INFORMATION TO USERS

This manuscript has been reproduced from the microfilm master. UMI films the text directly from the original or copy submitted. Thus, some thesis and dissertation copies are in typewriter face, while others may be from any type of computer printer.

The quality of this reproduction is dependent upon the quality of the copy submitted. Broken or indistinct print, colored or poor quality illustrations and photographs, print bleedthrough, substandard margins, and improper alignment can adversely affect reproduction.

In the unlikely event that the author did not send UMI a complete manuscript and there are missing pages, these will be noted. Also, if unauthorized copyright material had to be removed, a note will indicate the deletion.

Oversize materials (e.g., maps, drawings, charts) are reproduced by sectioning the original, beginning at the upper left-hand corner and continuing from left to right in equal sections with small overlaps. Each original is also photographed in one exposure and is included in reduced form at the back of the book.

Photographs included in the original manuscript have been reproduced xerographically in this copy. Higher quality 6" x 9" black and white photographic prints are available for any photographs or illustrations appearing in this copy for an additional charge. Contact UMI directly to order.

UMI

A Bell & Howell Information Company
300 North Zeeb Road, Ann Arbor MI 48106-1346 USA
313/761-4700 800/521-0600

ANALYSIS, STABILITY AND CONTROL OF WAKE FLOWS PAST A CIRCULAR CYLINDER: A NUMERICAL AND THEORETICAL STUDY

by

SHAOJIE TANG

A dissertation submitted to the Graduate Faculty in Engineering in partial fulfillment of the requirements for the degree of Doctor of Philosophy, The City University of New York

1997

This manuscript has been read and accepted for the Graduate Faculty in Engineering in satisfaction of the dissertation requirement for the degree of Doctor of Philosophy.

9/12/97
Date

Chair of Examining Committee

9/16/97
Date

Executive Officer

Professor Andreas Acrivos

Professor Nadine Aubry

Professor Yannis Andreapoulos

Professor George Triantafyllou

Professor Michael Siegel

Supervisory Committee

THE CITY UNIVERSITY OF NEW YORK

Abstract

ANALYSIS, STABILITY AND CONTROL OF WAKE FLOWS PAST A CIRCULAR CYLINDER: A NUMERICAL AND THEORETICAL STUDY

by

Shaojie Tang

Advisor: Professor Nadine Aubry

Two-dimensional wake flows past a circular cylinder have been investigated from low to moderately high Reynolds numbers, focusing on the stability and the control by means of low dimensional models and numerical simulations.

In the first part of this work, the impulsively started flow past a cylinder is computed by a two-dimensional direct numerical simulation over the range of Reynolds numbers $20 \leq Re \leq 1000$. At low Reynolds numbers, the flow consists of twin vortices which are images of one another by reflection through the centerline. This bubble of vortices first grows with time, before saturating to a steady solution. As Reynolds number is increased further, the flow keeps its symmetric bubble structure for a short time, undergoes a symmetry breaking instability and develops into a shedding vortex street. This symmetry breaking is naturally captured in our numerical simulation in the sense that the vortex shedding develops without the necessity of any external forcing or perturbation, as well as artificially captured by introducing a

particular perturbation. The critical Reynolds number is predicted by our numerical simulations to be 47.5. This (natural) symmetry breaking is found to be responsible for a significant increase in drag. Our results before and after the symmetry breaking events are compared with others' numerical and experimental results.

In the second part of this work, we concentrate on understanding and modeling the symmetry breaking bifurcation observed at $Re \geq 47.5$ in our numerical simulations. Föppl's vortex model is studied here as a low dimensional model for the symmetric bubble. The stability analysis of a fixed bubble in the model shows that there are two asymmetric eigenmodes, a stable mode and an unstable one. We show by direct numerical simulations of the impulsively started flow past a circular cylinder how the instability properties of the model mimic those of the real flow.

In the third part of this work, we show how the introduction of two additional weak potential vortices in the model is capable of (neutrally) stabilizing the flow by making the real part of all eigenvalues of the Jacobian matrix zero. We then control vortex shedding behind a circular cylinder in numerically simulated viscous flows by inserting two small vortex perturbations. The control has the effect of either suppressing vortex shedding, making the flow converge toward a stable, symmetric bubble, or altering vortex shedding by generating a reversed Karman vortex street.

Acknowledgments

I would like to thank my advisor, Professor Nadine Aubry, for her support, guidance and patience. She has been a great source of motivation, both personal and professional. Her generous advices, encouragements and constant faith have made my time with her a very challenging and rewarding experience.

I would also like to thank Professor John L. Lumley for hosting me at Cornell University where a part of this work was completed. I am very grateful to Professor Andreas Acrivos, Professor Yannis Andreapoulos and Professor George Triantafyllou for their very useful comments.

I am very indebted to my wife, Fengli Chen, for giving me great support which helped me concentrate on my research and course work, take examinations and meet deadlines during this challenging time. I am also thankful to Dr. Nianzheng Cao and Dr. Yu Zheng for many useful discussions and their continued help. Finally, I would like to thank Dr. Thomas Leweke, Dr. Helene Persillon, Dr. Anil Prasad and Professor C.H.K. Williamson for interesting discussions during my visit at Cornell University.

TABLE OF CONTENTS

LIST OF TABLES

LIST OF FIGURES

Chapter 1

Introduction

The problem of the flow about a bluff body is returned to, in the literature, again and again. The reason for this is clear enough -not only is the problem always of great practical importance, but it has so far not given way to theoretical treatment.

Anatol Roshko, On the wake and drag of bluff bodies (1955)

1.1 Circular cylinder wake flows

Wake flows past circular cylinders have been studied for more than 100 years since Strouhal (1878). Many important contributions have been made, and a partial list includes Karman (1911), Föppl (1913), Kovasznay (1949), Roshko (1955), Tritton (1959), Abernathy and Kronauer (1961), Gerrard (1966, 1978), Berger (1967), Acrivos *et al.* (1968), Perry *et al.* (1982), Williamson (1989), Strykowski and Sreenivasan (1990). A large number of experimental, theoretical and numerical studies have concentrated on this topic and it is beyond the scope of this thesis to recall all previous contributions. Instead, we refer the interested reader to the extensive reviews by Wille (1960, 1966), Morkovin (1964), Mair and Maull (1971), Berger and Wille (1972), Bearman and Graham (1980), Oertel (1990), Coutanceau and Defaye (1991)

and Williamson (1996).

One of the most important current issues lies in the understanding of transient regimes in unsteady separated flows due to accelerated and decelerated motions. Here, we concentrate on the accelerated flow only. At low Reynolds numbers, the latter flow consists of a bubble of two vortices, invariant under reflection through the mid-plane. Above the critical Reynolds number, the flow remains a symmetric bubble at early times but the asymptotic state consists of a periodic vortex shedding, asymmetric at all times. While most previous studies have focused on either the asymptotic state or the very early (symmetric) stages of the flow, one of the purposes of the present work is to draw a bridge between these two states. In the first part of the thesis, we describe the symmetry breaking events, together with its consequences on the global features of the flow including the body force. Not only is such a description of primary importance from a fundamental viewpoint, but also it should play a crucial role in the understanding of unsteady separated flows in general and in the control of the vortex shedding process itself.

Numerical investigations of the impulsively started flow are difficult, even in the symmetric bubble regime, due to the singular character of the flow at early times, and the fine details of the separation phenomena. Although numerous investigations have been reported in the literature, there are still open questions related to the validity and precision of the numerics, particularly at high Reynolds numbers. However, this flow presents a great advantage compared to many other unsteady flows since approximate analytical solutions (essential to test numerical findings) have been available since the early work of Blasius (1908). These flows are time power series symmetric solutions valid for short times. So far, the most accurate solutions are those obtained by Collins and Dennis (1973b) and Bar-Lev and Yang (1975). In the following of this thesis, we will use such solutions extensively to validate our

simulations at early times.

The symmetric stage of the flow was simulated by Ta Phuoc Loc (1980) who used a streamfunction/vorticity formulation to integrate the equations of motion in the range of Reynolds numbers $550 \leq Re \leq 1000$. This work was then extended to higher Reynolds numbers ($3000 \leq Re \leq 9500$) by Ta Phuoc Loc and Bouard (1985). More recently. Smith and Stansby (1988), Chang and Chern (1991) and Koumoutsakos and Leonard (1995) have used vortex methods to simulate the evolution of the symmetric bubble. In particular, Koumoutsakos and Leonard have provided benchmark quality simulations for the early stages of the flow, using more than 50 000 vortex elements on the Cray YMP. Throughout the present work, we will carry out detailed comparisons between their results and ours in the early stages of the flow.

Numerous experiments of an impulsively started flow past a cylinder have been carried out since the pioneer works of Nayler and Frazer (1917) and Prandtl (1927). The two experiments most relevant to the present study are those of Bouard and Coutanceau (1980) and Perry *et al.* (1982). Bouard and Coutanceau's apparatus consists of a translating cylinder subject to a (quasi)-impulsive acceleration. They visualized the flow structures by means of solid tracers introduced in uniform suspension in the fluid. Their detailed description of the growing bubble in a broad range of Reynolds numbers ($40 < Re < 10^4$) has played a major role in providing data for validating numerical simulations. Perry *et al.* (1982) have used time-exposure photography of the motion of aluminum particles in order to obtain a sequence of instantaneous streamline patterns. These patterns show that the bubble or cavity behind the cylinder is closed at early times, and opens up when the vortex-shedding process begins. At that time, instantaneous 'alleyways' of fluid are formed which penetrate the cavity. Coutanceau and Defaye (1991) also report similar vortex-shedding mechanisms from their experiments.

Despite numerous studies, the breakdown of the growing (unsteady) symmetric bubble into the Karman vortex street is not fully understood. However, the steady solutions and their linear stability properties have been obtained. Steady solutions at various Reynolds numbers can be found in Acrivos *et al.* (1968), Takami and Keller (1969), Dennis and Chang (1970) and Fornberg (1980, 1985), while the linear stability analysis has been performed by Jackson (1987) and Zebib (1987). They found that the steady, symmetric solution undergoes a Hopf bifurcation, and that the solution emerging from the bifurcation is asymmetric. The critical Reynolds numbers found by these studies agree reasonably well ($Re_c = 46$ from Jackson (1987) and $R\epsilon_c = 40$ from Zebib (1987)). However, the values of Re_c reported in the literature from experimental studies are scattered between $Re_c = 34$ and $Re_c = 48$ (Kovasznay, 1949, Coutanceau and Bouard, 1977, Nishioka and Sato, 1978, Mathis *et al.*, 1984 and Williamson, 1989). An important work about critical Reynolds number from experimental studies is that of Shair *et al.* (1963). They found that the critical Reynolds number is strongly influenced by the proximity of the walls of the confining experimental equipment. Whether there is a link between the instability of the unsteady, impulsively started flow and that of the steady solution of the NS equations still remains to be investigated. We have used the present code to determine the critical Reynolds number by direct numerical simulation.

1.2 Vortex shedding from a circular cylinder

As far as the vortex shedding alone is concerned, many numerical simulations have been performed and a partial list includes Jordan and Fromm (1972), Gresho *et al.* (1980, 1984), Braza *et al.* (1986), Chilukuri (1987), Eaton (1987), Karniadakis and Triantafyllou (1989), Anagnostopoulos (1989), Franke *et al.* (1990),

Engelman and Jamnia (1990), Stansby and Slaouti (1993), Zhang *et al.* (1995), Henderson (1995) and Anagnostopoulos and Iliadis (1996). The sensitivity of the vortex shedding to small external perturbations makes the numerical results, such as the Strouhal number, the drag and the lift, strongly dependent on the specific boundary conditions chosen, the size of the domain, etc. Such a strong sensitivity to the box size, often referred to as "the blockage effect", has remained a challenge not only numerically but also experimentally. The effect was first discovered experimentally by Shair *et al.* (1963) who showed that the stability of the steady laminar wake behind a circular cylinder is strongly influenced by the proximity of the walls in the confining experimental equipment. The blockage effect has remained a challenge numerically since most numerical flows are computed within a relatively small computational box. In order to guarantee the validity of our computation, we use a very large (more precisely, several thousands (or more) times the radius of the cylinder) physical domain. Our technique, however, consists of an adaptive scheme which increases the size of the computational domain as the vorticity is transported away from the body.

Despite many contributions, it seems fair to say that much remains unclear about the formation of the vortices present in the flow past a circular cylinder. Since vortex shedding is born from the break-up of the recirculating, symmetric bubble in an impulsively started wake flow, a very basic and long standing issue concerns the origin and understanding of the symmetry breaking the flow undergoes. Here, as in some previous works (Aubry *et al.*, 1988; Sanghi and Aubry, 1993), we are investigating issues regarding causality and mechanisms which are difficult to answer by means of the full, complex Navier-Stokes equations. We are thus looking for a low dimensional dynamical system, a simple model, capable of capturing the basic features of the stability property of the symmetric bubble. Not only is the issue regarding the origin of the symmetry breaking instability of primary importance from

a fundamental viewpoint, but also it plays a crucial role in the control of the vortex shedding process.

It is well known that if a circular cylinder starts moving from rest in an incompressible fluid, twin vortices spinning in opposite directions form behind the cylinder soon after the motion begins. These vortices grow and become more and more elongated as time increases until they reach their maximal size. After that time, the bubble of vortices remains steady at low Reynolds numbers, develops into a time dependent oscillating wake regime in which the bubble remains attached to the body or breaks down into a Karman vortex street at higher Reynolds numbers. It is interesting to notice that if the initial condition is symmetric, the solution formally remains symmetric at all later times $t > 0$. In other words, the subspace of symmetric solutions is an invariant subspace of the Navier-Stokes equations subject to the boundary conditions considered here. The fact that the flow goes away from this subspace beyond the critical Reynolds number in both physical and numerical experiments means that the symmetric bubble becomes unstable beyond the critical Reynolds number. This observation led Föppl (1913) to investigate whether one can find steady solutions in the form of twin vortices and study their stability property. Föppl represented the system by building a two-dimensional, incompressible potential flow consisting of a uniform oncoming flow, a pair of point vortices symmetrically located with respect to the centerline behind the cylinder, and inner vortices placed to satisfy the boundary condition on the body (see Lamb, 1945; Milne-Thompson, 1962 and Saffman, 1992). He found fixed points (i.e. steady flows) for which the twin vortices can indeed maintain their locations relative to the cylinder. Such equilibrium positions are located on two symmetric curves starting from the rear stagnation point of the bubble. Föppl (1913), who also studied the stability of the equilibrium, showed that the vortices are stable to all symmetric perturbations and unstable to

some asymmetric perturbations. However, there was a mistake in Föppl's analytical results which was later detected and corrected by Smith (1973) who showed that the equilibrium is only marginally stable to all symmetric perturbations (instead of being stable as originally found by Föppl, 1913). Laat and Coene (1995) studied Föppl's vortex model numerically and showed that a vortex located near the equilibrium rotates with some frequency around this point in a closed orbit. They also checked numerically that the fixed point is indeed unstable to asymmetric perturbations. In the second part of this work, we reexamine Föppl's vortex model and find that the equilibrium is unstable to some asymmetric perturbations (referred to as asymmetric "divergent" perturbations) and stable to some other asymmetric perturbations (referred to as asymmetric "convergent" perturbations). The specific shape of the perturbation is therefore crucial. We show in the second part how this property remains valid in our two-dimensional numerical simulation of the viscous flow past a cylinder.

Over the years, the onset of vortex shedding has been the subject of various descriptions. For instance, Gerrard (1966) described the onset of vortex shedding as follows. "The growing vortex continues to be fed by circulation from the shear layer until the vortex becomes strong enough to draw the other shear layer across the wake. The approach of oppositely-signed vorticity in sufficient concentration cuts off further supply of circulation to the vortex, which then ceases to increase in strength. We may speak of the vortex as being shed from the body at this stage." Perry *et al.* (1982) marked the vortex shedding by the opening of the closed bubble in the wake. They showed that the bubble or cavity behind the cylinder is closed at early times, and opens up when the vortex-shedding process begins. At that time, instantaneous 'alleyways' of fluid are formed which penetrate the cavity.

Over the last decade, research on the vortex shedding from bluff bodies has

received a new impulse from the theory of hydrodynamic stability. In order to study the stability property of the wake behind a circular cylinder, the stability property of the time averaged profile of the Karman vortex street was considered and the so-called "locally parallel approximation" was made (Triantafyllou *et al*, 1986). Yet, the fact that such theoretical studies lead to a frequency of the Karman vortex street at the instability onset very close to that experimentally observed is extremely impressive. Another approach was undertaken by Jackson (1987) and Zebib (1987) who presented direct computations of the stability property of the symmetric bubble from the full Navier-Stokes (NS) equations in the neighborhood of the critical Reynolds number. They found that the transition is marked by a Hopf bifurcation. The details of the bifurcation, however, are difficult to fully understand, due to the fact that the full NS equations constitute a high dimensional dynamical system.

The aim of the second part of this work is to find a low-dimensional dynamical system which will enlighten the mechanism responsible for the symmetry breaking instability leading to vortex shedding. In Chapter 3, we present the linear stability analysis of the low dimensional dynamical system consisting of a two-dimensional, potential vortex model, as originally derived by Föppl (1913). Our analysis, however, goes further than Föppl's early study. In particular, our study is carried out for *any* perturbation and special attention is given to the particular shape of the eigenmodes obtained.

1.3 Vortex shedding control

Vortex shedding control has been the object of intensive research over recent years. Arguments motivating the investigation of this issue are numerous. For instance, the shedding of vortices from alternate sides of bluff bodies is associated with

strong periodic transverse forces that can damage the body. Preventing the instability from occurring would thus lead to the suppression of vortex-induced vibrations. It may also lead to drag reduction, a desired feature in many applications.

A wide variety of techniques have been applied, such as the use of a splitter plate (Roshko, 1955 and Grove *et al.*, 1964), base bleed (Wood, 1967 and Bearman, 1967), forced cylinder vibrations (Wehrmann, 1965; Berger, 1967 and Schumm *et al* 1994), wake heating (Noto *et al.*, 1985 and Mori *et al.*, 1986), a small secondary cylinder (Strykowski and Sreenivasan 1990), rotary oscillation of a cylinder (Tokumaru and Dimotakis, 1991), and a flapping foil (Gopalkrishnan *et al.* 1994) among others (see, e.g., the extensive review by Zdravkovich, 1981). Feedback control techniques have also been developed (Ffowcs Williams ans Zhao, 1989, and Roussopoulos, 1993).

Some of these techniques are successful at controlling or suppressing vortex shedding through a large modification (e.g. a splitter plate of length $10a$ or a flapping foil of chord $4a$, where a is the radius of the cylinder). Some other approaches, such as the insertion of a small cylinder in the wake, are small local modifications but are usually restricted to a small range of Reynolds numbers. In many cases, control techniques are empirical.

The implementation of an efficient, *smart* control strategy requires the understanding of the origin of the physical phenomenon one wants to control. For this purpose, the derivation and analysis of a model, preferably a low dimensional dynamical system which can capture the essential features of the physics and be understood relatively easily, should be of great help. During the last decade, the use of low dimensional dynamical systems as powerful tools to model fluid mechanics phenomena has attracted much attention (see, for instance, Aubry *et al.*, 1988; Sanghi and Aubry, 1993; and Coller *et al.*, 1994). The third part of this work is based on these simple ideas applied to the origin of vortex shedding and its control.

In Chapter 4, we introduce two small control vortices in the model and find that this insertion is responsible for the appearance of a neutrally stable equilibrium point. We then apply the technique to the numerically simulated flow and show that the control vortices can either suppress vortex shedding or generate a reversed Karman vortex street.

Chapter 2

Numerical simulations of circular cylinder wake flows

2.1 Preliminaries

In contrast to most previous studies, the aim of the present chapter is to simulate the impulsively started flow past a circular cylinder in two dimensions and to document the transient during which symmetry breaking occurs. In order to avoid the well-known blockage effect, We use a very large physical domain. Our technique is an adaptive scheme which increase the size of the computational domain as the vorticity moves away from the body. The instabilities we describe below are only due to the instability of the bubble itself, triggered, unless specified otherwise, by round-off errors and truncations due to the (necessarily limited) accuracy of the schemes used. It is the first prediction of the critical Reynolds number by direct numerical simulations. Some results of this chapter are reported in Tang and Aubry (1996).

2.2 The governing equations

We first start by giving the formulation of the Navier-Stokes equations we consider to simulate an impulsively started flow past a circular cylinder of radius a. Hereafter, U_∞ denotes the free-stream velocity at times $t \geq 0$.

We restrict ourselves to the two-dimensional formulation of the Navier-Stokes equations and write the equations in an exponential-polar coordinate system (ξ, η) defined by

$$\tilde{r} = a e^{2\pi\xi} \tag{2.1}$$

$$\tilde{\theta} = 2\pi\eta \tag{2.2}$$

where $(\tilde{r}, \tilde{\theta})$ are the polar coordinates (see figure 2.1). This exponential mapping allows us to treat a very large physical domain in order to avoid the blockage effect. Such a mapping permits the implementation of appropriate boundary conditions at (nearly) infinity, while keeping the cost of our numerical simulations affordable. We should keep in mind, however, that the flow is well resolved only in the near-wake since the grid size dramatically increases with the distance from the cylinder. Figure 2.2 shows the typical grids used in our computations around the cylinder.

Formulation of the Navier-Stokes equations

We choose the vorticity/streamfunction formulation of the Navier-Stokes equations and consider the following dimensionless variables: $\omega = \tilde{\omega}a/U_\infty$, $\psi = \tilde{\psi}/U_\infty a$, $V_r = \tilde{V}_r/U_\infty$, $V_\theta = \tilde{V}_\theta/U_\infty$, $t = \tilde{t}U_\infty/a$, $r = \tilde{r}/a$, $\theta = \tilde{\theta}$. Here, $\tilde{\omega}$ denotes the vorticity, $\tilde{\psi}$ the streamfunction, $\tilde{V}_r$ and $\tilde{V}_\theta$ the radial and angular velocity components. The Navier-Stokes equations, expressed with respect to the previous

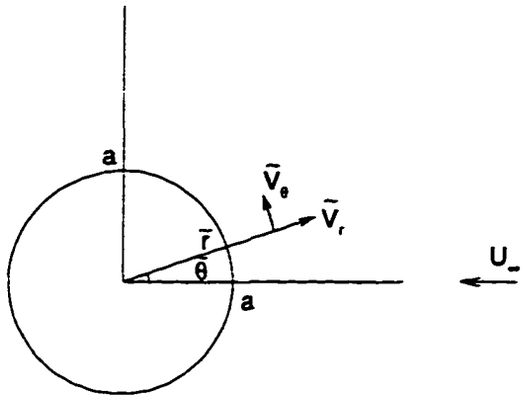

Figure 2.1: Flow configuration and system of coordinates in physical space. The oncoming flow is going from right to left in the computation.

dimensionless variables, become

$$E\frac{\partial\omega}{\partial t}+\frac{\partial U\omega}{\partial\xi}+\frac{\partial V\omega}{\partial\eta} = \frac{2}{Re}(\frac{\partial^2\omega}{\partial\xi^2}+\frac{\partial^2\omega}{\partial\eta^2}) \tag{2.3}$$

$$\frac{\partial^2\psi}{\partial\xi^2}+\frac{\partial^2\psi}{\partial\eta^2} = -E\omega \tag{2.4}$$

where $E=4\pi^2e^{4\pi\xi}, U=\partial\psi/\partial\eta=E^{\frac{1}{2}}V_r, V=-\partial\psi/\partial\xi=E^{\frac{1}{2}}V_\theta, Re=U_\infty 2a/\nu.$

Boundary conditions

These equations are subject to the following boundary conditions which consist of no-slip boundary conditions on the surface of the body and the two-dimensional potential flow at infinity, i.e.

$$\psi=0 \quad for \quad \xi\leq 0 \tag{2.5}$$

$$\psi=-2sh(2\pi\xi_\infty)sin(2\pi\eta) \quad at \quad \xi=\xi_\infty \tag{2.6}$$

for the streamfunction, and

$$\omega=-\frac{1}{E}\frac{\partial^2\psi}{\partial\xi^2} \quad at \quad \xi=0 \tag{2.7}$$

$$\omega = 0 \quad at \quad \xi = \xi_\infty \tag{2.8}$$

for the vorticity.

Note that we have considered that the velocity within the cylinder is zero in order to satisfy the no-slip velocity boundary condition systematically.

Initial condition

The impulsive start may be simulated by using the potential flow as the initial condition, except on the surface of the cylinder where the absence of slip is imposed.

Everywhere except on the surface of the cylinder, the flow is initially potential so that at $t = 0$.

$$\omega = 0, \quad \psi = -2sh(2\pi\xi)sin(2\pi\eta) \quad for \quad \xi > 0. \tag{2.9}$$

On the surface of the cylinder, the expression of the vorticity is obtained from equation (2.4) in which we have used the fact that at the surface $\partial^2\psi/\partial\eta^2$ vanishes. Therefore, at $t = 0$,

$$\omega = -\frac{1}{E}\frac{\partial^2\psi}{\partial\xi^2} \quad at \quad \xi = 0 \tag{2.10}$$

which will be discretized according to the scheme given in the next section (see equation (2.20)) in which we substitute the zero velocity boundary condition (2.5).

Forces on the body

After numerically solving equations (2.3) and (2.4), we pay particular attention to the force on the body $\vec{F_b}$ and the corresponding force coefficients

$$C_d = \frac{\text{drag force}}{\rho U_\infty^2 a}, \qquad C_l = \frac{\text{lift force}}{\rho U_\infty^2 a} \tag{2.11}$$

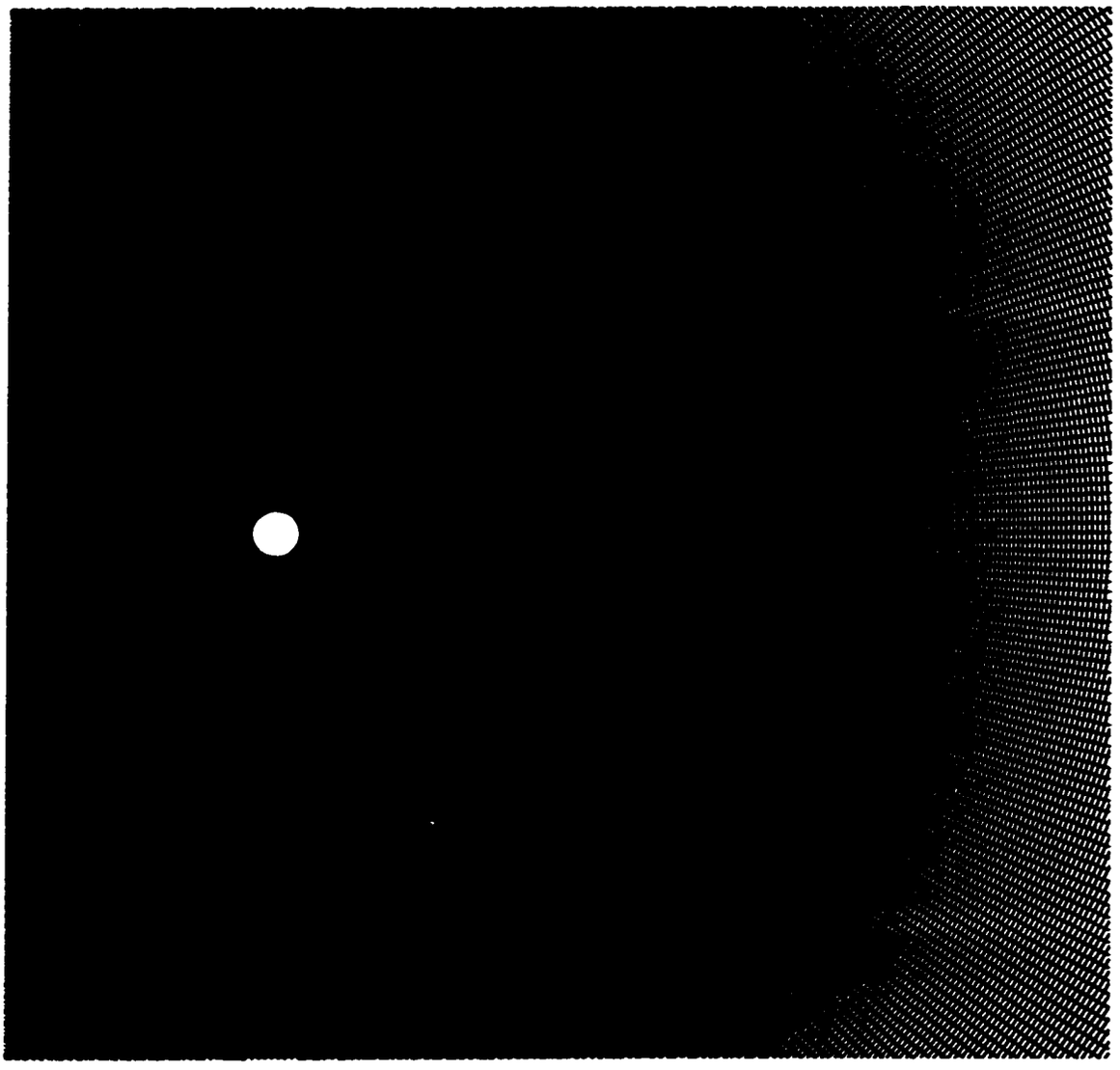

Figure 2.2: The grids used around the cylinder with 1200×512 grid points.

where C_d and C_l refer to the drag and lift coefficients, respectively. We now present various algorithms to compute the body force $\vec{F}_b$ or, equivalently, the corresponding force coefficients C_d and C_l.

Algorithm 1.

The time dependent forces on the body can be computed from the vorticity and the vorticity flux on the surface of the body, so that the lift and drag coefficients satisfy the relation

$$-C_d(t) + iC_l(t) = \frac{2}{Re} i \int_0^1 e^{i2\pi\eta} (2\pi\omega(t) - \frac{\partial\omega}{\partial\xi}(t))_{\xi=0} d\eta \tag{2.12}$$

where the contribution involving the vorticity flux leads to the pressure force while that originating in the vorticity gives the friction force. Although this formula can be easily implemented since we know the vorticity on the body surface at each time step. it is difficult to compute the vorticity flux at early times accurately owing to the initial discontinuity of the vorticity on the surface of the body.

Algorithm 2.

The forces on the body can also be computed from the control volume formulation of the momentum equation. Hereafter, *cv* and *cs* refer to the control volume and the control surface, respectively. For this purpose, we choose a coaxial cylinder of large radius containing the body. The net forces on the body can then be expressed as

$$\vec{F} = \vec{F}_{cs} - \frac{d}{dt} \int \int_{cv} \vec{u} \rho dv - \int_{cs} \vec{u} \rho \vec{u} \cdot \vec{n} ds \tag{2.13}$$

where $\vec{F}_{cs}$ denotes the force on the surface of the control volume. After converting into our system of coordinates and substituting the pressure in terms of the velocity (by means of the momentum equation), we obtain the expressions for the lift and drag coefficients.

$$
\begin{aligned}
C_d + iC_l &= -\frac{d}{dt}\int_0^{\xi_{cs}}\int_0^1 (V_r + iV_\theta)e^{i2\pi\eta}(2\pi r)^2 d\xi d\eta + i2\pi r^2 \frac{d}{dt}\int_{0\ cs}^{1} V_\theta e^{i2\pi\eta} d\eta \\
&+ ir\int_{0\ cs}^{1} (\frac{\partial V_r V_\theta}{\partial \xi} + 4\pi V_r V_\theta - \frac{2}{Re}\frac{\partial \omega}{\partial \xi})e^{i2\pi\eta} d\eta \\
&+ 2\pi r\int_{0\ cs}^{1} V_\theta^2 e^{i2\pi\eta} d\eta + i\frac{2r}{Re}\int_{0\ cs}^{1} \frac{\partial V_\theta / r}{\partial \xi} e^{i2\pi\eta} d\eta \\
&+ \frac{4\pi}{Re}\int_{0\ cs}^{1} V_r e^{i2\pi\eta} d\eta - 2\pi r\int_{0\ cs}^{1} V_r (V_r + iV_\theta)e^{i2\pi\eta} d\eta. \qquad (2.14)
\end{aligned}
$$

Note that this second technique requires the knowledge of the full velocity field in the control volume while the vorticity flux is needed only on the control surface. Here, we avoid the technical difficulty to compute the vorticity flux on the surface of the body which was required in the first algorithm. For this reason, we anticipate seeing an improvement in our numerical computations of the forces at early times.

Algorithm 3.

Finally, it is useful to recall that the forces on the body can also be computed by means of the formula

$$
\begin{aligned}
\vec{F} &= -\frac{d}{dt}\int\int_{fluid} \vec{u} dx dy \\
&= \frac{d}{dt}\int\int_{fluid} \vec{\omega} \times \vec{x} dx dy \\
&= \frac{d}{dt}\int\int_{fluid} (-\omega y \vec{i} + \omega x \vec{j}) dx dy. \qquad (2.15)
\end{aligned}
$$

Here, $\vec{i}$ denotes the direction of the free-stream flow. The use of such an expression, however, introduces artificial high frequency oscillations in our results similar to those reported by Koumoutsakos and Leonard (1995). For this reason, we will not implement it in the calculations. Instead, we will use it to explain certain features of the force acting on the full system in the numerical simulations of the vortex shedding control in Chapter 4.

Pressure

Finally, throughout this work, the pressure on the surface of the body will be computed from the expression

$$\frac{p(0,\eta)-p_\infty}{\frac{1}{2}\rho U_\infty^2} = 1 + \frac{4}{Re}\int_{0,\xi=0}^{\eta}\frac{\partial\omega}{\partial\xi}d\eta + \frac{4}{Re}\int_{0,\eta=0}^{\infty}\frac{\partial\omega}{\partial\eta}d\xi$$
$$+4\pi\int_{0,\eta=0}^{\infty}e^{2\pi\xi}\frac{\partial V_r}{\partial t}d\xi - 2\int_{0,\eta=0}^{\infty}V_\theta\frac{\partial V_r}{\partial\eta}d\xi - 4\pi\int_{0,\eta=0}^{\infty}V_\theta^2 d\xi. \qquad (2.16)$$

2.3 Moving boundary conditions for the vorticity

An adaptive scheme is developed in order to increase the efficiency of our numerical code. This scheme consists in moving the boundary used for the vorticity transport equation (2.3) further and further away from the body as the vorticity is transported outward. Indeed, we recall that the vorticity is first created in the boundary layers on the cylinder, and that it diffuses and convects away from the wall shear layer as time increases. In other words, the zero-vorticity line is initially very close to the body. When this is the case, the zero-vorticity boundary condition is valid in the neighborhood of the cylinder and there is no reason for maintaining it fixed at a very large (formally infinite) distance and computing the entire flow in a fixed, large computational domain. Designing a numerical scheme in which the boundary moves with the vorticity is a way of reducing the original infinite domain problem to a finite domain problem in a rigorous manner. Not only do we save a substantial amount of computing time by using this adaptive technique, but also we can guarantee that the vorticity does not reach the external boundary during the time of the computation. Keeping this goal in mind, we now divide our full physical domain into two subdomains, Region I and Region II, as shown in figure 2.3. The

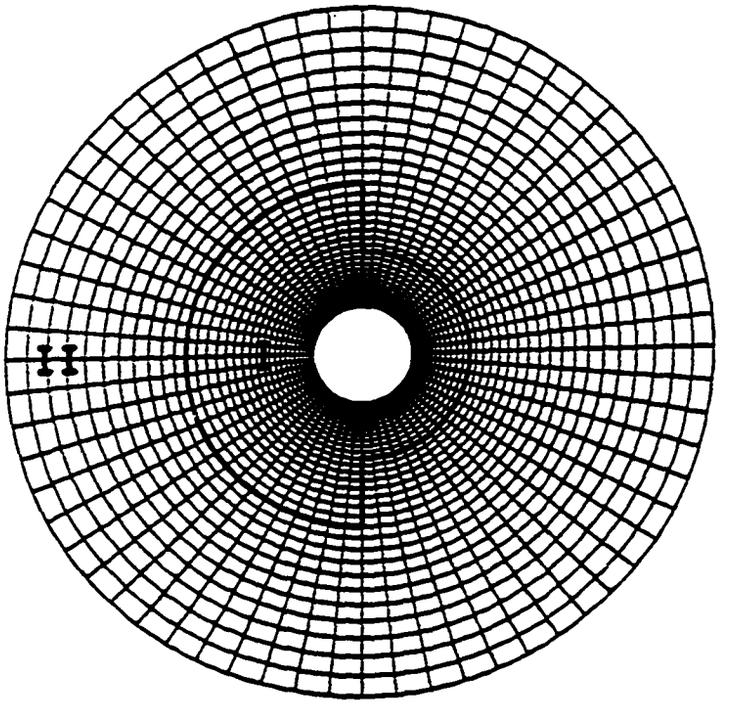

(a)

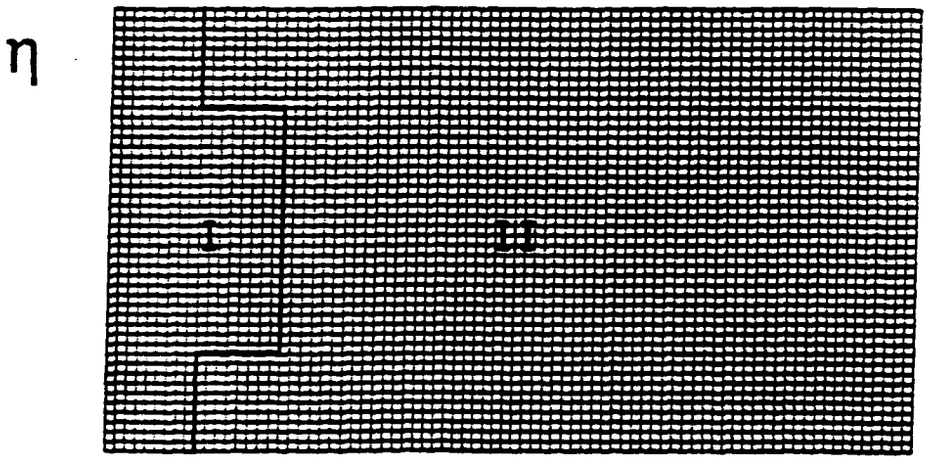

(b)

Figure 2.3: Illustration of the computational grid (with a large mesh size than that used in our computations). The sketches show the two domains in Section 2.3, Region I and Region II: (a) in the physical space, (b) in the computational space.

distinction between the two subdomains is that the vorticity is fully contained in Region I while the flow is vorticity free in Region II. We use two semi-circles to construct the boundary of Region I, taking into account the fore-aft asymmetry of the flow. Obviously, the semi-circle located downstream will be larger than that located upstream after $t = 0$, as a result of the adaptive scheme. Each semi-circle will move outward according to the evolution of the vorticity field, with its own (time dependent) velocity. The definition of the boundary between the two regions is such that the vorticity at *all points* on the boundary must be smaller, in absolute value, than a certain threshold chosen to be 10^{-15}. After determining the location of the boundary, the vorticity is set to zero on the boundary, as well as in Region II.

It is important to point out that since our threshold value is much smaller than the remaining computational errors, our adaptive scheme does not alter the accuracy of our computations. Note that Koumoutsakos and Leonard (1995) chose a much larger dimensionless cut-off vorticity value ($10^{-5,-6}$) in their high-resolution implementation of vortex methods.

2.4 Numerical methods

We now summarize the numerical methods we use to solve equations (2.3) and (2.4). These techniques are standard and more details can be found in the literature. An alternating-direction-implicit (ADI) algorithm is implemented to solve the vorticity transport equation (2.3), leading to the discretized formulae:

$$\frac{E_i}{\Delta t}\omega_{ij}^{n+\frac{1}{2}} - \frac{\omega_{ij+1}^{n+\frac{1}{2}} - 2\omega_{ij}^{n+\frac{1}{2}} + \omega_{ij-1}^{n+\frac{1}{2}}}{(\Delta\eta)^2 Re} + \frac{1}{4}\frac{(\tilde{V}\omega^{n+\frac{1}{2}})_{ij+1} - (\tilde{V}\omega^{n+\frac{1}{2}})_{ij-1}}{\Delta\eta}$$
$$= \frac{E_i}{\Delta t}\omega_{ij}^{n} + \frac{\omega_{i+1j}^{n} - 2\omega_{ij}^{n} + \omega_{i-1j}^{n}}{(\Delta\xi)^2 Re} - \frac{1}{4}\frac{(\tilde{U}\omega^{n})_{i+1j} - (\tilde{U}\omega^{n})_{i-1j}}{\Delta\xi} \qquad (2.17)$$

$$\frac{E_i}{\Delta t}\omega_{ij}^{n+1} - \frac{\omega_{i+1j}^{n+1} - 2\omega_{ij}^{n+1} + \omega_{i-1j}^{n+1}}{(\Delta\xi)^2 Re} + \frac{1}{4}\frac{(\tilde{U}\omega^{n+1})_{i+1j} - (\tilde{U}\omega^{n+1})_{i-1j}}{\Delta\xi}$$
$$= \frac{E_i}{\Delta t}\omega_{ij}^{n+\frac{1}{2}} + \frac{\omega_{ij+1}^{n+\frac{1}{2}} - 2\omega_{ij}^{n+\frac{1}{2}} + \omega_{ij-1}^{n+\frac{1}{2}}}{(\Delta\eta)^2 Re} - \frac{1}{4}\frac{(\tilde{V}\omega^{n+\frac{1}{2}})_{ij+1} - (\tilde{V}\omega^{n+\frac{1}{2}})_{ij-1}}{\Delta\eta} \qquad (2.18)$$

where $\tilde{U}$ and $\tilde{V}$ are the $\xi-$ and $\eta-$velocity components in the computational domain, which are calculated at the n^{th} time step.

An efficient algorithm using fast Fourier transforms (FFT) is employed to solve the Poisson equation (2.4) with second-order accuracy as in Hockney (1970):

$$\frac{\psi_{i+1j}^n - 2\psi_{ij}^n + \psi_{i-1j}^n}{\Delta\xi^2} + \frac{\psi_{ij+1}^n - 2\psi_{ij}^n + \psi_{ij-1}^n}{\Delta\eta^2} = -E_i\omega_{ij}^n. \qquad (2.19)$$

The vorticity distribution on the surface of the cylinder, which will play the role of boundary condition for the next time step, is computed by means of the equation:

$$\omega_{0j}^n = -\frac{1}{4\pi^2}\frac{\psi_{1j}^{n-1}}{\Delta\xi^2}. \qquad (2.20)$$

This vorticity used as the initial condition at the next time step represents the repetitive creation of vorticity at the surface of the body due to the action of viscosity at a solid wall.

The derivative of the vorticity ω needed in equation (2.12) is given by the discretization scheme:

$$\frac{\partial\omega^n}{\partial\xi}\Big|_{\xi=0} = \frac{1}{2\Delta\xi}(-3\omega_{0j}^n + 4\omega_{1j}^n - \omega_{2j}^n). \qquad (2.21)$$

2.5 Numerical results

We now compute the impulsively started flow past a circular cylinder in the Reynolds number range $20 \leq Re \leq 1000$.

First, we should mention that the radius of our entire computational domain, R_∞, is selected as large as possible in order to avoid the "blockage effect" and the wave reflection at the downstream boundary due to the relatively small size of the box (Shair *et al.*, 1963, Karniadakis and Triantafyllou, 1992, Anagnostopoulos and Iliadis, 1996). We recall that this effect can be significant as Karniadakis and Triantafyllou (1992) observed an error of 15% by increasing the size of their computational domain from $6a$ to $24a$ for instance.

In order to study the effect of the computational grid and the size of the time increment on the numerical solution, computations are performed with various grid sizes and time steps. The numerical parameters varied are the grid size in the ξ-direction, $\Delta\xi$, the grid size in the η-direction, $\Delta\eta$, the time step Δt and the number of grid points, $N_\xi \times N_\eta$. These parameters are chosen in order to guarantee numerical stability and maximize the computational accuracy. Our parameters and results are summarized in Table 1 where we report the values of our Strouhal number $St = 2af/U_\infty$, (f denoting the dominant frequency of the flow which we extract from our numerical data) and that of Williamson (1989). Our findings compare well with the experimental results.

We now investigate whether our numerical method is capable of capturing the $t^{-1/2}$ singularity of the drag coefficient at early times and we compare our results with those of Collins and Dennis (1973a), Bar-Lev and Yang (1975), and Koumoutsakos and Leonard (1995). Figure 2.4, which displays the drag computed from equation (2.14), gives evidence that a good agreement is found for times $t < 0.5$ at Reynolds numbers $Re = 40, 100, 500, 1000$. We recall that we have the choice between Algorithm 1 and Algorithm 2 to compute the forces on the body. We have found that Algorithm 2 gives more accurate results than Algorithm 1 in this regime of the flow, due to the (inaccurate) computation of the flux of vorticity on the surface

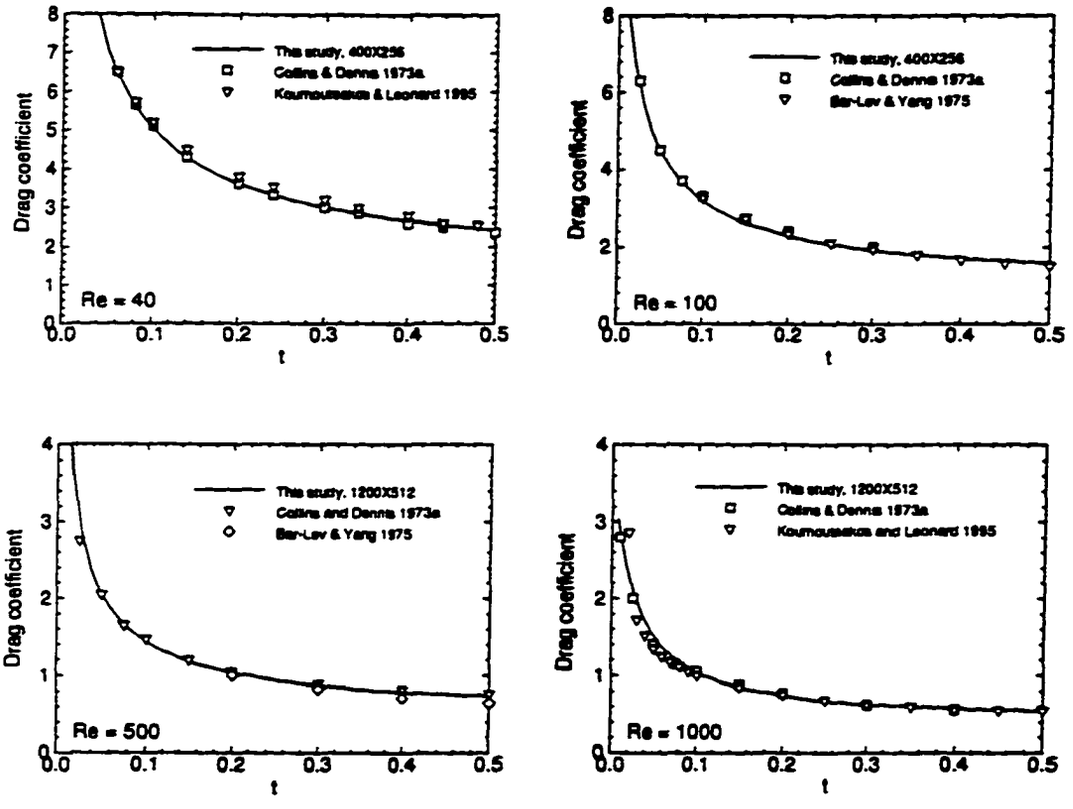

Figure 2.4: Time history of the drag coefficient at $Re = 40, 100, 500, 1000$, computed from Algorithm 2. One can observe that the $t^{-1/2}$ drag singularity is well captured by our computational scheme and that it compares well with the results of Collins and Dennis (1973a,b), Bar-Lev and Yang (1975) and Koumoutsakos and Leonard (1995).

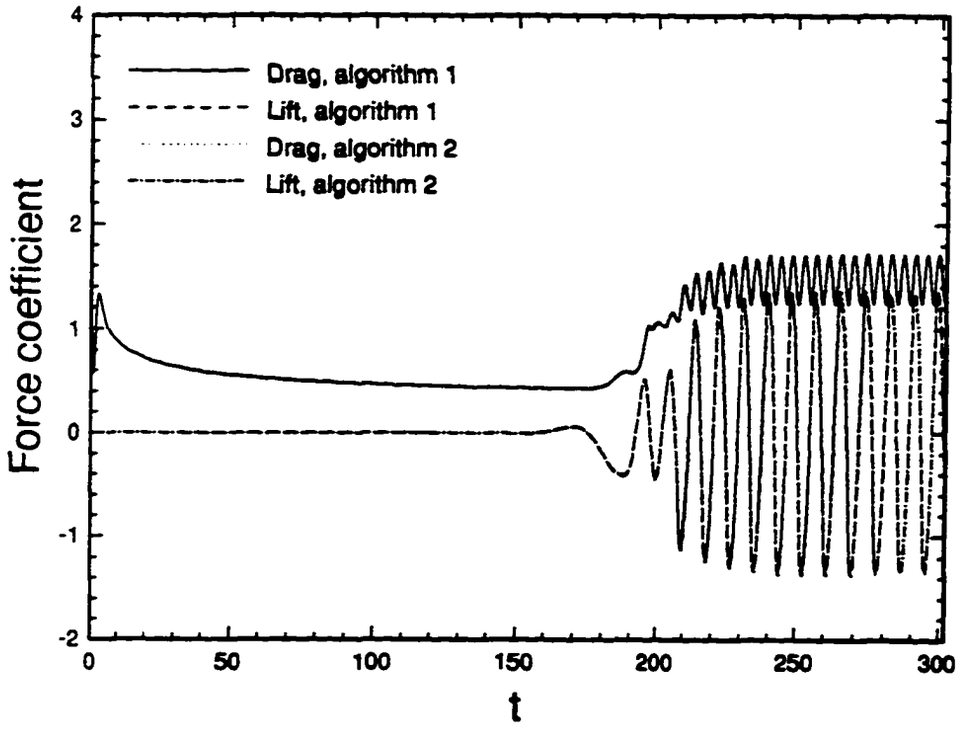

Figure 2.5: Comparison between the lift and drag coefficients using Algorithm 1 and Algorithm 2 in Section 2, at $Re = 1000$, with the 750×256 grid in double precision.

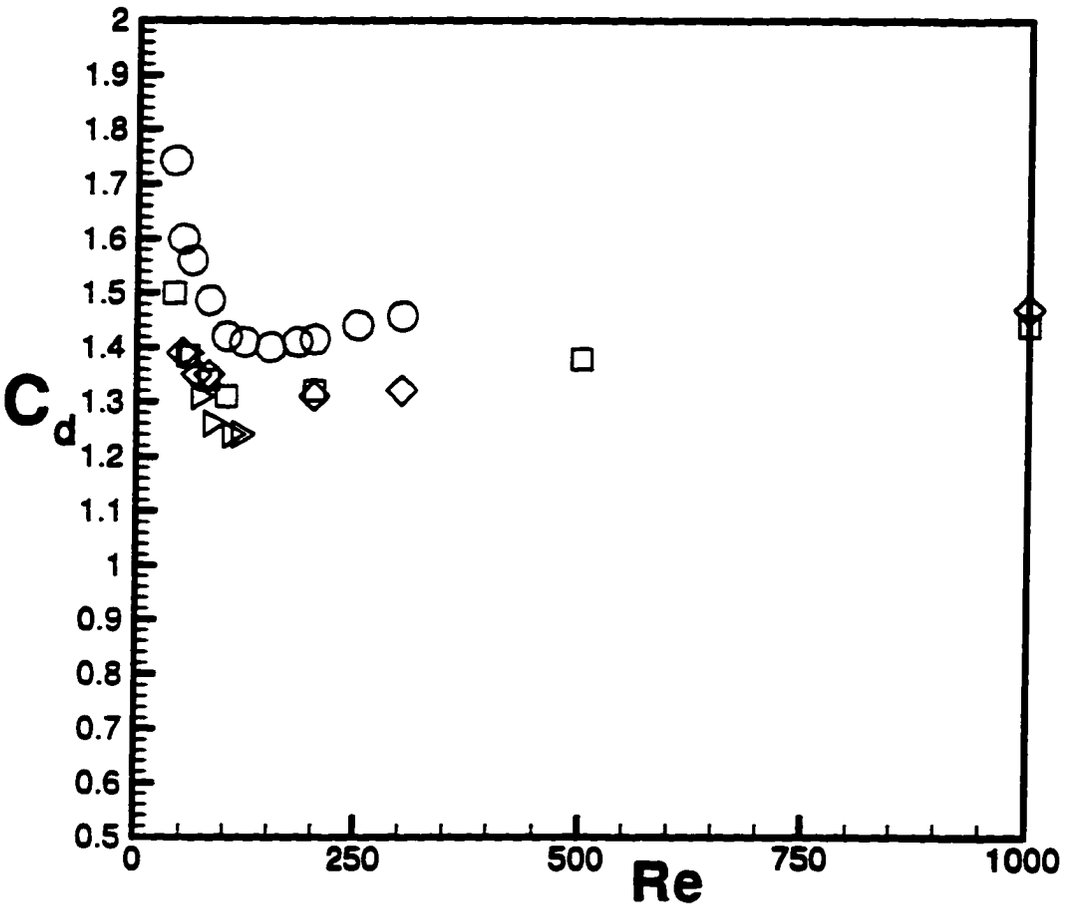

Figure 2.6: Mean drag coefficient versus Reynolds number: Zhang *et al.*'s (1995) data (circles), Franke *et al.*'s (1990) data (diamonds), Tritton (1959) (triangles), this study (squares).

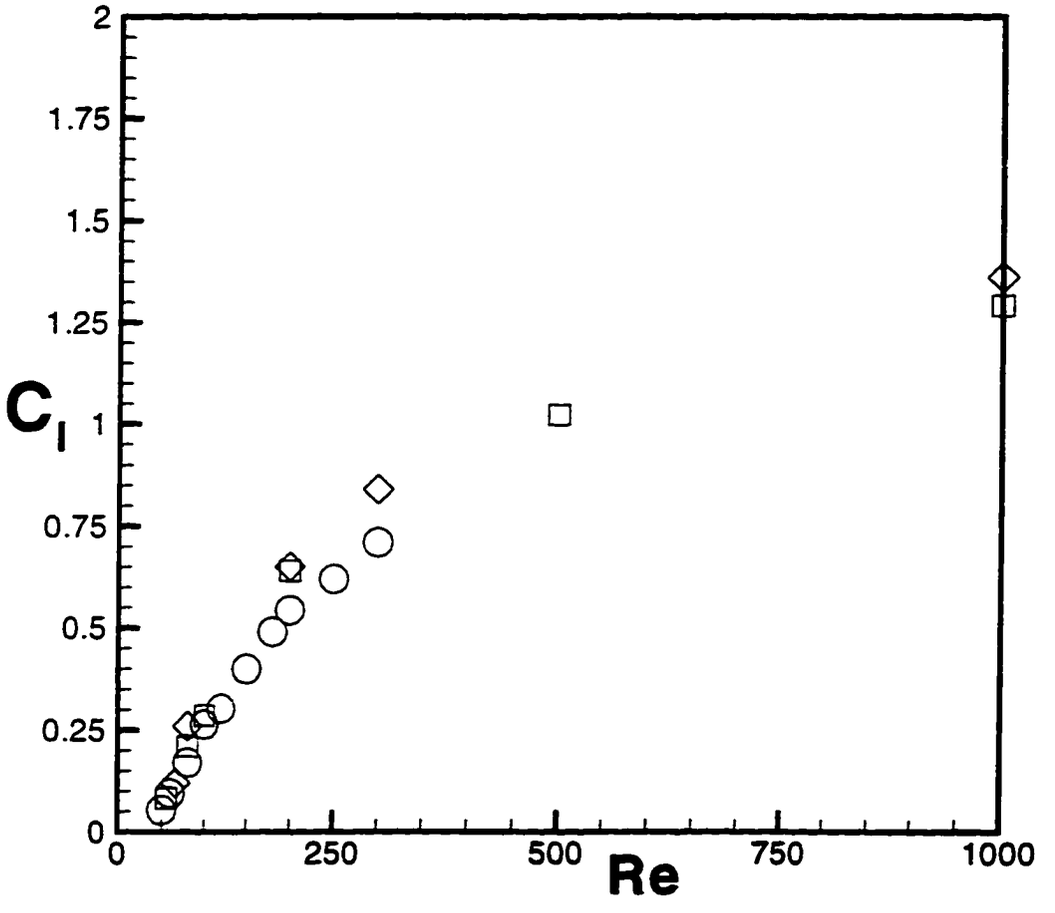

Figure 2.7: Amplitude of lift coefficient versus Reynolds number: Zhang *et al.*'s (1995) data (circles), Franke *et al.*'s (1990) data (diamonds), this study (squares).

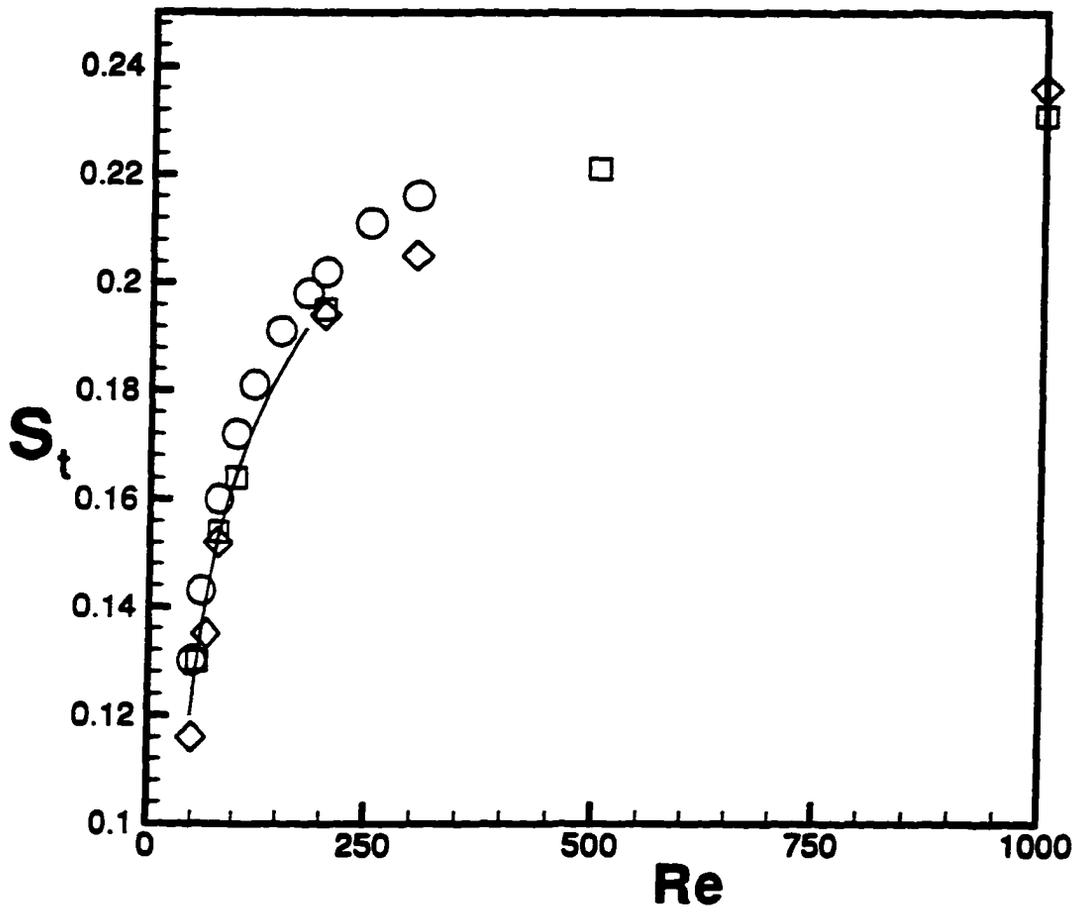

Figure 2.8: Strouhal number versus Reynolds number: Zhang *et al.*'s (1995) data (circles), Franke *et al.*'s (1990) data (diamonds), Williamson (1996) (solid line), this study (squares).

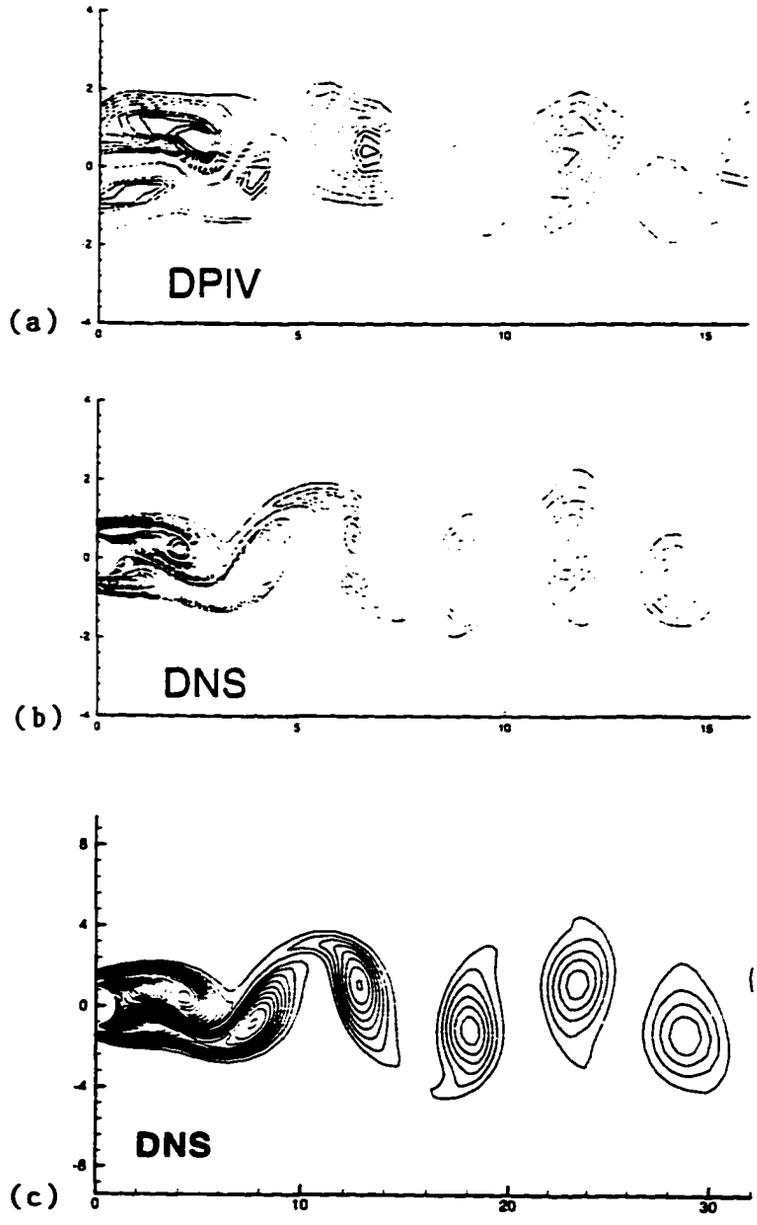

Figure 2.9: A comparison of results from DPIV experimental measurets by Hammache and Gharib (Henderson, 1994) (a), direct numerical simulation (DNS) by Henderson (1994) (b), and our DNS (c).

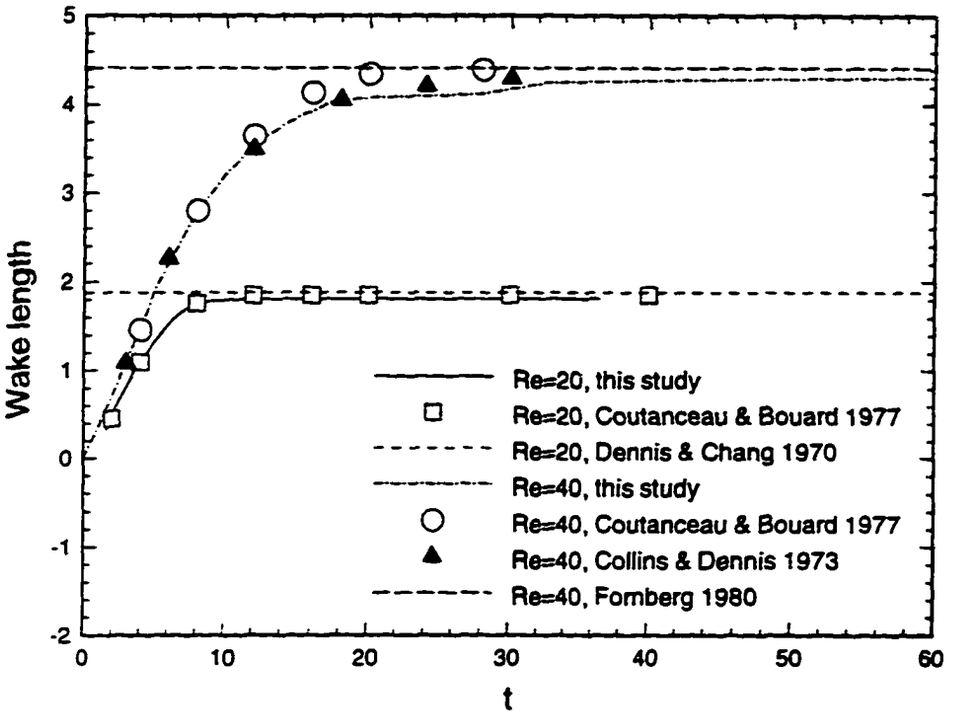

(a)

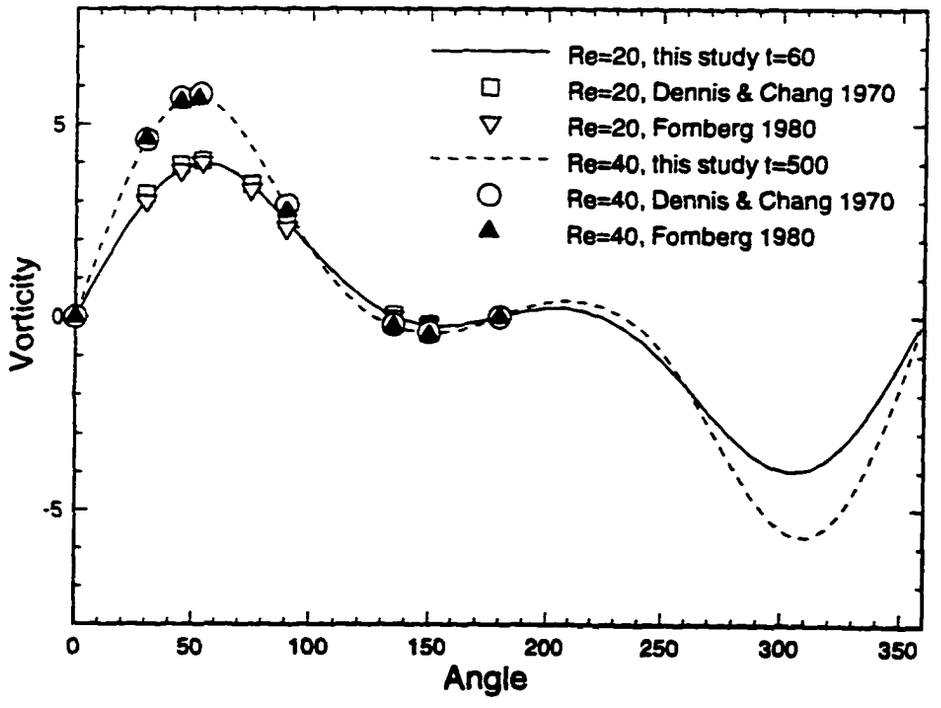

(b)

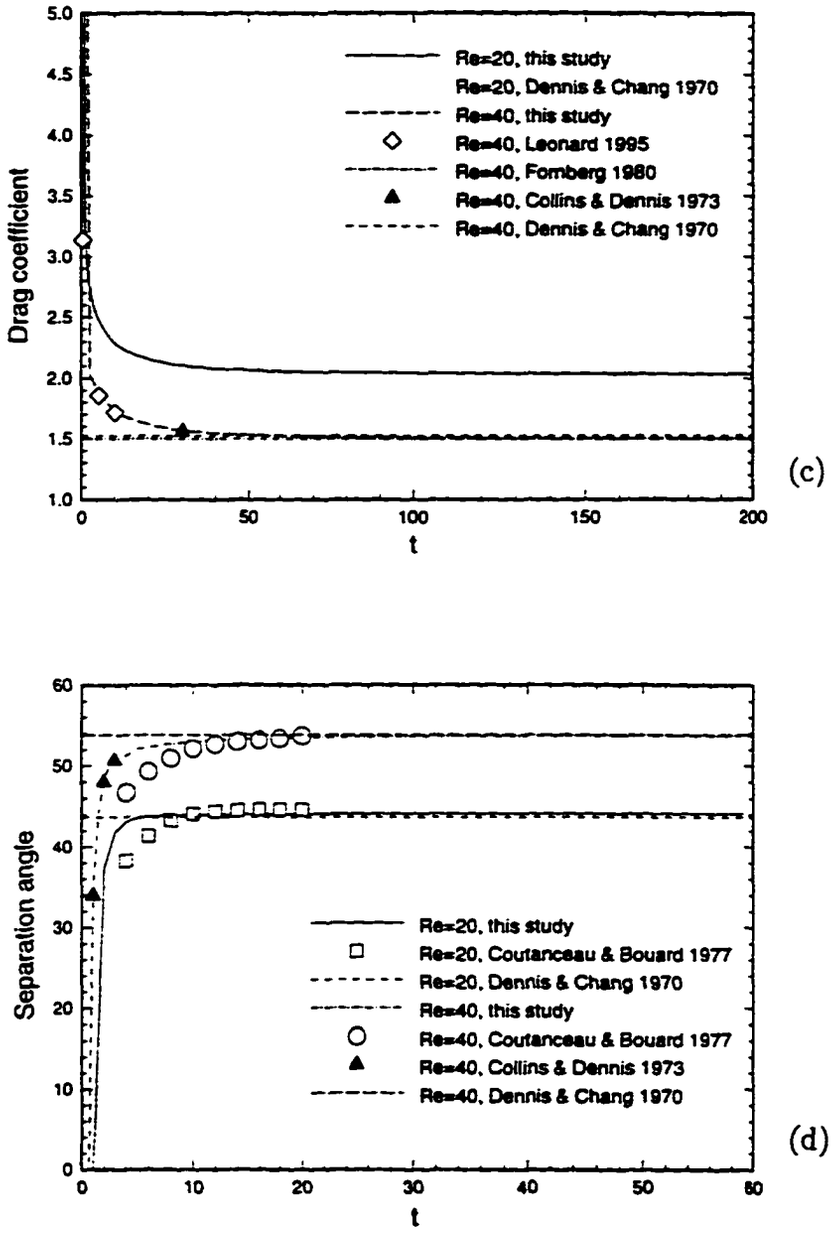

Figure 2.10: The flow computed at the Reynolds numbers $Re = 20$ and $Re = 40$. Here, we have used a 130×128 grid for $Re = 20$ and a 400×256 grid for $Re = 40$. (a) Time history of the wake length, (b) vorticity on the surface of the body, as a function of the angle expressed in degrees, at specific times, (c) time history of the drag coefficient, (d) time evolution of the separation angle. Our results are compared with others' experimental and numerical data.

of the body at early times in the first formulation (2.12). The discrepancy found between the two methods vanishes at later times, as shown in Figure 2.5.

As far as the vortex shedding is concerned, figure 2.6 , figure 2.7 and figure 2.8 display Reynolds number dependency of the mean drag coefficient, the amplitude of lift coefficient and the Strouhal number ($St = 2af/U_\infty$, f denoting the dominant frequency of the flow which we extract from our numerical data). Our results compare well with others' numerical and experimental data, particularly those of Williamson (1996) (for the Strouhal number) and Franke *et al.* (1990). Figure 2.9 shows the comparison of our results with DPIV experimental measurements and other's numerical results. It demonstrates the agreement between the numerical simulations and the experimental flow on qualitative detail in the wake, including the size, the shape, and the location of vortices.

We now report the details of our numerical results for various Reynolds numbers up to $Re = 1000$.

2.5.1 Computations at $Re = 20$ and $Re = 40$

Reynolds numbers $Re = 20$ and $Re = 40$ should be below the critical Reynolds number for vortex shedding, as indicated by physical experiments. Our DNS simulations show that the symmetric bubble is indeed stable for Reynolds numbers $Re \leq 40$, and unstable for $Re \geq 56$. In the neighborhood of the critical Reynolds number (about $Re = 40 - 50$), the instability takes a long time to develop because of the very small growth rate of the most unstable mode (see Jackson, 1987 and Zebib, 1987).

At the two Reynolds numbers $Re = 20$ and $Re = 40$, our solutions reach steady states after time $t = 15$ for $Re = 20$ and $t = 40$ for $Re = 40$. The flow structures take the shape of a bubble of symmetric vortices whose size grows as

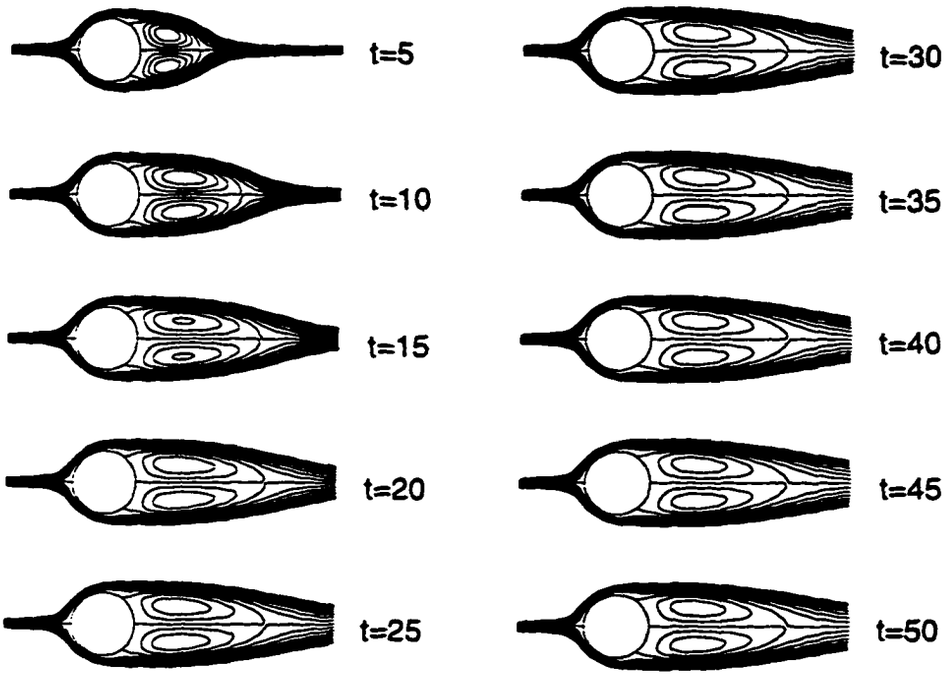

Figure 2.11: Streamlines of the flow at the Reynolds number $Re = 40$ at various times (see figure 2.10 for other characteristics of the flow). Although the incoming flow is from right to left in our computations, we flip all our streamlines as if the flow was coming from left to right in order to permit a better comparison between our results and those of others.

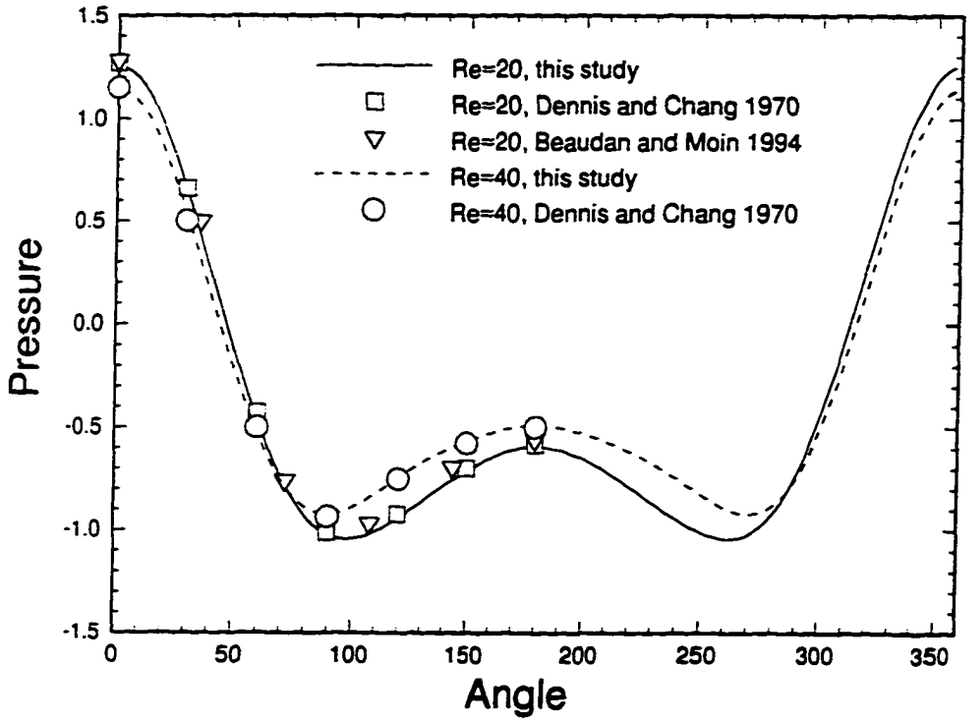

Figure 2.12: Pressure distribution of the flow along the body at the Reynolds numbers $Re = 20$ at time $t = 60$ with the 130×128 grid and $Re = 40$ at time $t = 100$ with the 400×256 grid. Our results compare well with those of others.

Re	$\Delta\xi$	$\Delta\eta$	Δt	$N_\xi \times N_\eta$	R_∞	St	St_e	T_m
20	0.0156	0.0078	0.01	130 × 128	309986			500
40	0.008	0.0078	0.005	200 × 128	22088			500
40	0.004	0.0039	0.005	400 × 256	22651			500
56	0.004	0.0039	0.005	400 × 256	22651	0.130	0.131	1000
80	0.008	0.0078	0.005	200 × 128	22088	0.154	0.153	500
100	0.008	0.0078	0.005	200 × 128	22088	0.166	0.164	500
100	0.004	0.0039	0.005	400 × 256	22651	0.164	0.164	500
200	0.004	0.0039	0.005	400 × 256	22651	0.195		500
500	0.003	0.0039	0.002	500 × 256	12160	0.222		200
500*	0.003	0.0039	0.002	500 × 256	12160	0.221		300
500	0.002	0.0039	0.002	750 × 256	12237	0.222		200
500	0.001	0.0019	0.001	1200 × 512	1869	0.221		200
500*	0.001	0.0019	0.001	1200 × 512	1869	0.221		350
1000	0.002	0.0039	0.002	750 × 256	12237	0.234		200
1000*	0.002	0.0039	0.002	750 × 256	12237	0.235		300
1000	0.001	0.0019	0.001	1200 × 512	1869	0.231		200
1000*	0.001	0.0019	0.001	1200 × 512	1869	0.231		300

Table 2.1: Parameter values used in this chapter, the values of the Strouhal number St found numerically in this work, the Strouhal number St_e reported experimentally by Williamson (1989) and the final time T_m at which our code was run. We report data for various Reynolds numbers Re. In each case, we give the grid sizes $\Delta\xi$, $\Delta\eta$ and time step Δt used in our computation. The star * denotes the use of double precision.

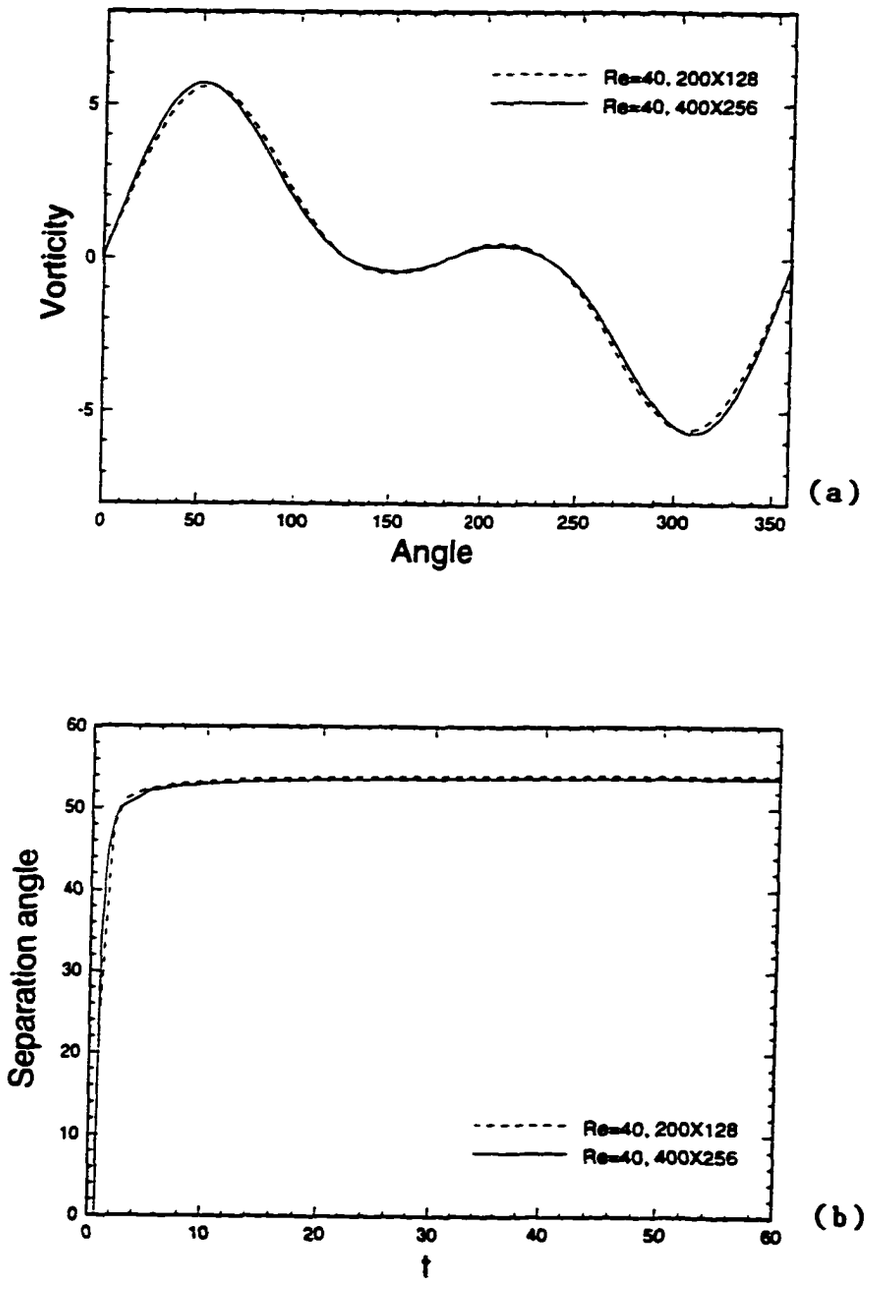

Figure 2.13: Comparison between the flow computed with a 200 × 128 grid and a 400 × 256 grid at the Reynolds number $Re = 40$. (a) distribution of the vorticity on the surface of the body as a function of the angle expressed in degrees at time $t = 500$, (b) separation angle as a function of time.

time increases until the growth saturates to an equilibrium state. We now present detailed results of our computations performed with a 400 × 256 grid. The growth of the bubble is represented in figure 2.10 (a) and compared with other numerical and experimental results, particularly those of Coutanceau and Bouard (1977) and Collins and Dennis (1973b) for the transient regimes, and those of Dennis and Chang (1970) and Fornberg (1980) for the asymptotic states. A good agreement is found in all cases. More details of the asymptotic, steady flow can be found in figure 2.10 (b) which displays the vorticity distribution on the surface of the body at time $t = 60$ for $Re = 20$ and at time $t = 500$ for $Re = 40$. In the upper mid-plane, while the primary vorticity is positive, some secondary, negative vorticity has appeared due to separation and the formation of a wall shear layer. As expected, both the primary vorticity and the secondary one are stronger at $Re = 40$ than at $Re = 20$. Again, our results agree very well with those of Dennis and Chang (1970) and Fornberg (1980). The time history of the drag coefficient and that of the separation angle are represented in figures 2.10 (c, d) where a comparison with others' studies is performed. One can notice that others' data points fall on our curves. While the values of the separation angle reported by Coutanceau and Bouard (1977) and our results coincide in the asymptotic regime, a small discrepancy is noticed during the transient which may be explained by the fact that Coutanceau and Bouard's results are extrapolated from experimental data obtained with a cylinder of finite length and that the location of the separation point is one of the most sensitive characteristics of the problem. Figure 2.11 displays the growth of the bubble at $Re = 40$ at various times. Hereafter, we flip all our streamlines as if the flow was coming from left to right (rather than from right to left, as in our computations) in order to permit a better comparison between our results and those of others. All our other figures are left original. Note that separation has already occurred at $t = 5$. A similar series of

pictures is obtained at $Re = 20$. Finally, figure 2.12 displays the distribution of the pressure along the cylinder surface at both Reynolds numbers. Our results agree well with those obtained in other studies (Dennis and Chang, 1970, Beaudan and Moin, 1994).

Figure 2.13 shows our findings obtained with a coarser grid consisting of 200×128 mesh points for Reynolds number $Re = 40$. The characteristics of the flow are very close to those obtained with a finer 400×256 grid.

2.5.2 Computations at $Re = 100$

We now compute the flow at $Re = 100$ by using the two grid sizes reported in Table 1. In this section, we report results obtained with the finer grid, although once again the differences observed with the two grids are very small. Our numerical simulation shows that the flow at $Re = 100$ becomes asymmetric after a certain time, developing into a Karman vortex street. Before we present the details of the events associated with this symmetry breaking, we first compare our numerical data with others' results either in the early (symmetric) stage of the flow, or in the asymptotic, periodic (asymmetric) regime. The growth of the wake length agrees well with the data provided by Collins and Dennis (1973b) at early times (see figure 2.14 (a)). The size of the bubble is, however, always smaller than that of the steady flow (see the comparison with Dennis and Chang (1970) and Fornberg (1980) in figure 2.14 (a)). This feature agrees with the experimental measurement of the largest wake length reported by Honji and Taneda (1969). The bubble size, in the latter study, is significantly smaller than ours. We should mention, however, that the sizes of the bubble before symmetry breaking are very scattered. For instance, Acrivos *et al.*'s experimental records give a wake length slightly larger than ours. Figure 2.14 (b) compares our vorticity on the surface of the body at various early times with

that of Collins and Dennis (1973b). The agreement is remarkable. At $t = 0.5$, one can observe that the flow consists of primary vorticity only but an inflexion point is born. At $t = 1$, the flow has already separated and secondary vorticity (of opposite sign) has appeared. At $t = 2$, the secondary vorticity has strengthened and at $t = 4$ it has weakened. At $t = 8$, the secondary vorticity has developed two inflexion points. At higher Reynolds number values, such inflexion points will be the origin of the formation of a secondary vortex in between the points. Finally, the distribution of the vorticity along the body surface at time $t = 100$ is compared with the vorticity corresponding to the steady solution of the Navier-Stokes equations (Dennis and Chang, 1970) (see figure 2.14 (c)). It then deviates from such values as vortex shedding starts occurring. These features are corroborated by figure 2.14 (d) which displays the drag obtained in this study and the value corresponding to the (unstable) steady flow computed by Dennis and Chang (1970). The fact that the drag of the unsteady solution reaches the drag value of the unstable steady solution of the Navier-Stokes equation before vortex shedding occurs is striking. This point gives significance to the steady solution, although we recall that the size of the bubble is much smaller in the unsteady case. Our time series of the separation angle also compare well with those of Collins and Dennis (1973b) during the early stages and with the constant value of Dennis and Chang (1970) before the symmetry breaks (that is $60 \leq t \leq 100$, see figure 2.14 (e)).

We now concentrate on the visualization of the flow by means of the streamlines which are displayed in figure 2.15 for the time interval $0 \leq t \leq 250$, with a time step $\delta t = 5$. At early times, the streamlines are symmetric, and the bubble grows, becoming more and more elongated. The asymmetry is first very weak and it is difficult to give an estimate of the time at which the symmetry breaking begins from the observation of these flow patterns alone. Here, it can be first detected by observing

the flow structure in the neighborhood of the rear stagnation point of the bubble. Experimentally, Nishioka and Sato (1978) also observed a weak sinusoidal fluctuation near the stagnation point in the wake when the Reynolds number exceeded 48. The most sensitive variable, however, seems to be the lift coefficient which starts oscillating at the instability onset (see figure 2.14 (d)). A more detailed description of this unsteady behavior will be given later in conjunction with figure 2.24. Close to the instability onset, our simulation shows that the closed bubble - or cavity - opens up around the downstream stagnation point of the bubble, as described by Perry *et al.* (1982). The vortex shedding process, however, does not occur immediately after the bubble opening event. Instead, the two elongated vortices undergo an oscillatory motion in which one of the two vortices becomes larger than its companion which, in turn, becomes larger than the other one after some time, etc. This competitive game is interrupted when, at a certain time, the large vortex splits into two smaller vortices, one upstream and one downstream. In our numerical simulation, the upper vortex is the first one to split, and this happens at time $t = 120$ (see figure 2.15). The small vortex located downstream sheds away from the bubble slightly before $t = 125$ while that located upstream is still in contact with the surface of the cylinder. At this time, the remaining upper vortex is much smaller than the lower vortex and the process occurs once again: the large lower vortex splits, in its turn, into two small vortices, one being shed downstream (at time $t = 130$). The lower vortex becomes larger than the upper one (at time $t = 135$), splits and undergoes the cycle once again. This splitting process, observed experimentally by Nayler and Frazer (1917), ends when the vortices are no longer elongated. It is followed by the steady shedding process which is very similar to that described by Perry *et al.* (1982) by means of critical points. In particular, some of our plots can be identified with individual pictures of Perry *et al.*'s figure 2. For instance, our patterns at time $t = 205$ closely resemble

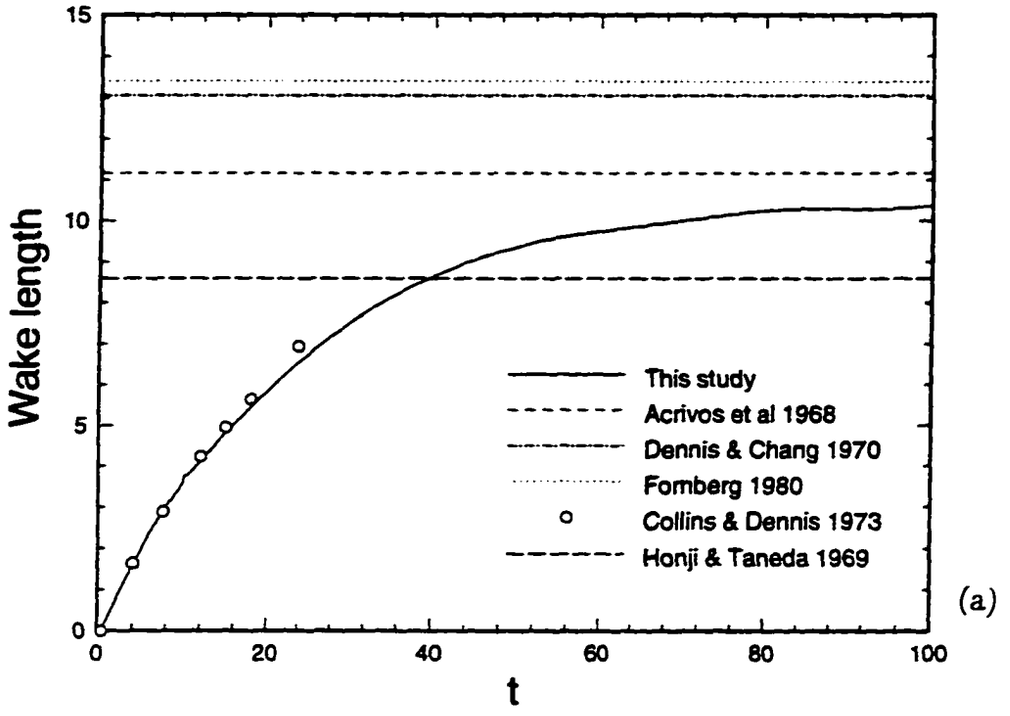

(a)

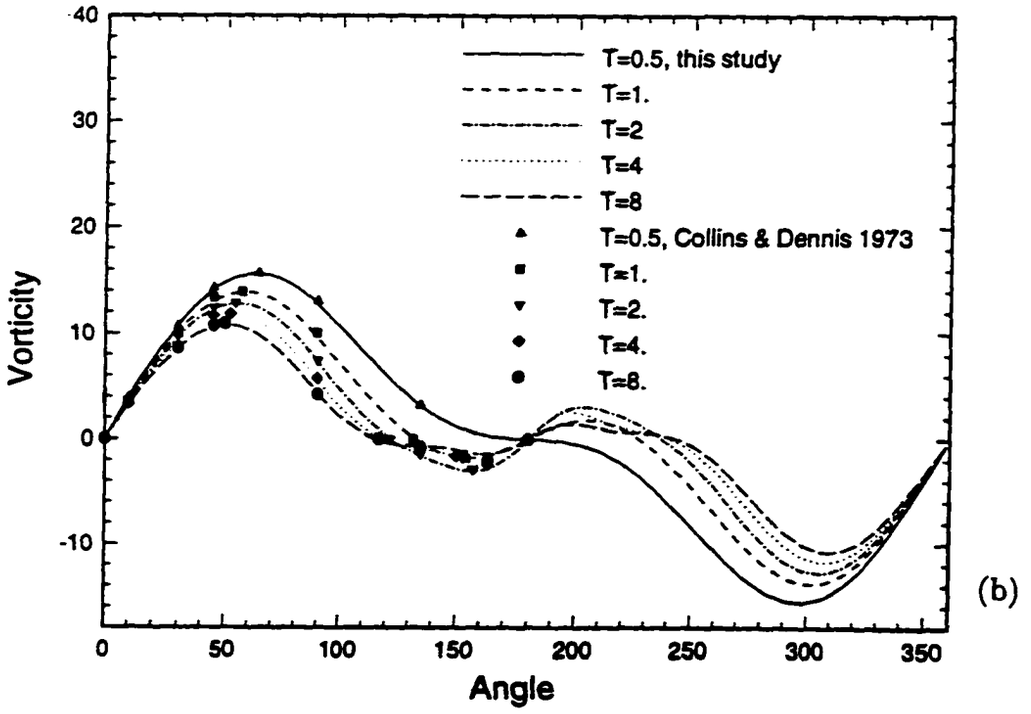

(b)

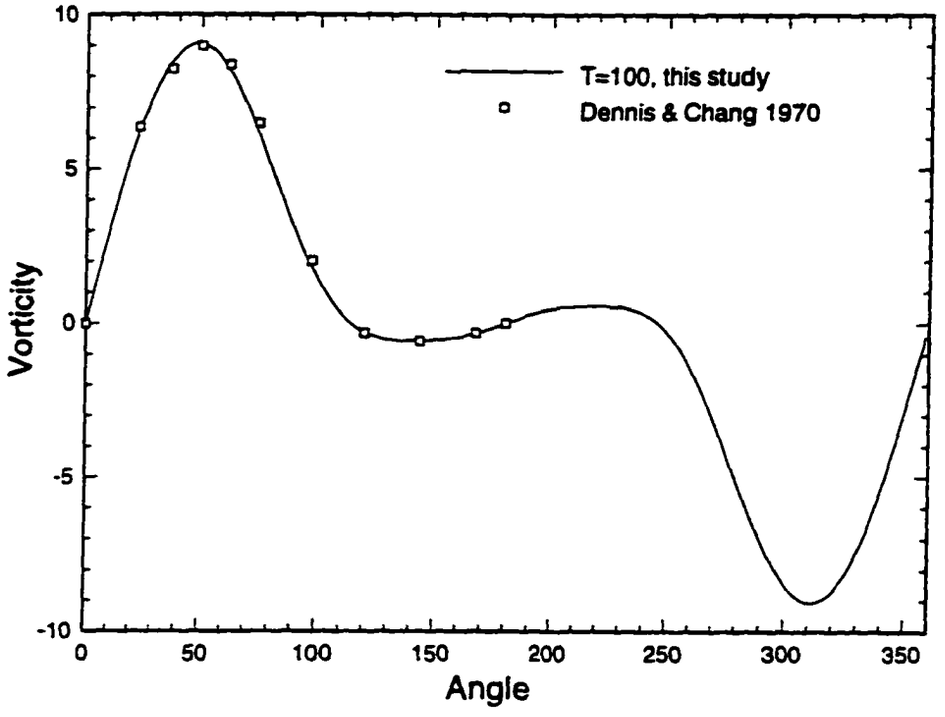

(c)

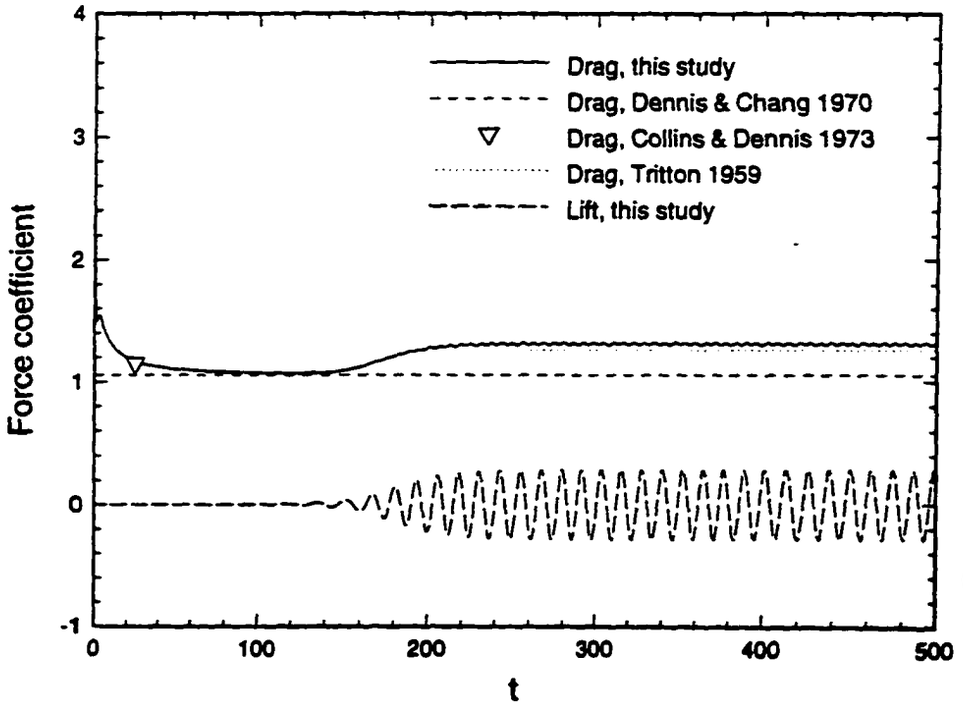

(d)

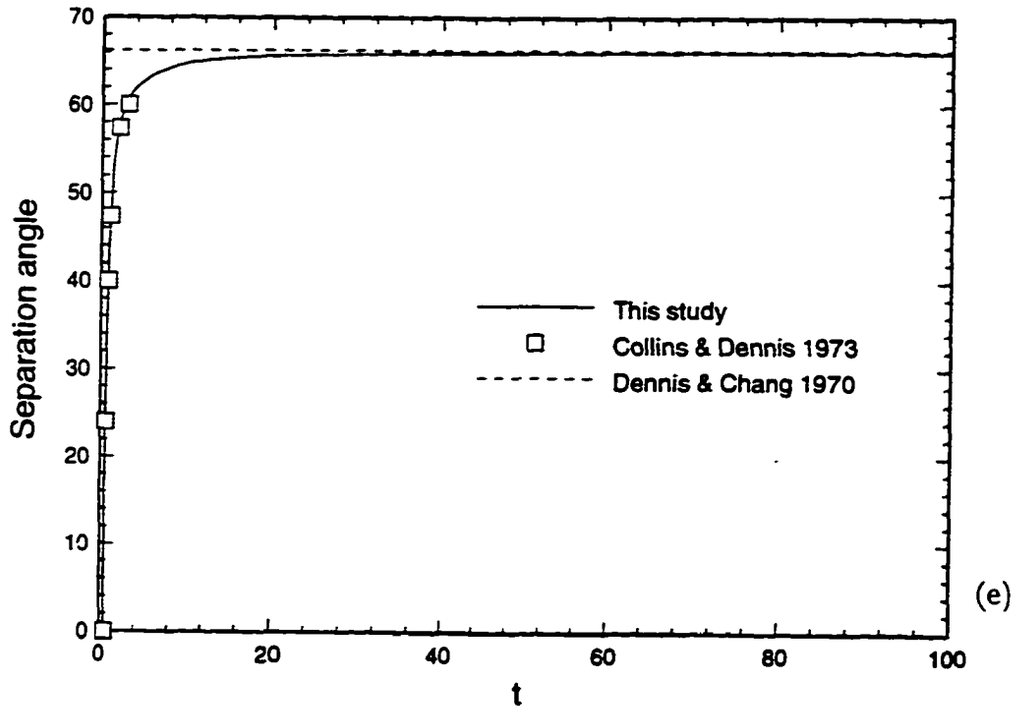

Figure 2.14: The flow computed at the Reynolds number $Re = 100$: (a) time history of the wake length, (b) vorticity on the surface of the body, as a function of the angle expressed in degrees, at various times during the transient, (c) vorticity on the surface of the cylinder, as a function of the angle expressed in degrees, at time $t = 100$, (d) time history of the drag and lift coefficients, (e) time evolution of the separation angle. Our results are compared with others' experimental and numerical data.

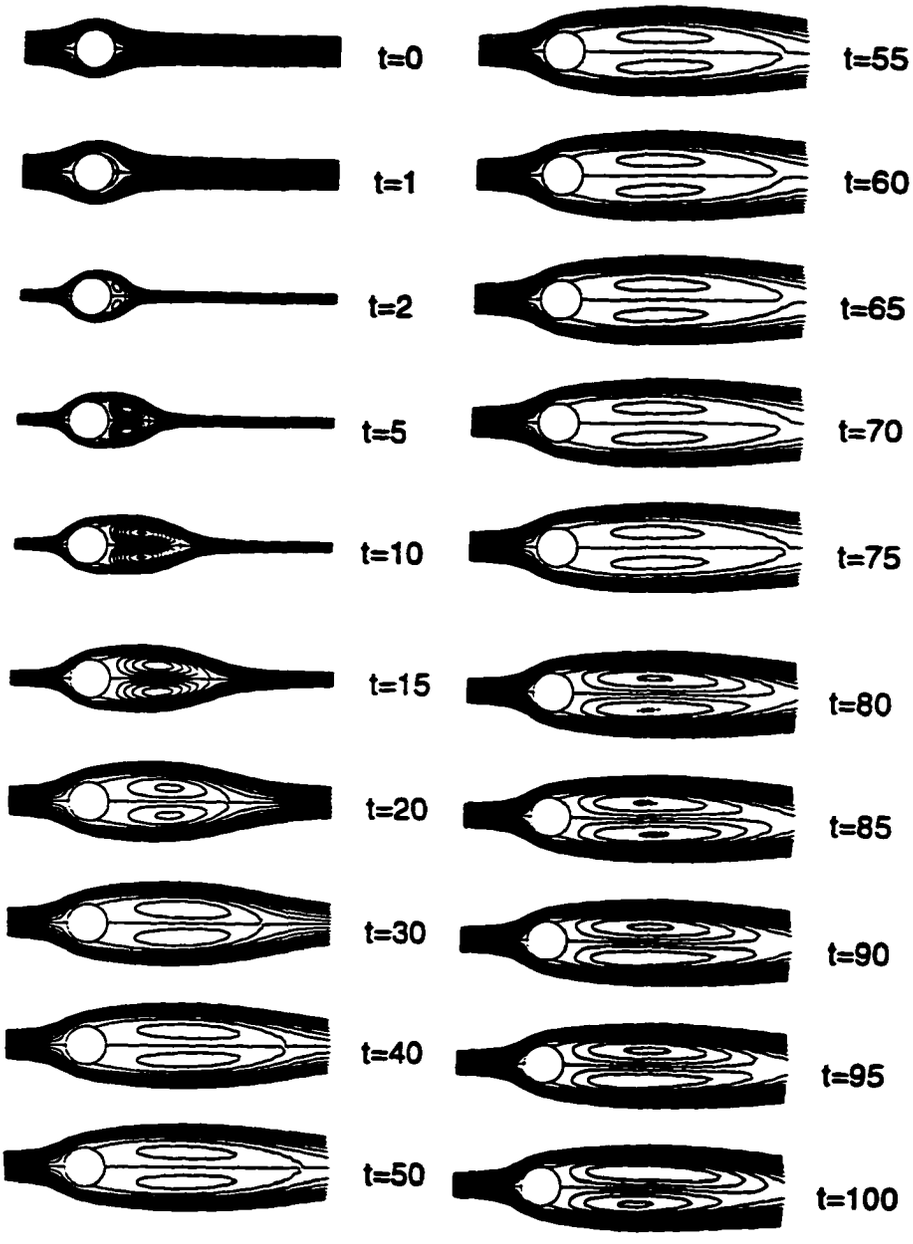

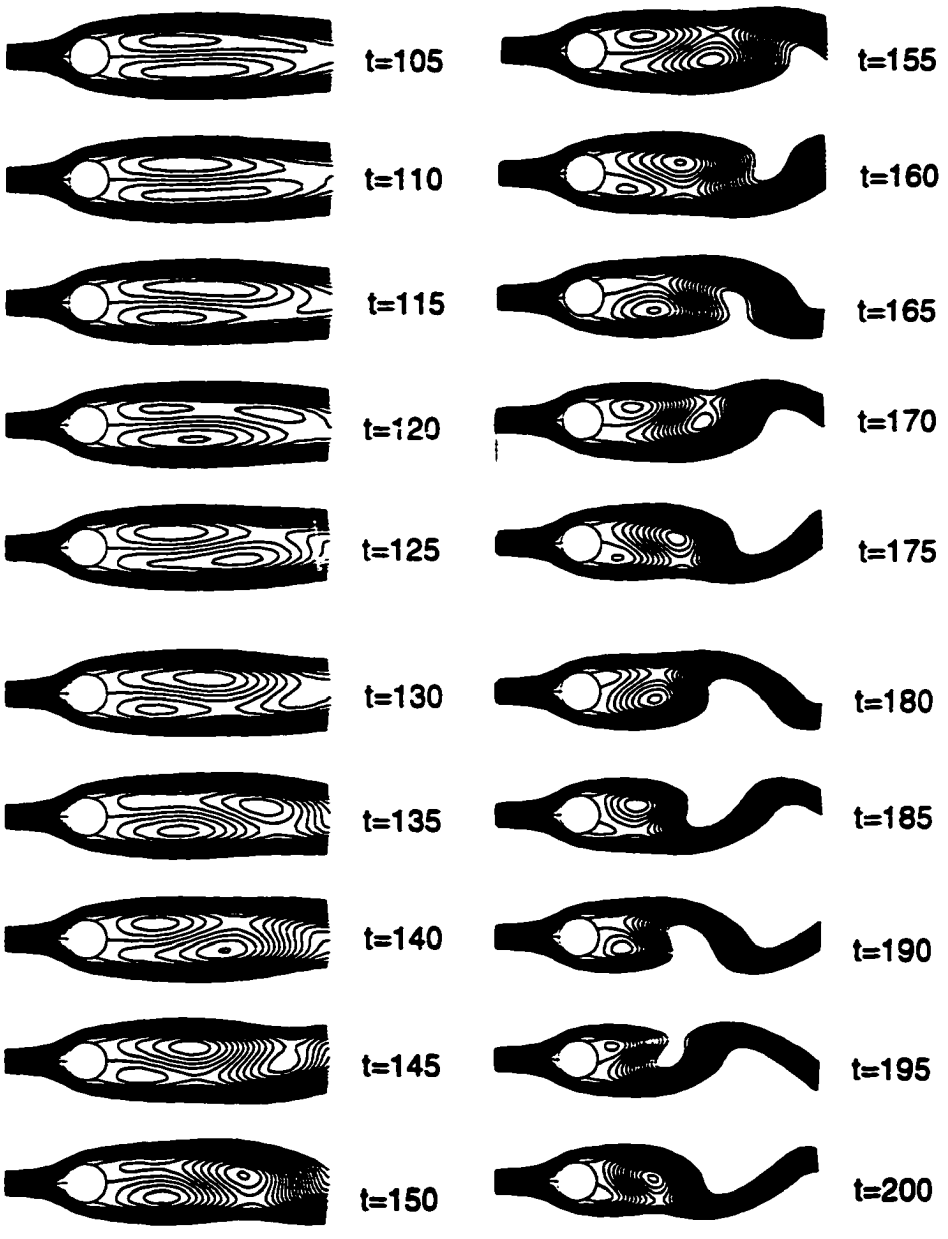

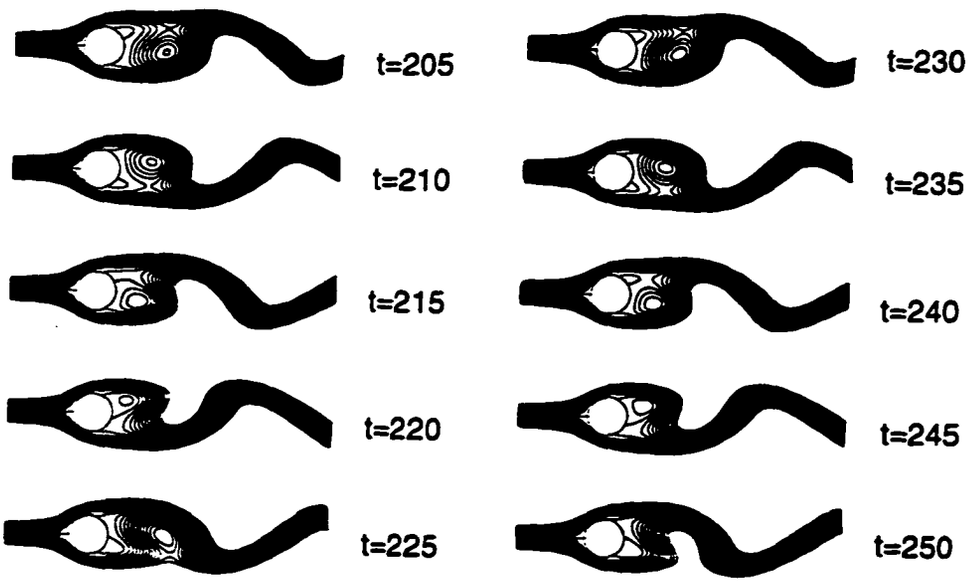

Figure 2.15: Streamlines of the flow at the Reynolds number Re = 100 at various times (see figure 2.14 for other characteristics of the flow). Although the incoming flow is from right to left in our computations, we flip all our streamlines as if the flow was coming from left to right in order to permit a better comparison between our results and those of others.

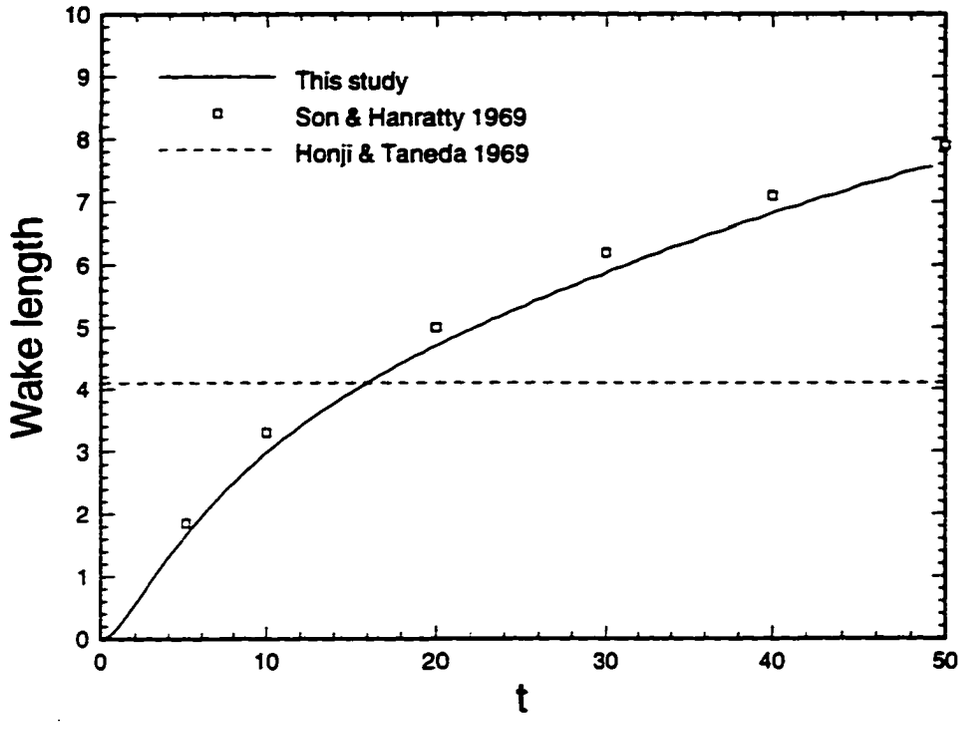

(a)

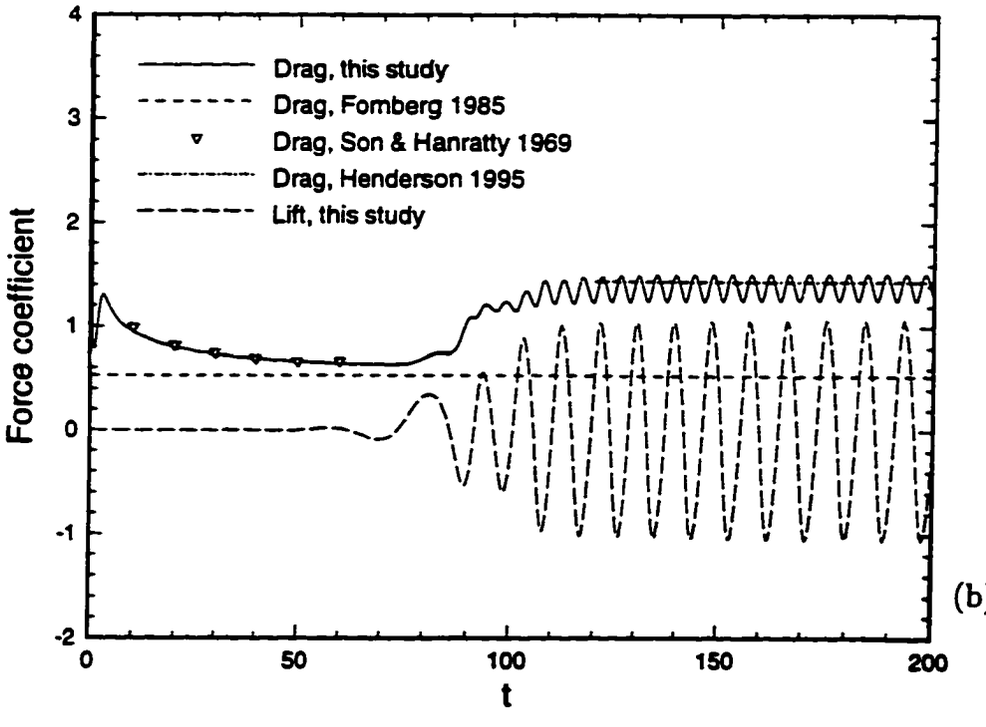

(b)

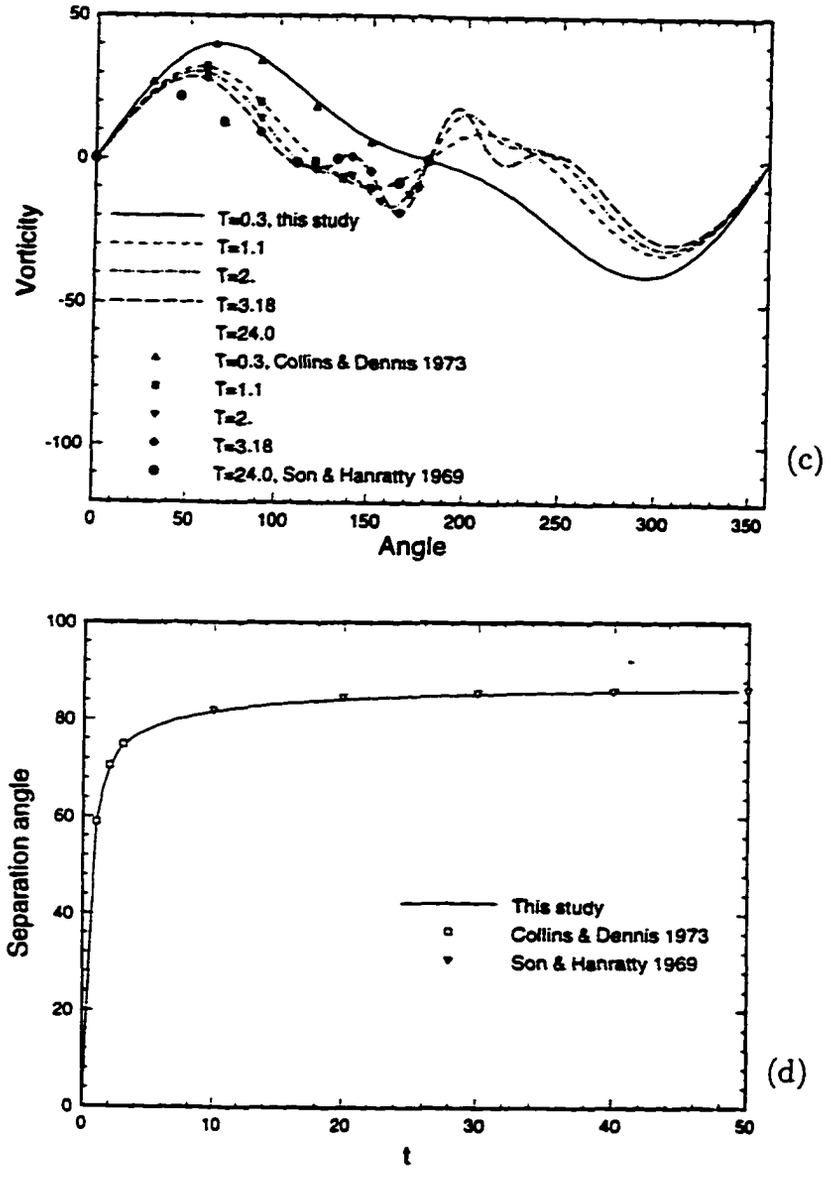

Figure 2.16: The flow computed at the Reynolds number $Re = 500$, with the 750×256 grid: (a) time history of the wake length, (b) time history of the drag and lift coefficients, (c) vorticity on the surface of the body, as a function of the angle expressed in degrees, at various times during the transient, (d) time evolution of the separation angle. Our results are compared with others' experimental and numerical data.

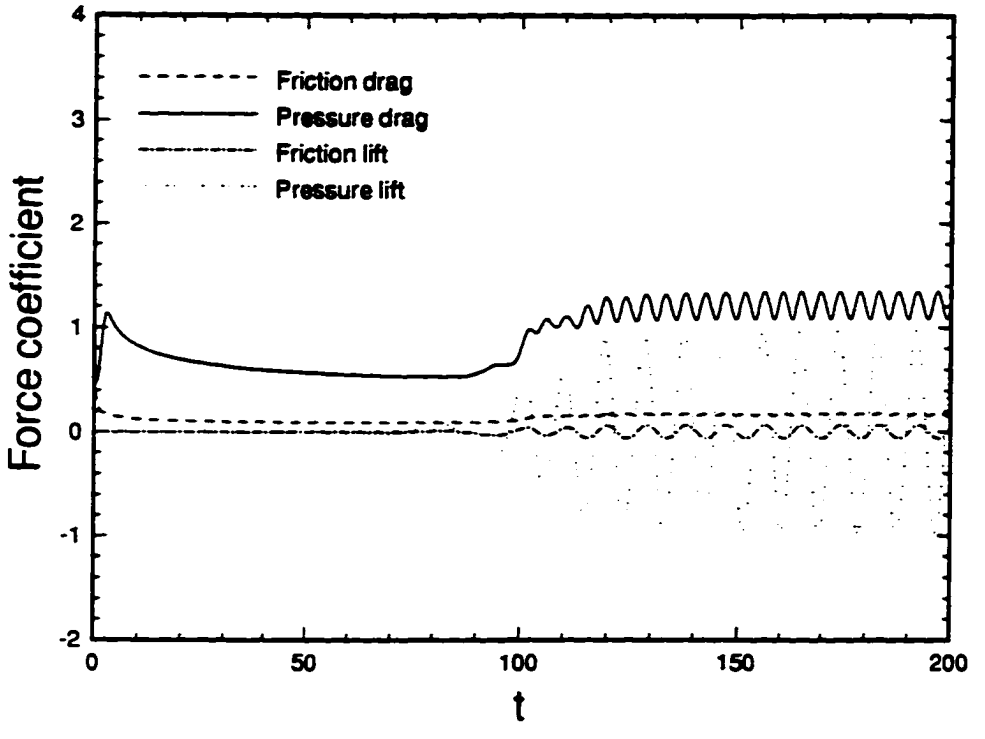

Figure 2.17: Time history of the pressure and friction drag coefficients versus time, at Reynolds number $Re = 500$, computed with the 1200×512 grid showing the negligible portion of the friction coefficients after time $t = 1$ or so. The pressure drag and lift closely resemble the total drag and lift of figure 2.16, except that the symmetry breaking is slightly delayed when the noise level is reduced by the use of a finer grid.

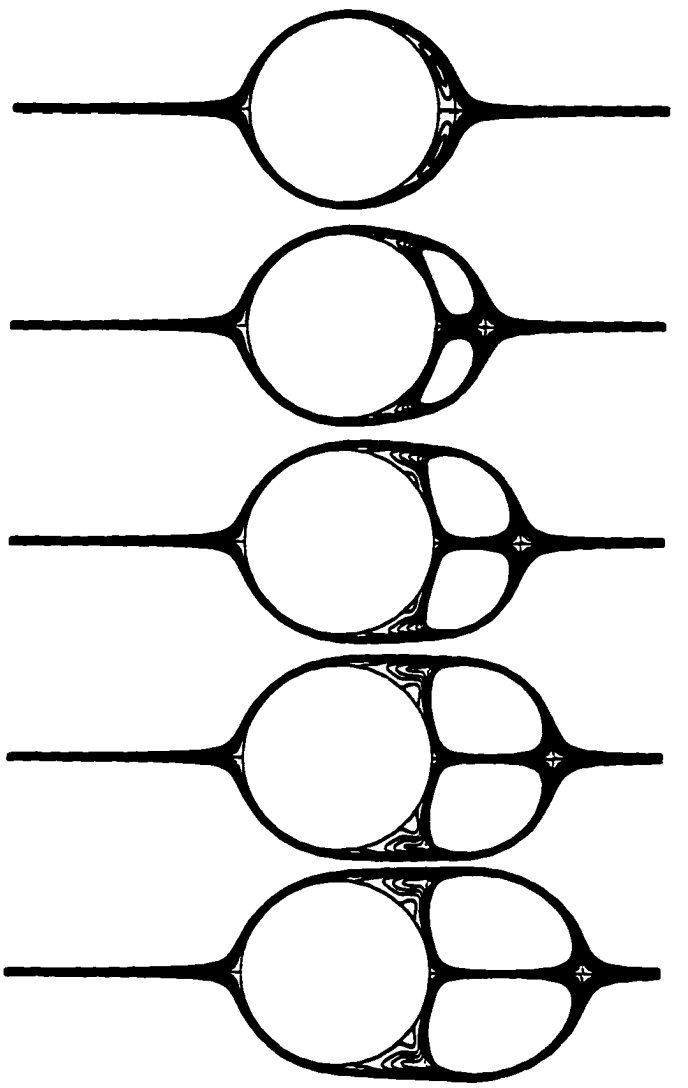

(a)

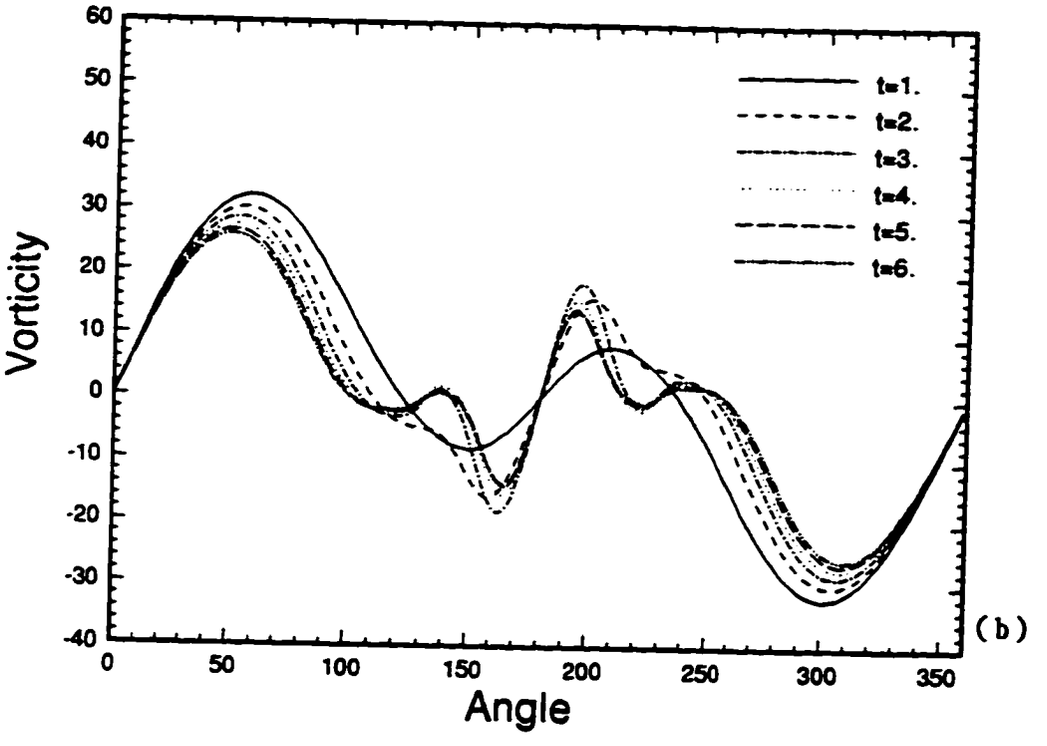

(b)

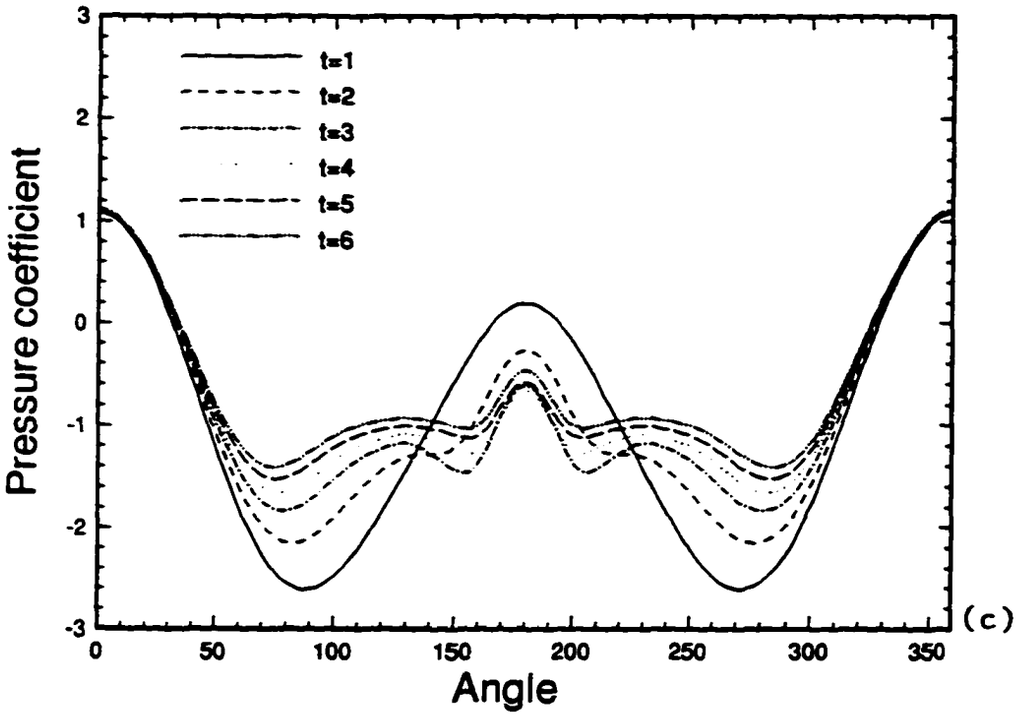

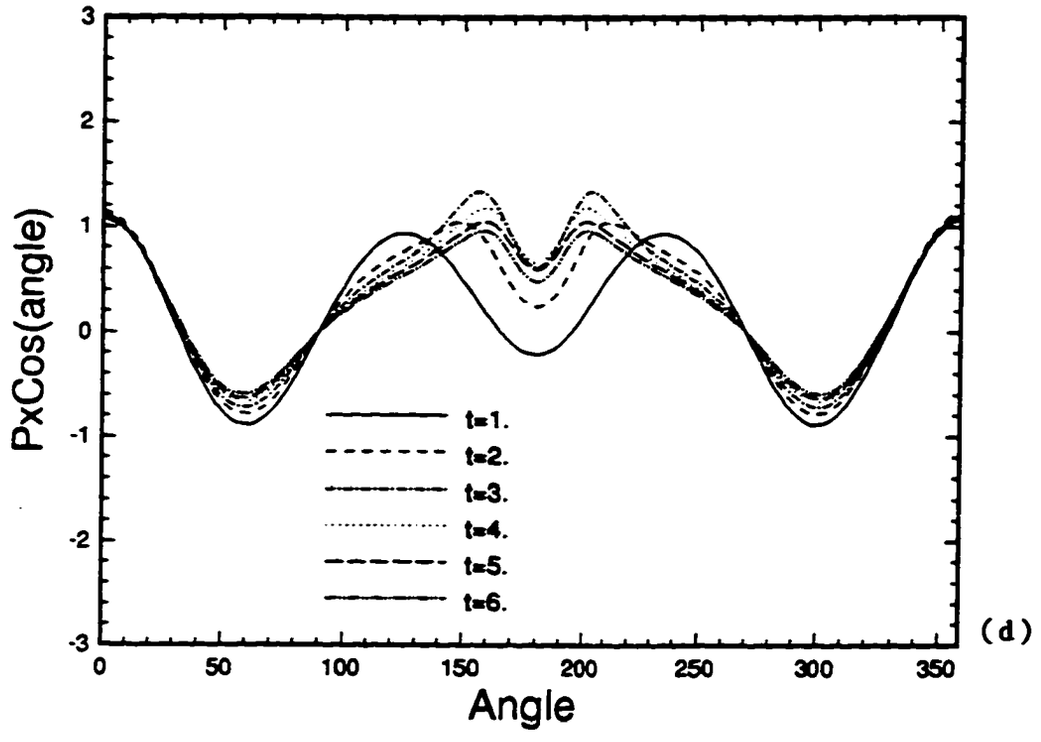

Figure 2.18: The symmetric bubble at the Reynolds number $Re = 500$, computed with the 750×256 grid at various early times $t = 1, 2, 3, 4, 5, 6$: (a) details of the streamlines of the flow, (b) vorticity distribution on the body as a function of the angle expressed in degrees, (c) pressure coefficient on the body as a function of the angle expressed in degrees, (d) projection of the pressure on the horizontal axis, i.e. $Pcos\theta$, as a function of the angle expressed in degrees.

those of figure 2(a) of Perry *et al.* Similarly, our figure 2.15 at $t = 210$ can be identified with figure 2(b) of Perry *et al.* Perhaps, the most important consequence of the symmetry breaking instability is the abrupt change in drag which increases by about 23% during the symmetry breaking event. More precisely, $C_d^{min} = 1.067$ (at $t = 120$) while the mean drag takes the value $C_d^{mean} = 1.31$ after $t = 220$. The time duration over which this increase takes place is about $T = 100$. We will show below that the intensity of the jump increases with Reynolds number, while its time duration decreases.

2.5.3 Computations at $Re = 500$

We first concentrate on the growth of the symmetric vortices at early times. On the one hand, the length of our bubble, as shown in figure 2.16, is much smaller than the wake length of the steady solution ($L_s = 72$, Fornberg (1985)). On the other hand, Honji and Taneda (1969) measured experimentally a largest bubble length $L_{largest} = 4.1$ at $Re = 550$, which is smaller than the value found in this study. We now explore Coutanceau and Defaye's (1991) experimental visualizations of the flow at $Re = 500$. At $t = 8$ (our dimensionless time is twice theirs), the experimental wake is symmetric and the length is about $L_{t=8} = 2.5$ (approximated from their picture), which coincides with our finding, as shown in figure 2.16 (a). Coutanceau and Defaye's flow patterns exhibit an asymmetric shape at time $t = 12$ for $Re = 500$. This symmetry breaking seems to occur earlier than in our simulation, indicating its sensitivity to the noise level presumably higher in an experimental set-up.

In the initial dynamics of the wake, the drag first decreases according to a $t^{-1/2}$ singularity until time $t = 0.95$, then increases until $t = 3.05$ and slowly decreases before suddenly increasing again to finally settle on a periodic motion. In the following, we will return to these variations in the drag coefficient.

Like at the previous Reynolds number, the symmetry seems to break when the drag reaches a value very close to that corresponding to the (unstable) steady solution of the Navier-Stokes equations, C_{Ds}. This is particularly clear in double precision that is, when the noise level is reduced. Indeed numerical noise can trigger the instability early. For example, the discrepancy between the drag coefficient of the steady solution ($C_{Ds} = 0.528$) and our minimal value obtained at $t = 72.6$ is about 22.3% in single precision ($C_d^{min} = 0.646$ with the 500×256 grid) and only 9.8% with the 500×256 grid ($C_d^{min} = 0.58$) at $t = 176.1$ in double precision. The difference can also be reduced further by using a finer 1200×512 grid from which we obtain $C_d^{min} = 0.618$ at $t = 78.4$ in single precision (the discrepancy is then 17%) and $C_d^{min} = 0.566$ at $t = 204$ in double precision (the discrepancy is 7.2%). The symmetry breaking instability is thus sensitive to the noise level. In our simulation, the latter, however, can be reduced considerably more by using double (rather than single) precision than by dividing our mesh size by a factor 2.

Here again, our numerical results concerning both the vorticity distribution on the cylinder surface and the separation angle are in good agreement with previous results (Collins and Dennis, 1973b, Son and Hanratty, 1969) at early times. A detailed comparison can be found in figures 2.16 (c, d). Son and Hanratty's (1969) data for $t < 3.18$ are not reported in figure 2.16 (c) due to the fact that they would be superimposed with those of Collins and Dennis (1973b). The vorticity plot clearly shows that separation has occurred at $t = 1.1$ while it was absent at $t = 0.3$. Like at smaller Reynolds numbers, one observes two inflexion points at $t = 2$ in the secondary vorticity region which develop into a secondary vortex which can be detected at $t = 3.18$ and is still present at $t = 24$.

Figure 2.17 shows that the friction force on the body is negligible compared to the pressure force after $t = 1$ or so. In particular, the two drag increases at $t = 1$

and $t = 90$ are mainly due to the dramatic change in the pressure on the surface of the body. These observations are corroborated by figure (2.18(a, b)) which displays the streamlines and the corresponding vorticity distribution on the body at times $t = 1, 2, 3, 4, 5$. The increase of the drag from $t = 0.95$ to $t = 3.05$, and its decrease afterwards (until $t = 6$), can be explained by the pressure plots of figure 2.18 (c), (d). Particularly, one can see that the secondary vorticity and secondary vortices (that is the part of the flow contained in the interval $130^o \leq \theta \leq 230^o$) play a major role in these drag fluctuations. (Recall that the rear stagnation point is located at $\theta = 180^o$.) In other words, the drag increase and decrease owe to the pressure fluctuations in the separated zone of the flow. During the symmetry breaking phase, the drag undergoes a dramatic raise which can also be easily related to the pressure increase on the cylinder surface, as shown in figure 2.19 which should be read in conjunction with the corresponding streamlines (figure 2.20). In the following qualitative description of the symmetry breaking events, we refer to the *absolute value* of the pressure. At $t = 75$, the lower vortex is slightly larger and stronger than the upper vortex, thus causing a higher pressure on the lower part of the body. At $t = 85$, the strong lower vortex has shed downstream and the upper one has strengthened and moved close to the centerline: the pressure is almost symmetric. At $t = 90$, the upper vortex in its turn has shed downstream and a new vortex is born in the lower half-plane, thus strengthening the pressure there. At $t = 95$, the situation has reversed, the pressure being strong above the centerline. In the time interval $100 < t < 125$, it is easy to carry out the same arguments and find a one-to-one correspondence between the flow structures and the pressure on the body. At each half cycle, the new vortex being created close to the body is stronger and stronger, increasing the pressure as a whole in the transient regime.

Figure 2.20 displays the time history of the streamlines from $t = 5$ to $t = 150$.

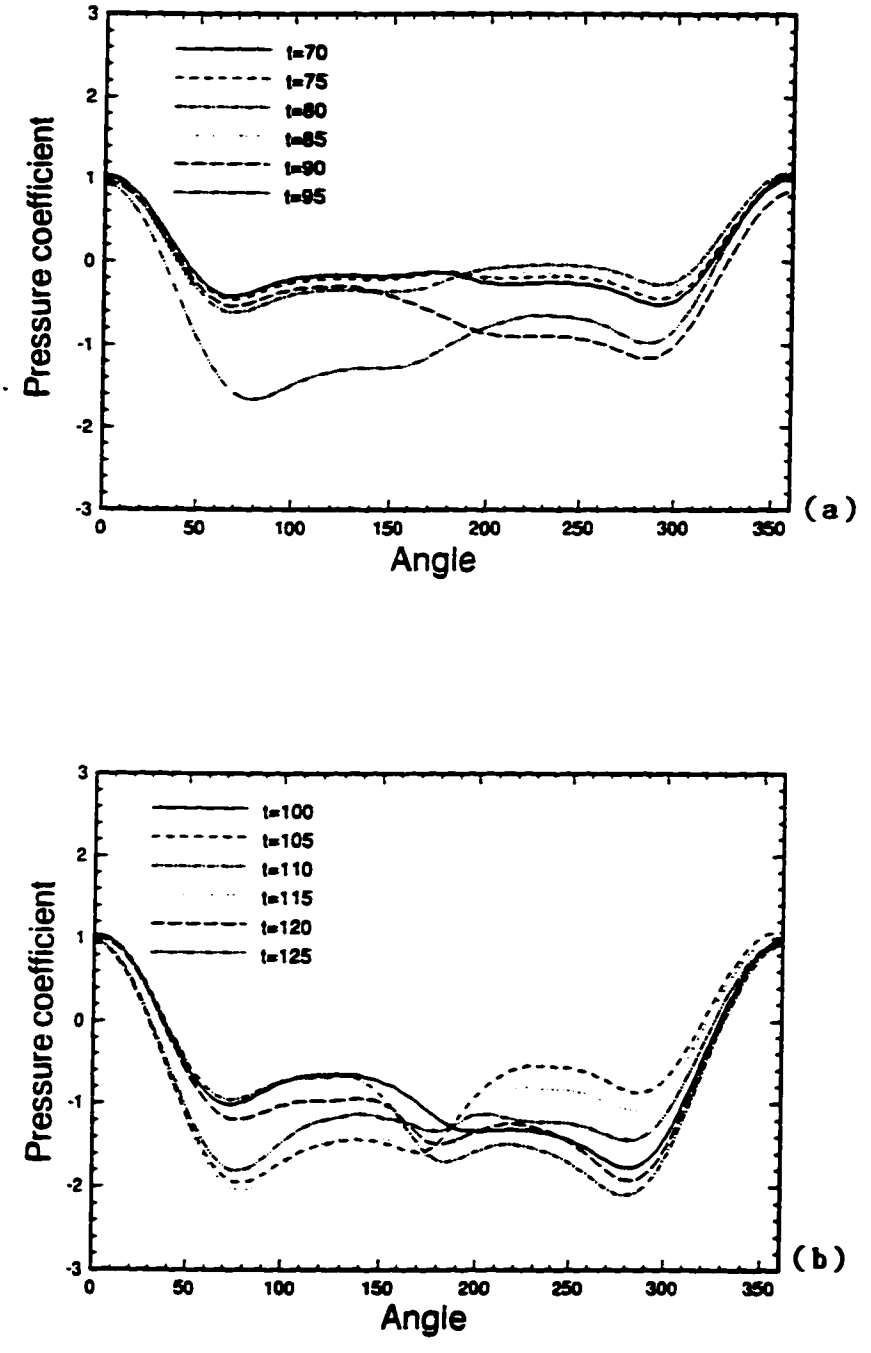

Figure 2.19: Pressure coefficient of the flow on the body at the Reynolds number $Re = 500$, computed with the 750×256 grid: (a) at times $t = 70, 75, 80, 85, 90, 95$, (b) at times $t = 100, 105, 110, 115, 120, 125$.

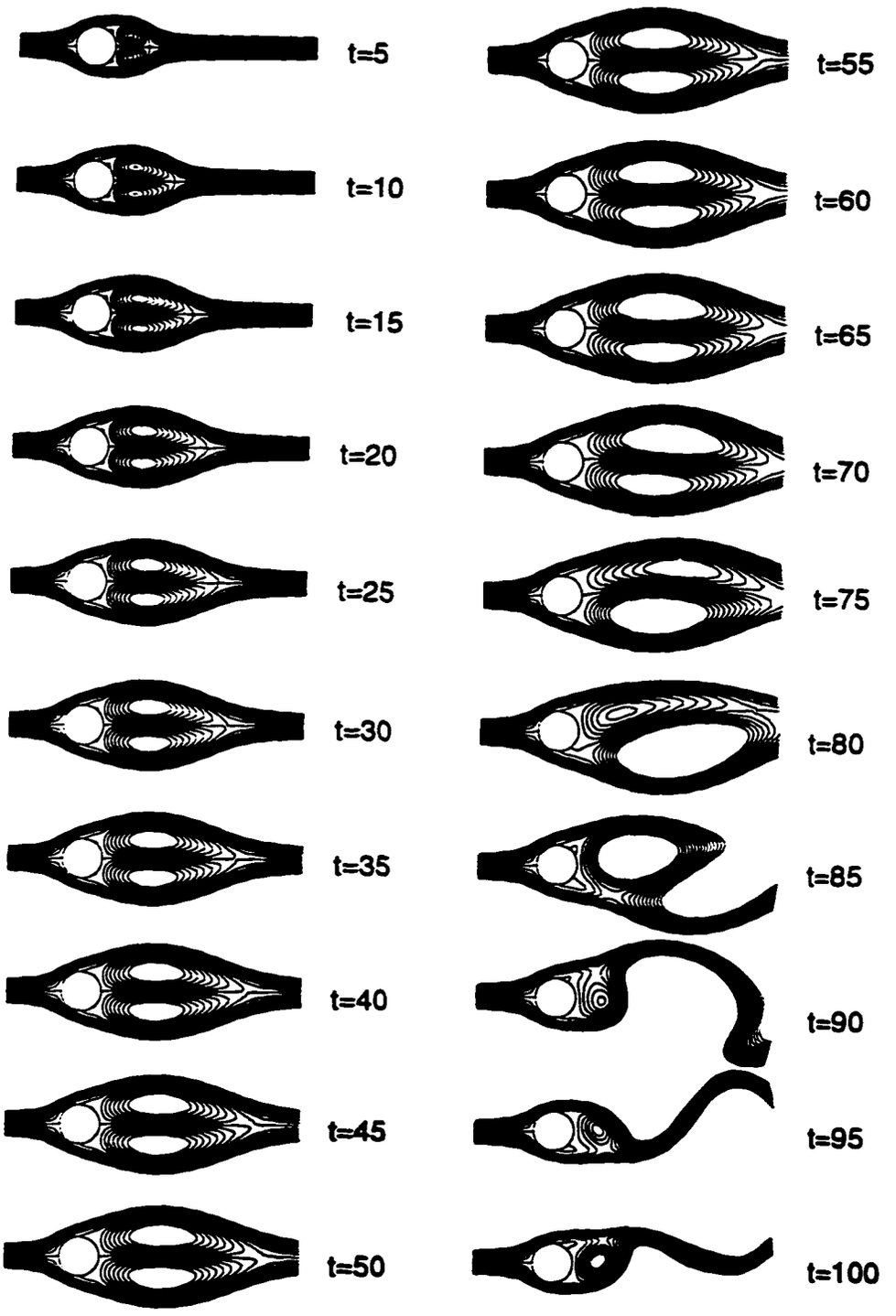

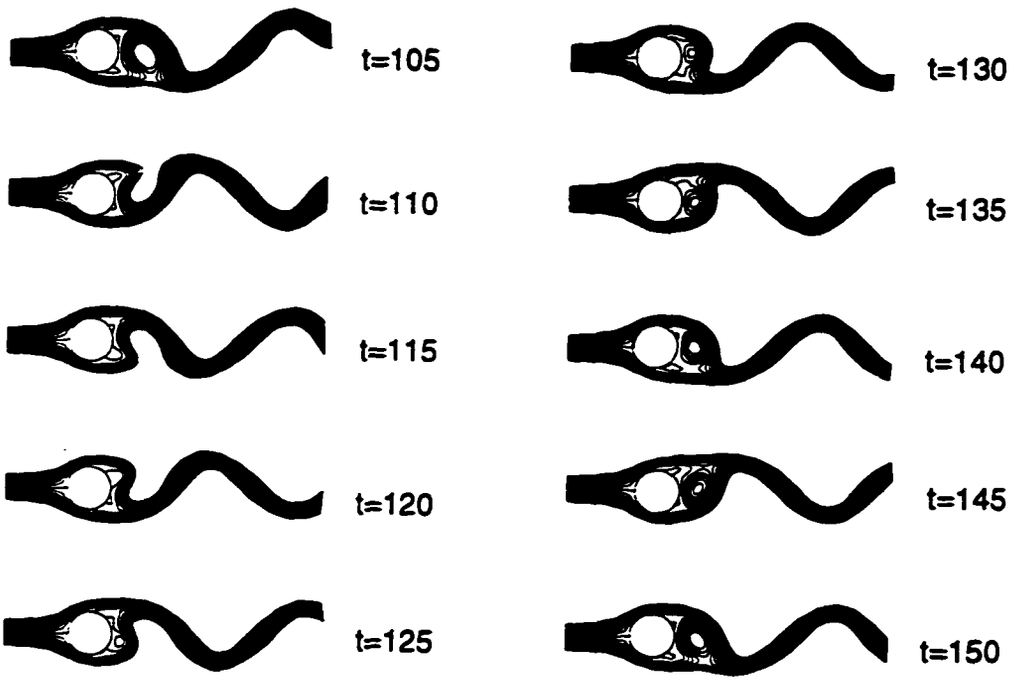

Figure 2.20: Streamlines of the flow at the Reynolds number $Re = 500$ at various times (see figure 2.16 for other characteristics of the flow). Although the incoming flow is from right to left in our computations, we flip all our streamlines as if the flow was coming from left to right in order to permit a better comparison between our results and those of others.

In agreement with the vorticity distribution on the body surface (figure 2.18 (b)), at $t = 5$ the flow has already separated and a secondary vortex is born. Subsequently, one can observe how the wake evolves from a symmetric, closed bubble to a periodic vortex street. Like in the description of our results at $Re = 100$ reported in the previous paragraph, it is easy to see the symmetry breaking at the rear stagnation point of the bubble, followed by the development of the shedding process.

At this Reynolds number, the increase in drag due to the symmetry breaking events followed by the onset of vortex shedding is more dramatic than at $Re = 100$. More precisely, our minimal drag, obtained at $t = 204$, takes the value $C_d^{min} = 0.566$ while the mean drag in the periodic regime $C_d^{mean} = 1.368$, leading to a jump of 142% obtained with the grid 1200×512 and double precision. The time over which the drag abruptly varies from its minimum to the asymptotic value for all grids is about $T = 40$.

After the symmetry starts breaking, the flow evolves into its asymptotic, periodic state in three oscillating periods, as shown by figure (2.20). The vortices start shedding downstream at a distance d from the cylinder, usually referred to as "formation length", which decreases as Reynolds number increases (see, for instance, the vortex streets at $Re = 100$ and $Re = 500$ in figures (2.15), (2.20)).

2.5.4 Computations at $Re = 1000$

Here, the increase of both the separation angle and the wake length with time can be observed in figure 2.21 (a). The wake length is shorter and separation occurs earlier than in the cases of $Re = 500$ and $Re = 100$. Our numerical results show a good agreement with Koumoutsakos and Leonard's (1995) numerical findings in the early stages of the wake development, as shown in figure 2.21 (b, c) which display the angular distribution of the vorticity on the cylinder surface and the time

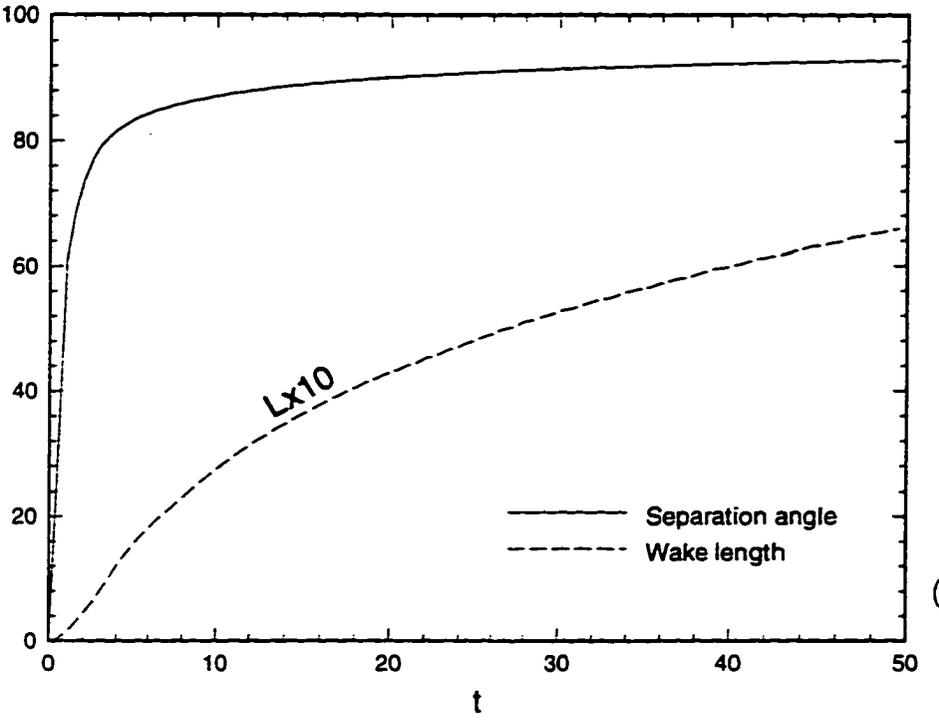

(a)

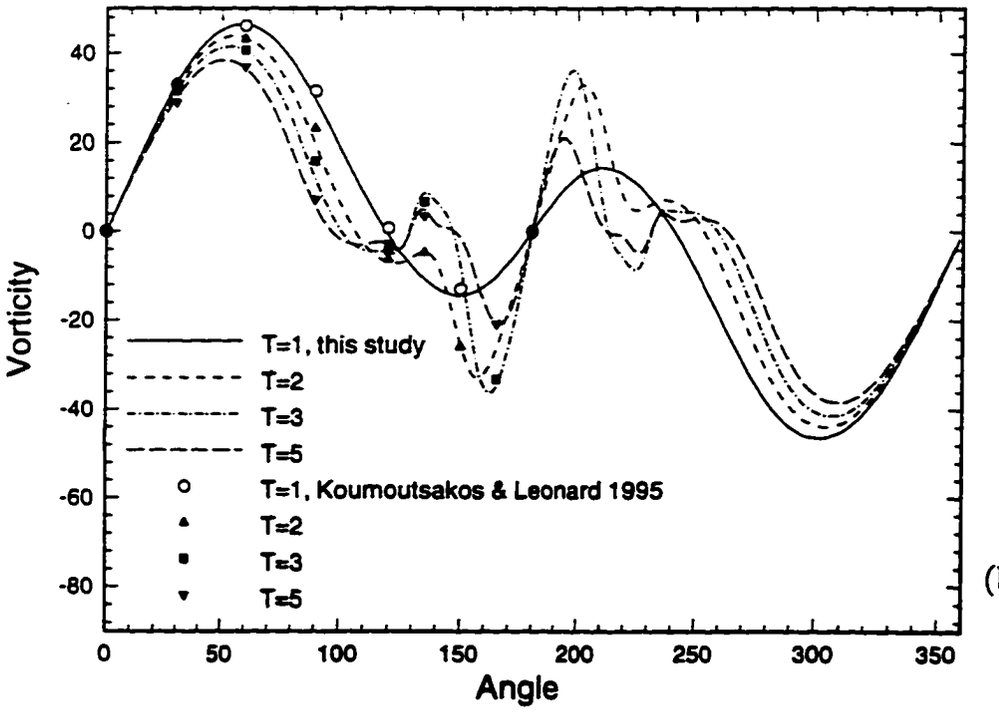

(b)

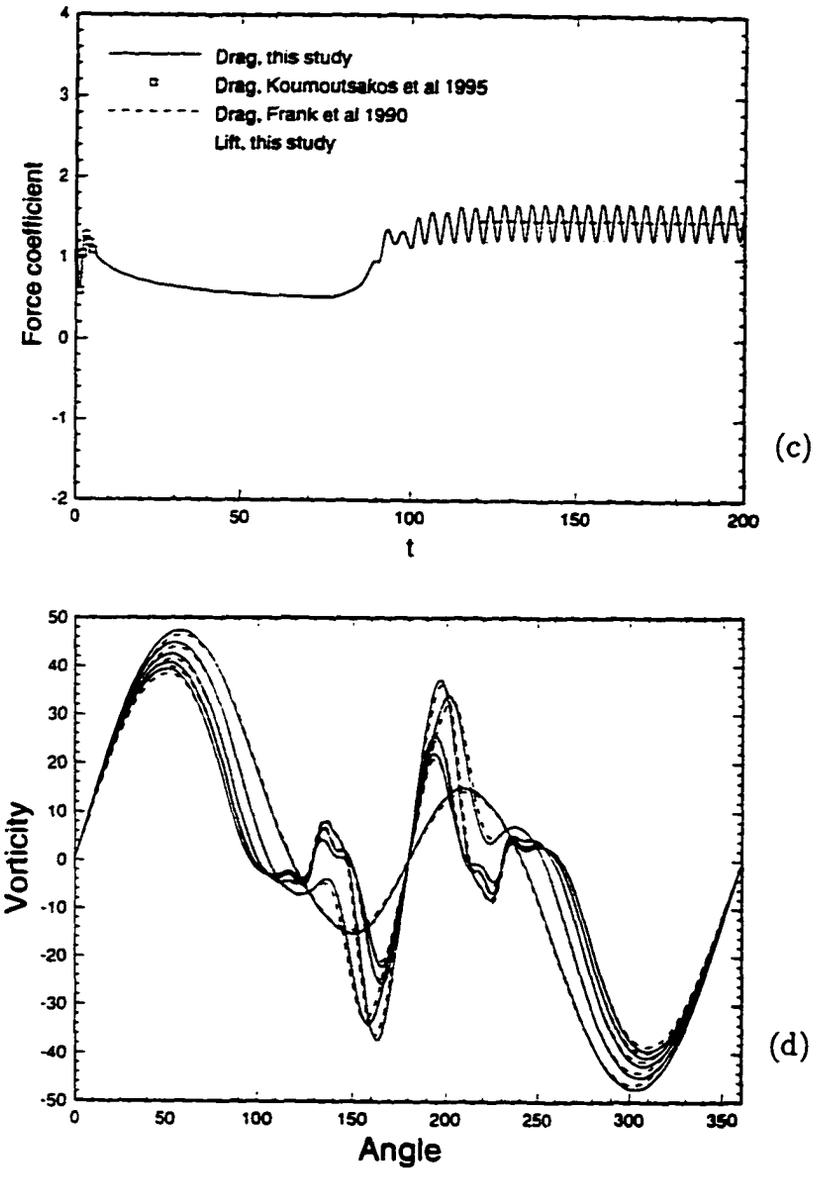

Figure 2.21: The flow computed at the Reynolds number $Re = 1000$ with the 750×256 grid: (a) time history of the wake length L ($10L$ is plotted in dashed line) and time evolution of the separation angle (solid line), (b) vorticity on the surface of the body, as a function of the angle expressed in degrees, at various times during the transient, (c) time history of the drag and lift coefficients, (d) comparison of the vorticity along the surface of the body for two different resolutions : the 750×256 grid and the 1200×512 grid. Our results are compared with others' experimental and numerical data.

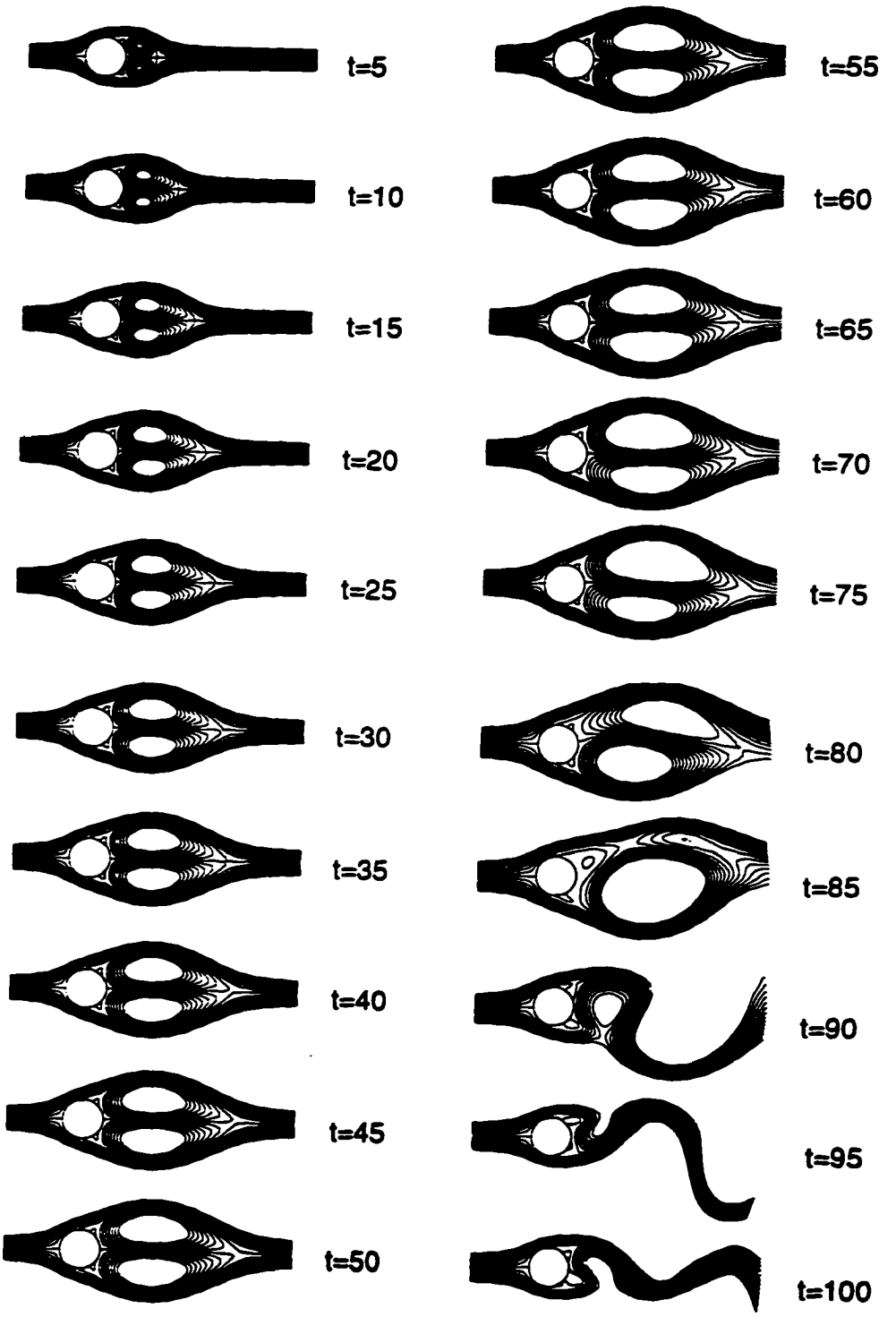

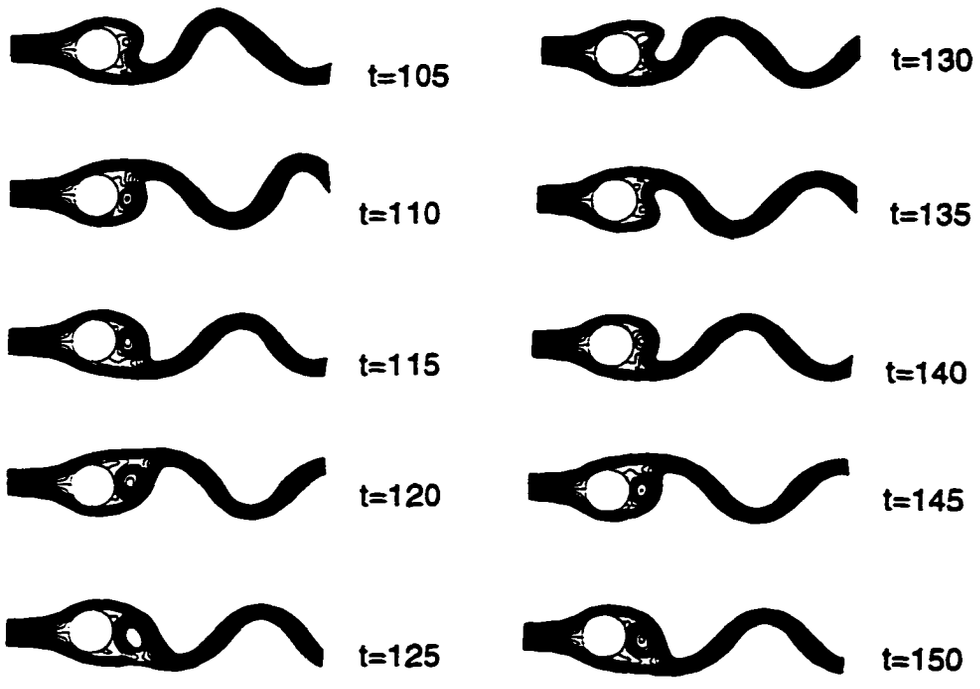

Figure 2.22: Streamlines of the flow at the Reynolds number $Re = 1000$ at various times (see figure 2.21 for other characteristics of the flow).

history of the drag coefficient. The vorticity plot shows that at $t = 1$ a first inflex ion point has appeared and led to separation, manifesting itself as the presence of secondary vorticity in the flow. At $t = 2$ the secondary vorticity develops two new inflexion points and at $t = 3$ the secondary vortex is born. At $t = 5$, the vorticity has developed four new inflexion points which are expected to lead to the formation of tertiary and quaternary vortices, as those observed at higher Reynolds numbers by Koumoutsakos and Leonard (1995). Note that this self-similar repetitive formation of smaller and smaller scales (here vortices) as time evolves is somewhat analogous to the self-similar cascade process identified by Carbone and Aubry (1996) in a turbulent channel flow. It would be interesting to study the scaling characteristics of such a self-similar cascade as the flow transits to turbulence. Our time average drag coefficient in the asymptotic regime is also in good agreement with that reported by Franke *et al.* (1990) (see figure 2.21 (c)). In between the symmetric bubble and the vortex shedding regimes, the drag increases abruptly from a (minimal) value of $C_d^{min} = 0.41$ at time $t = 188.1$ to an oscillatory regime whose time average is $C_d^{mean} = 1.446$, namely the relative jump is 252% with the 1200×512 grid in double precision, which occurs over a time period $T = 40$.

Convergence of these results with spatial resolution and time step was achieved with a reasonable accuracy: refinement of both the numerical grid and the time step by a factor of 2 changed the vorticity distribution on the body by less than 2.5% (see figure 2.21 (d)).

The flow patterns visualized by means of the streamlines in figure 2.22 are very similar to those we reported previously at $Re = 500$, except that the vortices start shedding closer to the cylinder than at lower Reynolds numbers.

2.6 Critical Reynolds number

The transition from the symmetric bubble to asymmetric flow is marked by a Hopf bifurcation (Jackson, 1987, and Zebib, 1987), which is one of the most important features of the wake flow past a circular cylinder. As stated by Zebib (1987), "Although solving the initial-value problem can be used to locate the onset of instabilities, it would be very expensive and does not seem to have been attempted." The objective of this section is to locate the onset of the instability in the unsteady problem. The difficulty lies in the fact that, close to the bifurcation point, the instability takes a long time to develop due to the very small growth rate of the most unstable mode. The critical Reynolds number given by the linear stability analysis is $Re_c = 46.2$ (Jackson 1987) and $Re_c = 40$ (Zebib 1987). The values of Re_c reported in the literature from experimental studies are scattered between $Re_c = 34$ and $Re_c = 48$ (Kovasznay, 1949, Coutanceau and Bouard, 1977, Nishioka and Sato, 1978, Mathis *et al.*, 1984 and Williamson, 1989). An important contribution regarding this issue is that of Shair *et al.* (1963). They found that the value of the critical Reynolds number is strongly influenced by the proximity of the walls in the confining experimental equipment. This problem is avoided in our simulations since our domain is very large. The computational time during which the instability develops is very long in the neighborhood of the critical Reynolds number (about Re = 40-50). In order to predict the critical Reynolds number by numerical simulation, we trigger the instability by using the unstable eigenmode found in Chapter 3, which consists of a vorticity perturbation $\omega_p = 0.05$ at $x_c = 5.5$, y_c =0. Figure 2.23 shows the lift coefficients for the flow at Re = 47, 47.5, 48 and 49 using double precision in a 400 × 256 grid. We recall that the lift coefficient is a good indicator for the symmetry breaking instability. The perturbation is introduced in the four cases at $t = 100$ and released afterward. At $Re = 47$, the perturbation decays, indicating that the flow is stable.

In contrast, at $Re = 48$ and 49, the perturbations are clearly amplified, meaning that the flows are unstable. However, at $Re = 47.5$, the perturbation remains constant during the integration time ($T_{max} = 800$). So the critical Reynolds number is close to 47.5, which is in good agreement with the values obtained from recent experiments. $Re_c = 47$ (Mathis *et al.*, 1984, for an infinitely long cylinder) and $Re_c = 47.9$ (Williamson, 1989, from parallel-shedding measurements). All the previous critical Reynolds number values agree rather well with the result obtained by Jackson (1987) from the linear stability analysis of the steady solution ($Re_c = 46.184$). It differs, however, from the value $Re_c = 40$ found by Zebib (1987) who also performed the linear stability analysis. This discrepancy needs further investigations.

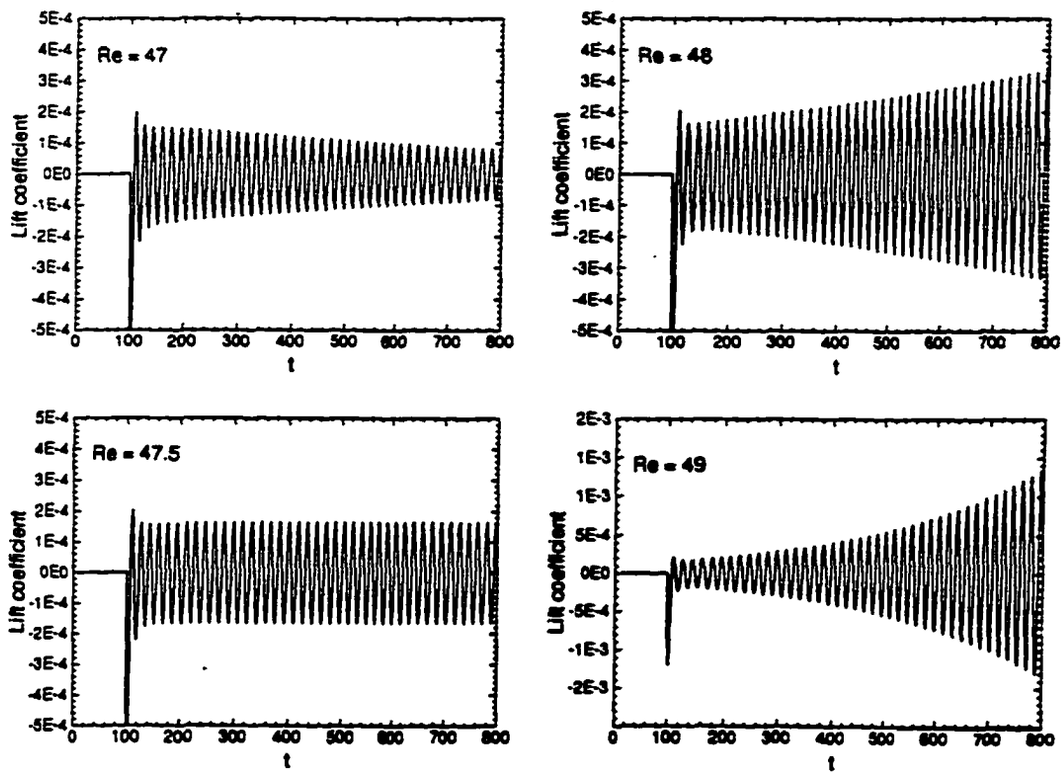

Figure 2.23: Lift coefficient for the flow at $Re = 47$, 47.5, 48 and 49 using 400×256 grid points and double precision.

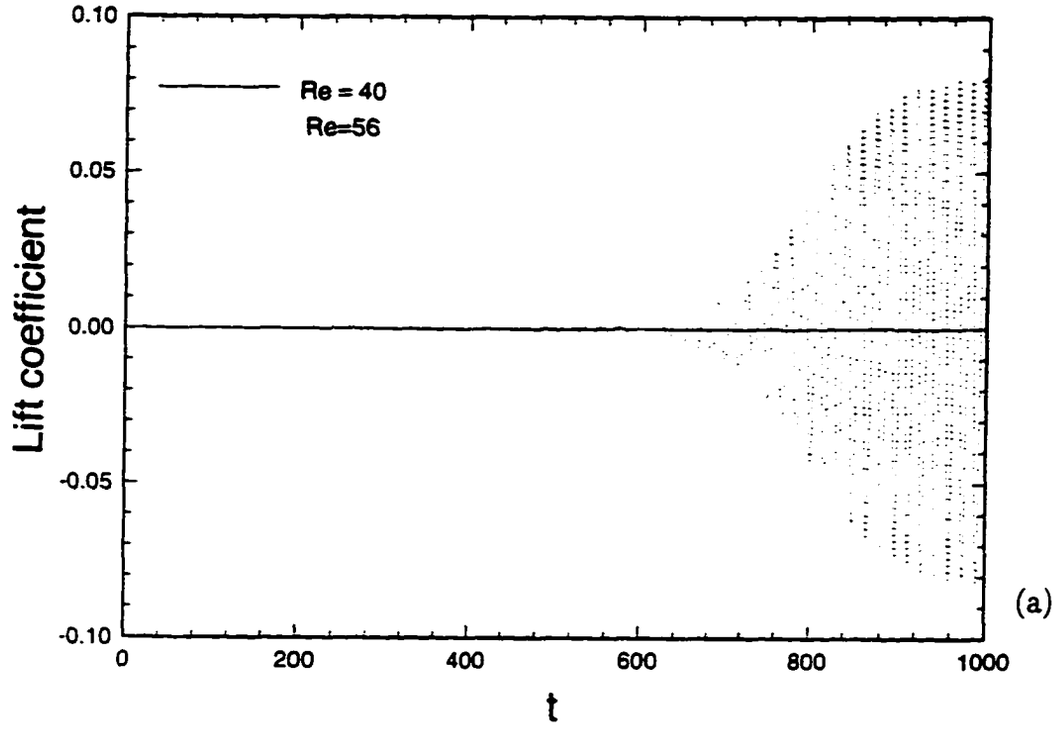

(a)

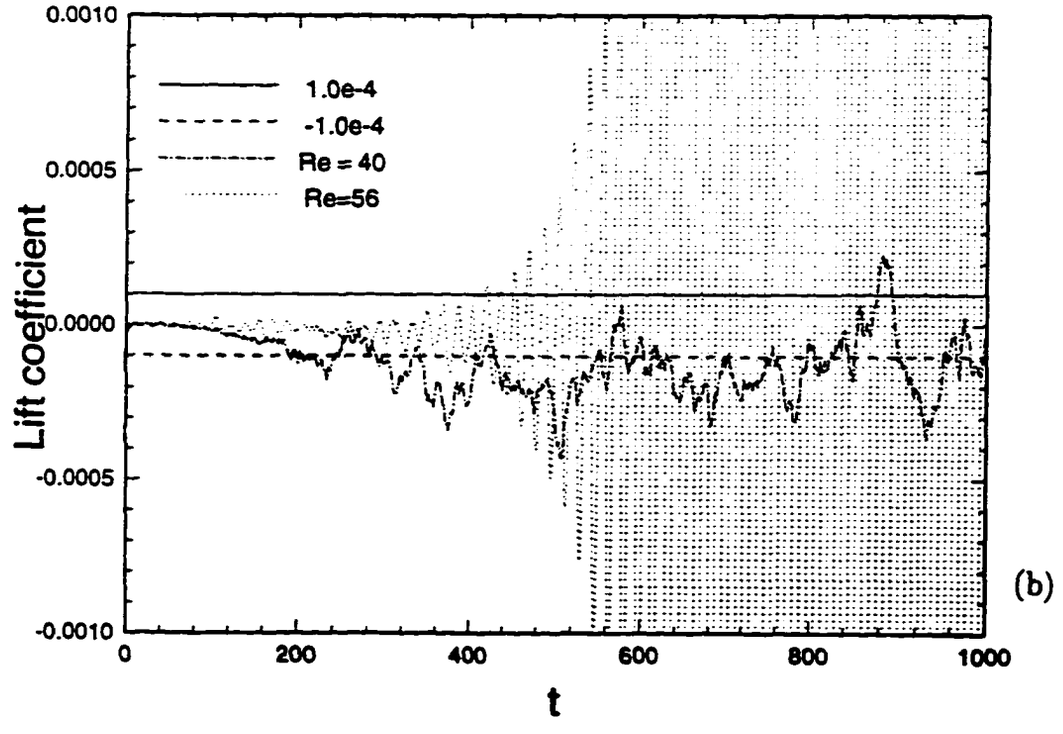

(b)

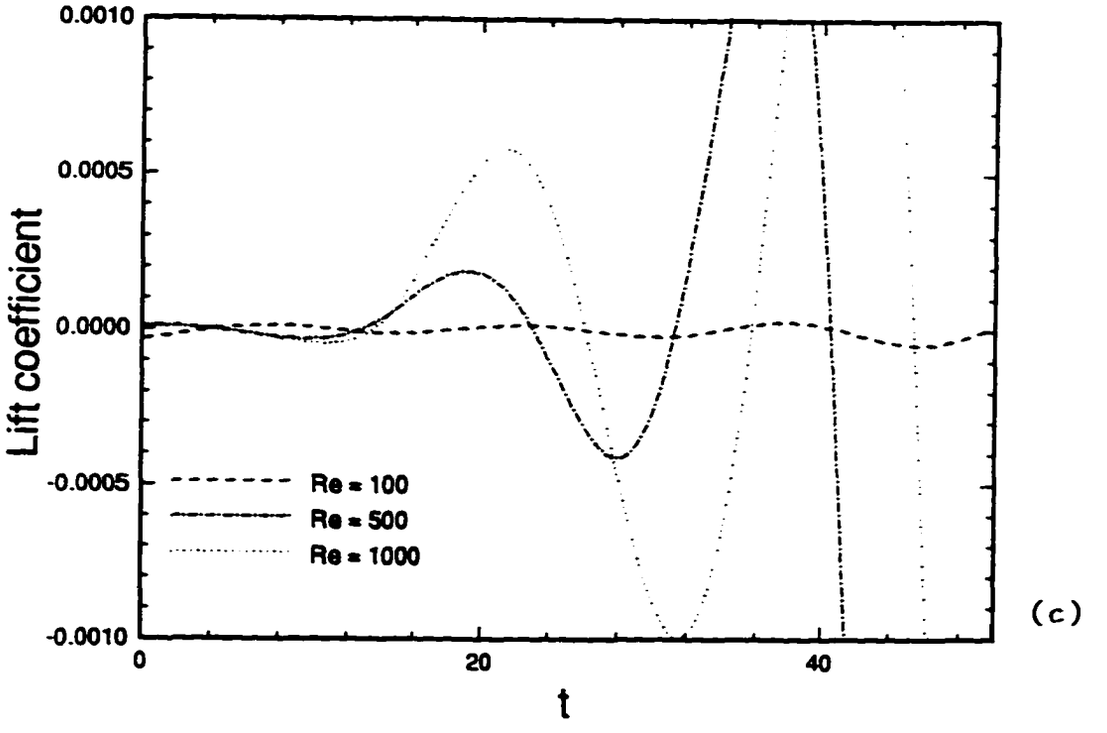

Figure 2.24: Time dependency of the lift coefficient for various Reynolds numbers: $Re = 40, 56, 100, 500, 1000$, (a) at the Reynolds number $Re = 40$ and $Re = 56$, (b) zoom of (a) showing the details of the amplitude variations, (c) at the Reynolds numbers $Re = 100$, $Re = 500$ and $Re = 1000$.

2.7 Summary and concluding remarks

The impulsively started flow past a circular cylinder was simulated for the first time to our knowledge from its initial state at rest to its final periodic state in the range of Reynolds numbers from $Re = 20$ to $Re = 1000$. Our code is based on the integration of the two-dimensional Navier-Stokes equations. At all Reynolds numbers, the flow consists of a bubble or cavity invariant by reflection symmetry through the mid-plane at early times. The cavity encloses two vortices which are images of one another through reflection symmetry. As time increases, the symmetry breaks and an asymmetric, oscillatory motion occurs among the two vortices, one vortex, say the upper one, becoming larger than the other one. After some time, the lower vortex becomes, in its turn, larger than the upper one, and the whole process occurs again. After a few periods, this temporal dynamics becomes periodic in both space and time, due to the appearance of shedding. The breaking of the instantaneous reflection symmetry occurs such that the symmetry remains, but in a space time sense. In other words, after the symmetry breaking has occurred, we can find the image by symmetry of the lower (resp. upper) vortex in the upper (resp. lower) vortex *at a later time, rather than at the same time.* Although the symmetry breaking seems to occur later in our numerical simulations than in experiments for $Re \geq 56$, early time oscillations of the lift indicate that the symmetry breaks at early times. Figure 2.24(a) shows the zero constant lift for $Re = 40$ (confirming the stability of the flow) and the oscillating lift for $Re = 56$. A zoom on the lift amplitude (figure 2.24(b)) points out a clear oscillation at $Re = 56$ at early times while no pattern can be observed at $Re = 40$. This feature is even more pronounced at higher Reynolds numbers. Indeed, figure 2.24(c) clearly exhibits lift oscillations almost initially.

It is of high interest to understand how the flow, through all its complex motions, breaks the instantaneous reflection symmetry and satisfies the space-time

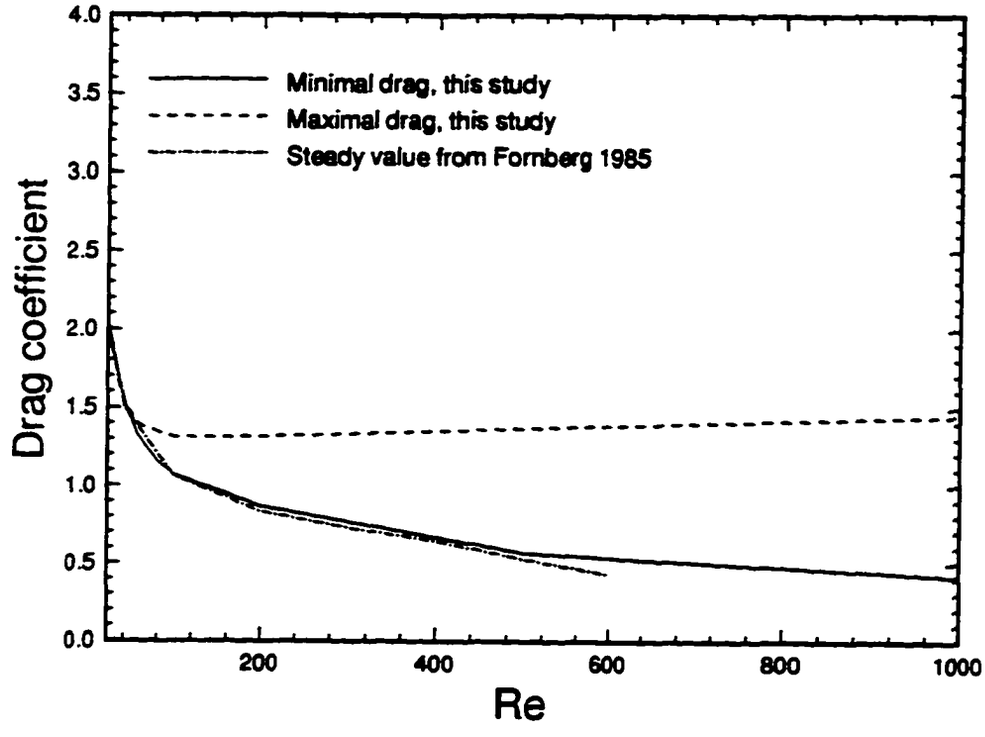

Figure 2.25: Increase of the drag as the flow undergoes the symmetry breaking. Minimal drag reached before the drag increase (solid line), mean drag of the Karman vortex street (dashed line), drag of the steady solution as computed by Fornberg (dot-dashed line). One can observe that the amplitude of the drag jump increases with Reynolds number.

symmetry (Aubry *et al.*, 1992, Cao, 1993). Not only is this important from a fundamental approach but also from the point of view of applications, as we have found that such a symmetry breaking is responsible for an important jump in the drag coefficient. This abrupt raise can be traced in the evolution of the pressure on the body, as we have shown at $Re = 500$, and increases with Reynolds number, since the minimal drag value preceding the jump decreases while the (time) average value of the drag in the asymptotic state increases (see figure 2.25). The maximal magnitude of the jump in drag can be estimated by the difference between the drag of the steady solutions (Fornberg 1985) and the mean drag of the asymptotic state. This estimate leads to 23% at $Re = 100$ and 159% at $Re = 500$ (compare to 23% and 142 % in this paper). Unfortunately, Fornberg (1985) did not compute the steady solution at $Re = 1000$. We have found a drag jump of 241% at this Reynolds number. However, the real drag jump in an individual (physical or numerical) experiment could be smaller as it depends on the noise level.

In addition, the dimensionless time over which the jump occurs decreases with Reynolds number. It is about $T = 100$ for $Re = 100$ and $T = 40$ for $Re = 500$ and $Re = 1000$. The corresponding real time (recall that $\tilde{t} = ta/U_\infty$) could be very small, particularly for a cylinder with a small diameter and high incoming velocity.

Asymptotic wake flows at high Reynolds numbers ($Re > 180$) are known to be three-dimensional. It is expected, however, that the flow remain two-dimensional during the initial phase of the transient. It is not clear at what time the three-dimensional instability will develop and how it will influence the substantial jump in drag value reported in this chapter. Two-dimensional simulations are known to over-predict the drag and lift due to the (statistically steady) Karman vortex street, compared with full three-dimensional computations. Mittal and Balachandar's (1995) numerical simulations show an artificial increase of 16% at $Re = 525$ due to the

restriction to two-dimensionality. Here, there are two possibilities, either the three-dimensional instability develops after the two-dimensional Karman vortex street has settled down, or it occurs before the end of the transient. In the first case, there will be no three-dimensional effect on the jump in drag value described in this chapter. In the second case, the three-dimensional effect will be present and will manifest itself by the fact that the upper value of the jump is lower. In the latter situation, the decrease in drag value due to three-dimensionality should be much smaller than the increase due to symmetry breaking. At $Re = 525$, for instance, the former is 16% while the latter is 142%: this still leaves a substantial increase in drag during the transient behavior, even in presence of three-dimensionality. So far, we have omitted the fact that three-dimensionality can manifest itself before the time at which the drag starts increasing dramatically. If this is indeed the case, it could either raise or lower the minimal drag value at the beginning of the jump. In any case, we should mention that Seto *et al.* (1991) did observe experimentally an important increase in drag value at high Reynolds number (between $7000 \leq Re \leq 9000$). We will investigate the consequences of three-dimensionality on this effect numerically in the near future. If the previous effect does persist in presence of three-dimensional effects, the findings of this chapter, which should have important consequences on many applications related to the transient behavior of vehicles undergoing fast accelerations, deserve further investigations.

We recall that the instability described in this chapter is triggered, except in the neighborhood of the critical Reynolds number, by round-off and discretization errors. Anderson *et al.* (1990) commented on the issue of accuracy and convergence of numerical calculations in situations in which the exact solution of the Navier-Stokes equations is unstable. They claimed that "if one does not introduce perturbations, but relies on numerical error to push the computed solution away from the unstable

one, then the computed solution is an uncontrolled consequence of discretization and round-off errors". We disagree with this statement in the sense that both the growth rate of the perturbation and the asymptotic stable solution the flow reaches should be identical whether the perturbation consists of round-off errors or whether it is imposed as the most unstable mode. Indeed, for a linearly unstable flow the perturbation will be amplified according to $A_0 e^{\lambda t}$ ($\lambda > 0$), where A_0 is the initial perturbation and λ refers to the growth rate. Of course, the amplitude (A_0) is perturbation dependent but the growth rate λ should not be. In order to prove these points, we now compare the numerical experiments obtained without any artificial perturbation and with the perturbation previously described. Figure 2.26 shows the results at $Re = 56$ in both cases. In the case without any artificial perturbation (figure 2.26 (a)), the discretization and round-off errors trigger the instability which develops at a later time. In the artificially perturbed case (figure 2.26 (b)) in which the perturbation is introduced at $t = 100$ and released afterward, the instability develops immediately. It is clear that the growth rates are identical in both cases, but the transient behaviors are different due to the fact that two different perturbations lead to different time scales for the development of the instability. We also calculate the growth rate at $Re = 100$ for a 1200×512 grid and a 400×256 grid. The growth rates are $\lambda = 0.059$ and $\lambda = 0.061$, respectively. Figure 2.27 shows the growth rate against Reynolds number compared with the experimental results of Strykowski (1986) and the numerical results of Strykowski and Hannemann (1991). The linear relationship found by these authors between λRe and Re up to $Re = 100$ is confirmed here. Our growth rate curve, however, is below their curve.

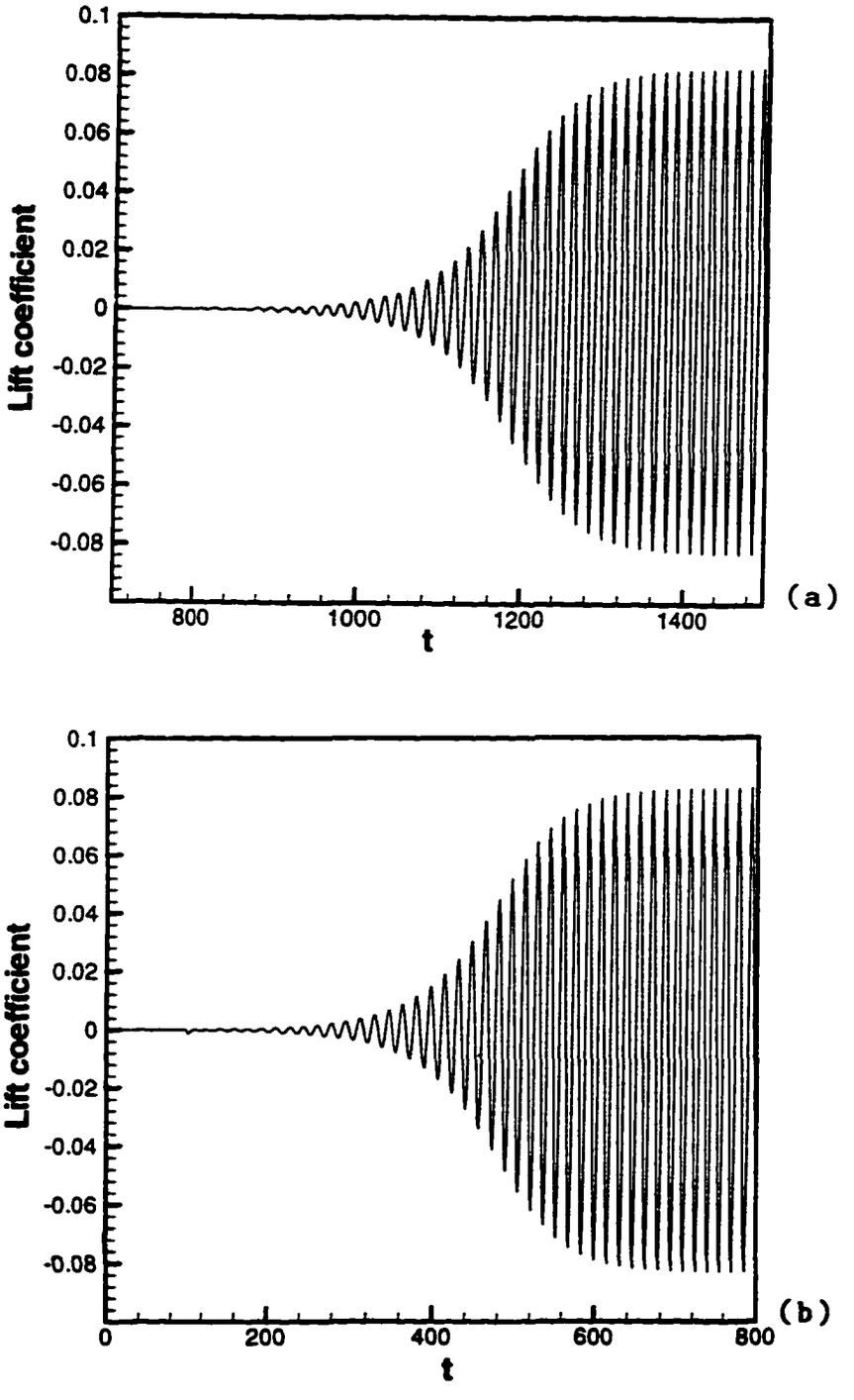

Figure 2.26: Lift coefficient for the cases without (a) and with (b) artificial perturbation at Reynolds number $Re = 56$.

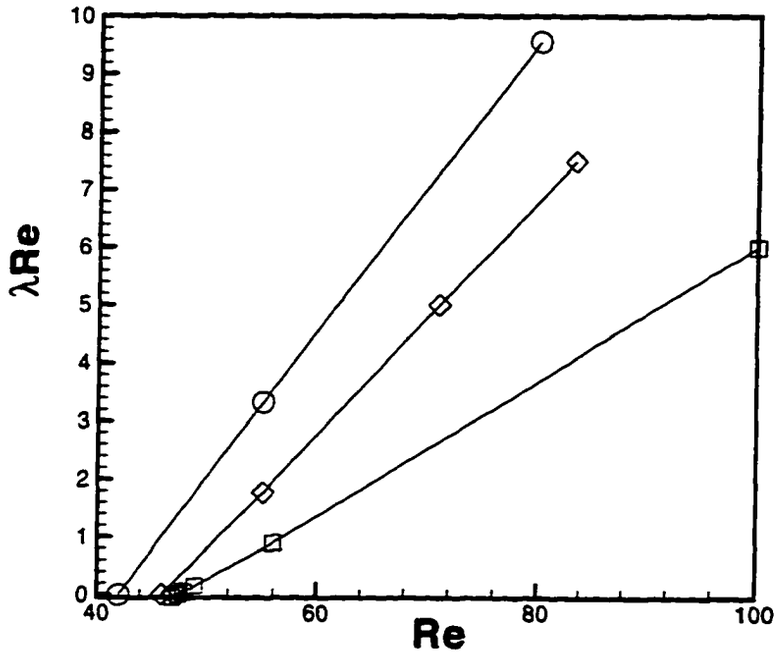

Figure 2.27: The growth rate versus Reynolds number. Numerical results (circles) and experimental results (diamonds) from Strykowski and Hannemann (1991), and present results (squares).

Chapter 3

Symmetry breaking instability leading to vortex shedding

3.1 Preliminaries

For Reynolds numbers higher than $Re = 47.5$, the symmetry breaking always occurs at some time after the impulsively started motion of the cylinder. This phenomenon is well-documented by the experimental works of Perry *et al.* (1982) and Coutanceau and Defaye (1991) and simulated by our computations (Chapter 2). The fact that the twin vortices are always present before vortex shedding develops seems to remain valid at all Reynolds numbers. This observation led us to study the dynamical properties of Föppl's (1913) vortex model and investigate its relevance to our computed flow. Föppl's formulation treats a special form of asymmetric perturbations. Here, we carry out a more general analysis, valid for any kind of perturbation. The results of this chapter are reported in Tang and Aubry (1997a)

3.2 The instability of Föppl's vortex model

3.2.1 The fixed point of Föppl's vortex model

In order to study the instability of twin, symmetric vortices behind a cylinder, we model the flow via potential vortices as did Föppl in 1913. Without loss of generality, we assume that the velocity of the oncoming flow be $U_\infty = 1$ and that the radius of the cylinder be also equal to 1, i.e. $a = 1$. Γ denotes the positive strength of the lower vortex, denoted by $Vort_2$, while the strength of the upper vortex, or $Vort_1$, is opposite, equal to $-\Gamma$. The induced flow is thus invariant under reflection symmetry with respect to the centerline $y = 0$. The presence of the circular cylinder boundary is represented by a pair of symmetric vortices located inside the cylinder (as sketched in figure 3.1). The inner vortices are placed to satisfy the boundary condition on the surface of the body. The flow built by superposition of the various potentials and streamfunctions involved can be expressed in terms of its complex potential which takes the form

$$W(z) = z + \frac{1}{z} - \frac{\Gamma}{2\pi i} ln(z - z_1) + \frac{\Gamma}{2\pi i} ln(z - \frac{1}{\overline{z}_1}) - \frac{\Gamma}{2\pi i} ln(z - \frac{1}{\overline{z}_2}) + \frac{\Gamma}{2\pi i} ln(z - z_2) \quad (3.1)$$

at each point $z = x + iy$ in the complex plane. The variables $z_1 = x_1 + iy_1$, $z_2 = x_2 + iy_2$ denote the locations of the twin vortices behind the cylinder in the complex plane. The index 1 refers to the upper vortex while the index 2 refers to the lower one. We now concentrate on two vortices which are the symmetric images of one another by reflection through the centerline. We thus consider $x_1 = x_2$ and $y_1 = -y_2$, or, equivalently, $z_2 = \overline{z}_1$.

The dynamics of the symmetrically disposed vortices is given by the complex

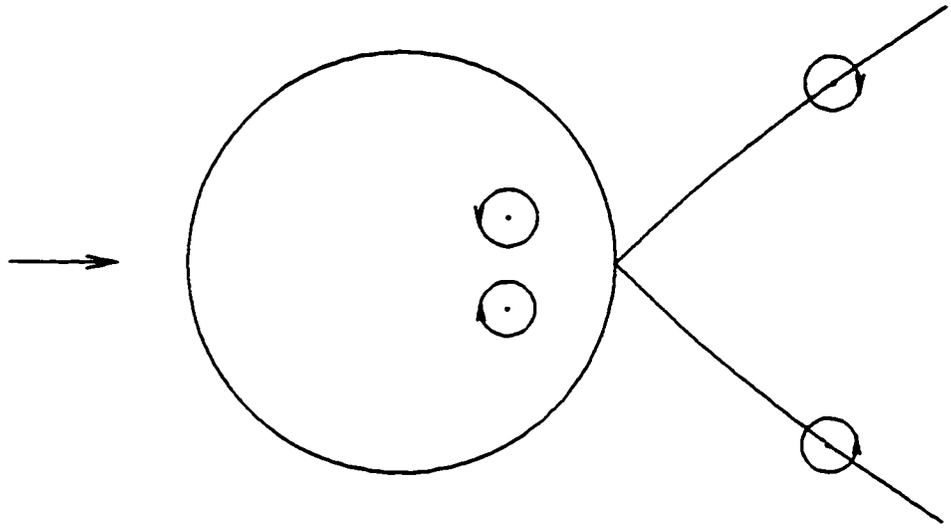

Figure 3.1: Sketch of the symmetric vortex pair and plot of the curve of fixed points in the model.

ordinary differential equation (ODE)

$$\frac{d\overline{z}_1}{dt} = 1 - \frac{1}{z_1^2} + \frac{\Gamma}{2\pi i}\frac{1}{z_1 - 1/\overline{z}_1} - \frac{\Gamma}{2\pi i}\frac{1}{z_1 - 1/z_1} + \frac{\Gamma}{2\pi i}\frac{1}{z_1 - \overline{z}_1}. \tag{3.2}$$

We then seek fixed points of this two-dimensional dynamical system, namely stationary pairs of symmetric vortices such that

$$\frac{d\overline{z}_1}{dt} = 0. \tag{3.3}$$

By solving these two (real) ordinary differential equations (see also Föppl, 1913; Smith, 1973; and Laat and Coene, 1995), we find that the fixed points are located on the two symmetric curves (see figure 3.1) in the (x, y)-plane defined by the equation

$$(r_1^2 - 1)^2 = 4r_1^2 y_1^2, \tag{3.4}$$

where $r_1^2 = x_1^2 + y_1^2$. The strength of the steady vortices is given by

$$\Gamma = 2\pi(r_1^2 - 1)^2(r_1^2 + 1)/r_1^5. \tag{3.5}$$

3.2.2 The stability analysis

We now investigate the stability property of the previous fixed points by slightly perturbing the latter. We then introduce the perturbed locations

$$z_1'' = x_1 + x_1' + i(y_1 + y_1'), \quad z_2'' = x_1 + x_2' + i(-y_1 + y_2') \tag{3.6}$$

where

$$z_1' = x_1' + iy_1', \quad z_2' = x_2' + iy_2' \tag{3.7}$$

are the small displacements from the equilibrium position in the complex plane. By substituting these expressions into the dynamical system (3.2), linearizing and using the fact that the vortices of strengths $-\Gamma$ and Γ are located at z_1 and $\overline{z}_1$, respectively,

we obtain the following four dimensional linear system of ODEs for the perturbations x_1', y_1', x_2' and y_2'

$$\frac{d}{dt}\begin{pmatrix} x_1' \\ y_1' \\ x_2' \\ y_2' \end{pmatrix} = \begin{pmatrix} a & b & c & d \\ e & -a & f & c \\ c & -d & a & -b \\ -f & c & -e & -a \end{pmatrix}\begin{pmatrix} x_1' \\ y_1' \\ x_2' \\ y_2' \end{pmatrix} \tag{3.8}$$

where the elements of the Jacobian matrix can be expressed in terms of the characteristics of the fixed point considered (defined by x_1, y_1 and Γ) as follows.

$$a(x_1) = \frac{2(x_1^3 - 3x_1y_1^2)}{r_1^6} + \frac{\Gamma x_1 y_1}{\pi(r_1^2-1)^2} - \frac{\Gamma x_1 y_1 (r_1^4 - 1)}{\pi[(x_1^2 - y_1^2 - 1)^2 + 4x_1^2y_1^2]^2} \tag{3.9}$$

$$b(x_1) = \frac{-2(y_1^3 - 3x_1^2y_1)}{r_1^6} - \frac{\Gamma(x_1^2 - y_1^2)}{2\pi(r_1^2-1)^2} + \frac{\Gamma}{2\pi(r_1^2-1)^2} + \frac{\Gamma[x_1^2(r_1^2-1)^2 - y_1^2(r_1^2+1)^2]}{2\pi[(x_1^2 - y_1^2 - 1)^2 + 4x_1^2y_1^2]^2} + \frac{\Gamma}{8\pi y_1^2} \tag{3.10}$$

$$c(x_1) = \frac{-2\Gamma x_1 y_1 (x_1^2 - y_1^2 - 1)}{\pi[(x_1^2 - y_1^2 - 1)^2 + 4x_1^2y_1^2]^2} \tag{3.11}$$

$$d(x_1) = \frac{-\Gamma[((x_1^2 - y_1^2 - 1)^2 - 4x_1^2y_1^2]}{2\pi[(x_1^2 - y_1^2 - 1)^2 + 4x_1^2y_1^2]^2} - \frac{\Gamma}{8\pi y_1^2} \tag{3.12}$$

$$e(x_1) = \frac{-2(y_1^3 - 3x_1^2y_1)}{r_1^6} - \frac{\Gamma(x_1^2 - y_1^2)}{2\pi(r_1^2-1)^2} - \frac{\Gamma}{2\pi(r_1^2-1)^2} + \frac{\Gamma[x_1^2(r_1^2-1)^2 - y_1^2(r_1^2+1)^2]}{2\pi[(x_1^2 - y_1^2 - 1)^2 + 4x_1^2y_1^2]^2} + \frac{\Gamma}{8\pi y_1^2} \tag{3.13}$$

$$f(x_1) = \frac{\Gamma[(x_1^2 - y_1^2 - 1)^2 - 4x_1^2y_1^2]}{2\pi[(x_1^2 - y_1^2 - 1)^2 + 4x_1^2y_1^2]^2} - \frac{\Gamma}{8\pi y_1^2} \tag{3.14}$$

where Γ is given by equation (3.5).

Note that a, b, c, d, e and f are functions of $r_1 = (x_1^2+y_1^2)^{1/2}$, such that x_1 and y_1 are related through the relation (3.4) satisfied by the equilibrium considered. We can thus consider $a(x_1)$ or $a(y_1)$. Here, we have arbitrarily chosen the x_1-dependency, that is $a(x_1)$, and similarly $b(x_1), c(x_1), d(x_1), e(x_1)$ and $f(x_1)$.

The substitution of the fixed point equations (3.4) and (3.5) leads to the

simplified expressions

$$a(x_1) = \frac{3x_1}{r_1^6} - \frac{2x_1}{r_1^8} \tag{3.15}$$

$$b(x_1) = \frac{1}{r_1^9} - \frac{5}{2r_1^7} + \frac{1}{2r_1^5} + \frac{2}{r_1^3} + \frac{1}{r_1} \tag{3.16}$$

$$c(x_1) = -\frac{x_1}{r_1^4} \tag{3.17}$$

$$d(x_1) = -\frac{1}{2r_1^5} - \frac{1}{2r_1^3} - \frac{1}{r_1} \tag{3.18}$$

$$e(x_1) = \frac{1}{r_1^9} - \frac{5}{2r_1^7} - \frac{3}{2r_1^5} + \frac{1}{r_1} \tag{3.19}$$

$$f(x_1) = \frac{1}{2r_1^5} - \frac{3}{2r_1^3} - \frac{1}{r_1}, \tag{3.20}$$

where, again, r_1 is the function of x_1 defined by equation (3.4). While the x_1-dependency of a, b, c, d, e, f should be kept in mind, it is often dropped below in order to lighten the notation.

The diagonalization of the Jacobian matrix leads to the following eigenvalues and eigenvectors

$$\lambda_{1,2}^2(x_1) = (a-c)^2 + (b+d)(e-f), \quad \vec{V}_{1,2}(x_1) = \begin{pmatrix} \frac{b+d}{\lambda_{1,2}-a+c} \\ 1 \\ \frac{-(b+d)}{\lambda_{1,2}-a+c} \\ 1 \end{pmatrix} \tag{3.21}$$

$$\lambda_{3,4}^2(x_1) = (a+c)^2 + (b-d)(e+f), \quad \vec{V}_{3,4}^R(x_1) + i\vec{V}_{3,4}^I(x_1) = \begin{pmatrix} \frac{d-b}{\lambda_{3,4}-a-c} \\ -1 \\ \frac{d-b}{\lambda_{3,4}-a-c} \\ 1 \end{pmatrix}, \tag{3.22}$$

which we rewrite

$$\lambda_1(x_1) = \sqrt{\frac{1}{r_1^{10}} - \frac{3}{r_1^8} + \frac{3}{r_1^6} + \frac{3}{r_1^4}} > 0, \quad \vec{V}_1(x_1) = \begin{pmatrix} \alpha(x_1) \\ 1 \\ -\alpha(x_1) \\ 1 \end{pmatrix} \tag{3.23}$$

$$\lambda_2(x_1) = -\sqrt{\frac{1}{r_1^{10}} - \frac{3}{r_1^8} + \frac{3}{r_1^6} + \frac{3}{r_1^4}} < 0, \quad \vec{V}_2(x_1) = \begin{pmatrix} -\beta(x_1) \\ 1 \\ \beta(x_1) \\ 1 \end{pmatrix} \tag{3.24}$$

$$\lambda_{3,4}^2(x_1) = \frac{5}{r_1^{10}} - \frac{13}{r_1^8} - \frac{5}{r_1^6} - \frac{3}{r_1^4} < 0. \tag{3.25}$$

We thus have a one-dimensional unstable subspace, a one-dimensional stable subspace and a two-dimensional center subspace. In real space, the symmetric vectors of any form

$$\vec{V}_3 = \begin{pmatrix} \gamma \\ 1 \\ \gamma \\ -1 \end{pmatrix} \quad and \quad \vec{V}_4 = \begin{pmatrix} -\delta \\ 1 \\ -\delta \\ -1 \end{pmatrix} \tag{3.26}$$

span the center subspace.

Here, $\alpha(x_1)$ and $\beta(x_1)$ are positive functions which can be easily deduced from equation (3.21) and (3.22), and γ and δ are arbitrary positive real numbers. It is interesting to display the functions $\alpha(x_1)$ and $\beta(x_1)$ defining the orientation of the unstable and stable eigenvectors $\vec{V}_1$ and $\vec{V}_2$ as the downstream distance x_1 varies (see figure 3.2(a)). While $\beta(x_1)$ remains small at all distances from the body, $\alpha(x_1)$ is large at small distances and decreases rapidly as x_1 increases. At large distances,

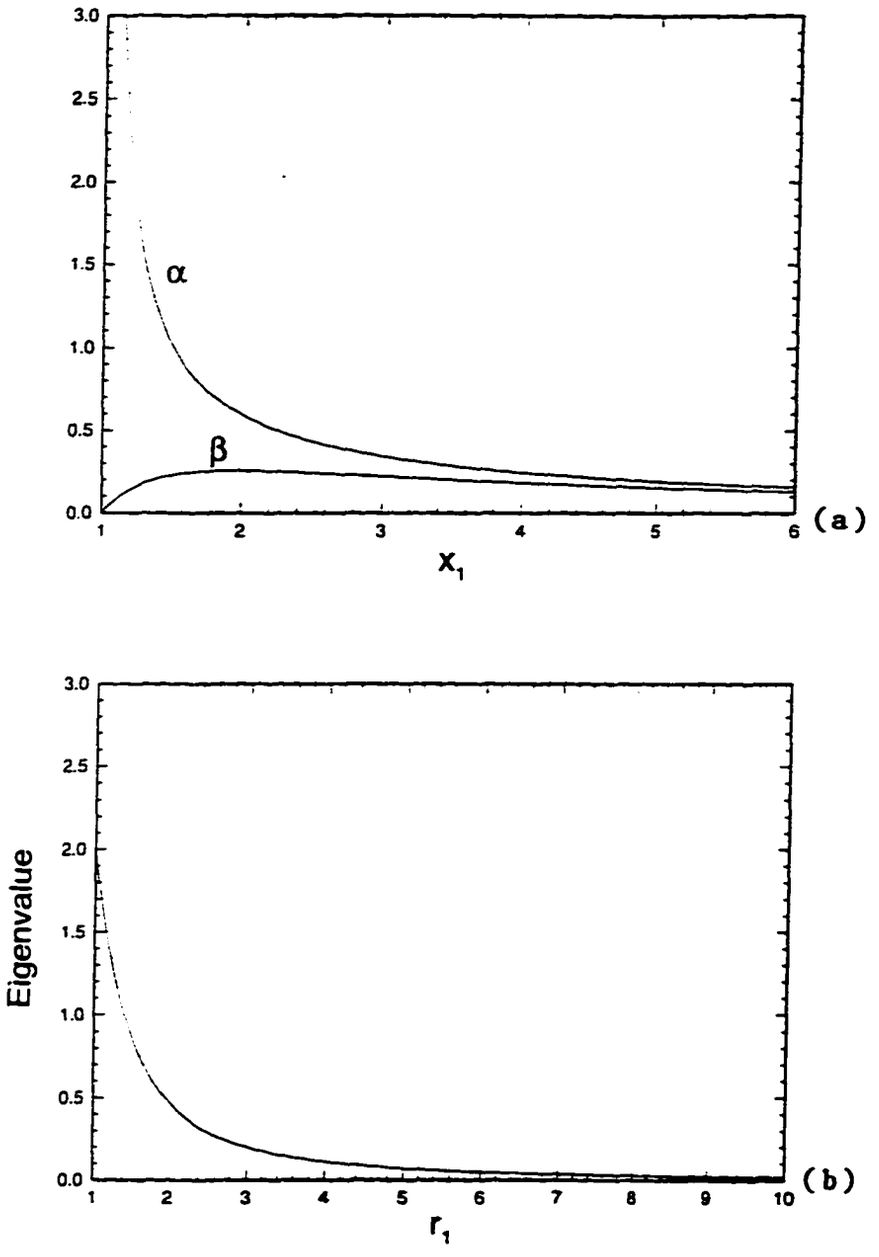

Figure 3.2: Low dimensional model representing twin point vortices and their stability property behind a circular cylinder: (a) the function $\alpha(x_1)$ involved in the unstable eigenvector $\vec{V}_1$ and the function $\beta(x_1)$ involved in the stable eigenvector $\vec{V}_2$; (b) The absolute value of the unstable and stable eigenvalues λ_1, λ_2 $(= -\lambda_1)$ as a function of the distance r_1 to the center of the cylinder.

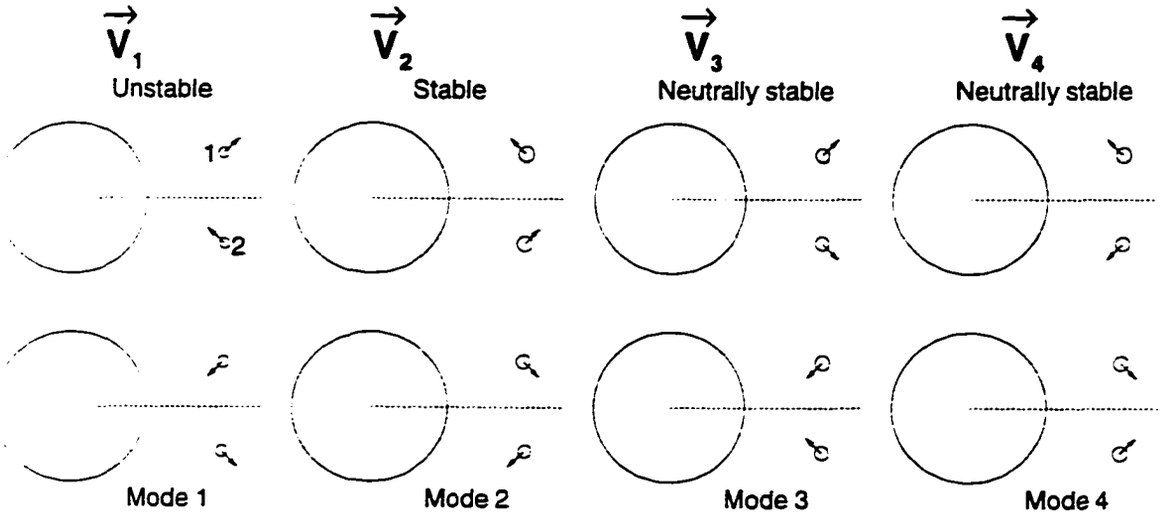

Figure 3.3: Configurations of the four vectors $\vec{V}_1$, $\vec{V}_2$, $\vec{V}_3$ and $\vec{V}_4$ (top) and their opposite companions $-\vec{V}_1$, $-\vec{V}_2$, $-\vec{V}_3$ and $-\vec{V}_4$ (bottom).

the two curves get close to each other, both decaying to zero at approximately the same rate. Figure 3.2(b) shows the absolute value of $\lambda_{1,2}$ for r_1 values up to $r_1 = 10$. The unstable eigenvalue has its maximal value on the surface of the body and decays monotonically for $r_1 > 1$. We summarize the directions of $\vec{V}_i, i = 1, 2, 3, 4$, in the (x, y) plane in figure 3.3 (top). Notice that if $\vec{V}_i$ is a solution, then $-\vec{V}_i$ (bottom) is also a solution. This leads to two possibilities for the orientation of the perturbations (x_1', y_1') and (x_2', y_2') corresponding to each vector.

Perhaps one of the most interesting features of the point vortex model is that the lower vortex $Vort_2$ in the unstable eigenmode $\vec{V}_1$ of figure 3.3 (top), has the tendency to move upstream and penetrate the flow between the upper vortex $Vort_1$ and the body while $Vort_1$ tends to move downstream and upward, being pushed away from $Vort_2$. Such vortex motion was described by Laat and Coene (1995) who computed the trajectories of the twin potential vortices in the model after perturbing them asymmetrically with respect to their equilibrium positions. Their results are gathered in their figure 9 where one can clearly see that the trajectories of the vortices fall exactly, in the early stage, on the unstable eigenspace defined by $\vec{V}_1$.

The fact that the unstable eigenspace is asymmetric is consistent with the stabilization of the flow by the insertion of a splitter plate on the centerline of the wake (Roshko, 1955). Indeed, this symmetrization imposes that $x_1' = x_2'$ and $y_1' = -y_2'$ which reduces the four dimensional dynamical system (3.8) to the two-dimensional system

$$\frac{d}{dt}\begin{pmatrix} x_1' \\ y_1' \end{pmatrix} = \begin{pmatrix} a+c & b-d \\ \\ e+f & -a-c \end{pmatrix}\begin{pmatrix} x_1' \\ y_1' \end{pmatrix}. \tag{3.27}$$

The diagonalization of the 2×2 Jacobian matrix gives us the third and fourth eigenvalues and the eigenvectors of the previous, four dimensional problem.

This mechanism therefore stabilizes the flow by reducing the dimension of the system and eliminating both the stable and unstable eigenspace (see a similar remark by Laat and Coene, 1995).

3.3 Numerical experiments

In this section we investigate the similarity between the low dimensional potential vortex model of Section 3.2 and our computed flows by introducing some particular perturbation in our direct numerical simulations (DNS). We recall that without the introduction of any additional perturbation in the DNS, the study of the stability property of the symmetric bubble flow at Reynolds numbers slightly above the critical Reynolds number requires long integration times during which numerical noise slowly amplifies. For instance, at Reynolds number $Re = 56$, the streamlines at times $t = 100$ and $t = 500$ obtained by DNS without any additional perturbation show a similar symmetric bubble structure (see figure 3.4(a) and 3.4(b)). In this time interval, the flow is quasi-steady, consisting of a symmetric recirculating bubble. We now show that the time it takes the instability to develop can be considerably shortened by introducing an adequate disturbance in the flow. The shape of the disturbance we use is inspired by our study of the low dimensional potential vortex model in Section 3.2.

First, we introduce a small artificial instantaneous vorticity perturbation such that

$$\Gamma_p = \omega_p dA = 0.003, \tag{3.28}$$

where ω_p is the value of the vorticity perturbation, and dA is the area of the grid mesh at the point considered (in this case, $\omega_p = 4.2$). Our insertion takes place at

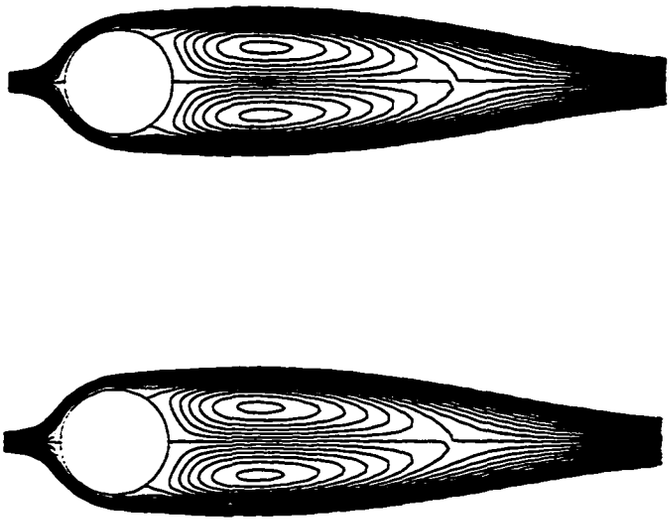

Figure 3.4: The flow at the Reynolds number $Re = 56$ at times: (a) $t = 100$ and (b) $t = 500$ showing that the flow consists of a symmetric recirculating bubble at both times without any artificial perturbation in the simulation.

time $t = 100$ and at the location $(1.1, 0.0)$ on the centerline. Immediately afterwards (i.e. for $t > 100$), we relax the perturbation. The velocity disturbance on the twin vortices induced by the previous perturbation is close to the stable eigenmode $\vec{V}_2$ of the vortex model of Section 3.2 as shown in figure 3.5(a). Hereafter, we call this kind of disturbance "an asymmetric convergent disturbance." If the viscous flow stability property is related to that of the model, the asymmetric convergent disturbance should decay in time according to equation (3.24).

Second, we use the same instantaneous vorticity perturbation, but we insert it in the flow at a point much farther downstream, for instance at the location $(10.1, 0.0)$, which is located on the centerline but outside the symmetric bubble as shown in figure 3.5(b). Here, the perturbation has the same circulation $\Gamma_p = \omega_p dA = 0.003$ as before, but the corresponding vorticity $\omega_p = 0.05$ is much smaller, due to the fact that the grid mesh increases considerably with the distance from the body. We refer to this kind of disturbance as "an asymmetric divergent disturbance." The disturbance is now close to the unstable eigenmode $\vec{V}_1$ and equation (3.23) of the vortex model predicts that such a disturbance should grow in time. As in the first simulation, we introduce the perturbation at $t = 100$ and release it immediately afterwards.

In both cases, we run our DNS code up to $t = 500$ and find that the stability property of the flow is similar to that of the model. We observe that the early oscillations of the lift offer a more precise criterion for the symmetry breaking instability than the time history of the drag or the flow patterns, which remain symmetric for some time after the lift starts oscillating. We thus look at the time history of the lift first. Figure 3.6(a) and 3.6(b) compare the lift in the two previous simulations with that obtained by the DNS without any perturbation. They clearly show that at $Re = 56$ the asymmetric divergent perturbation is amplified immediately after it is

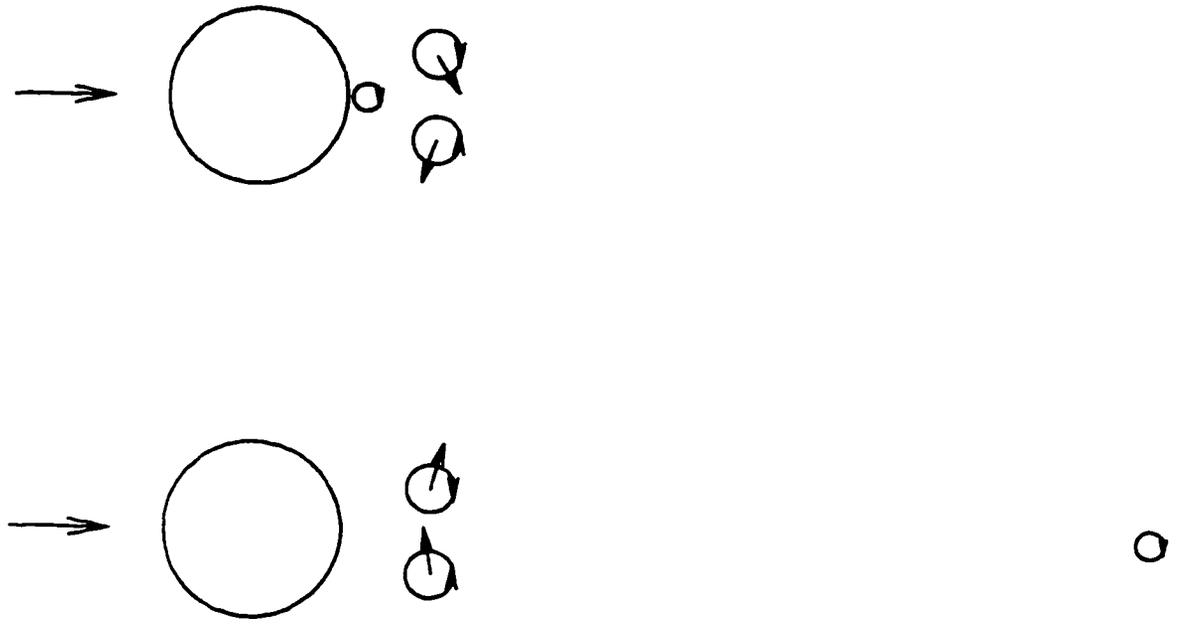

Figure 3.5: Sketch showing the small vorticity perturbation artificially introduced in the flow and the two main twin vortices of the bubble: (a) the perturbation is close to the cylinder so that the associated velocity disturbance applied to the twin vortices is of the asymmetric convergent type, i.e. along the stable eigenspace of the fixed point in the low dimensional model, (b) the perturbation is far away from the cylinder, so that the associated velocity disturbance applied to the twin vortices is of the asymmetric divergent type, i.e. along the unstable eigenvector of the fixed point in the low dimensional model.

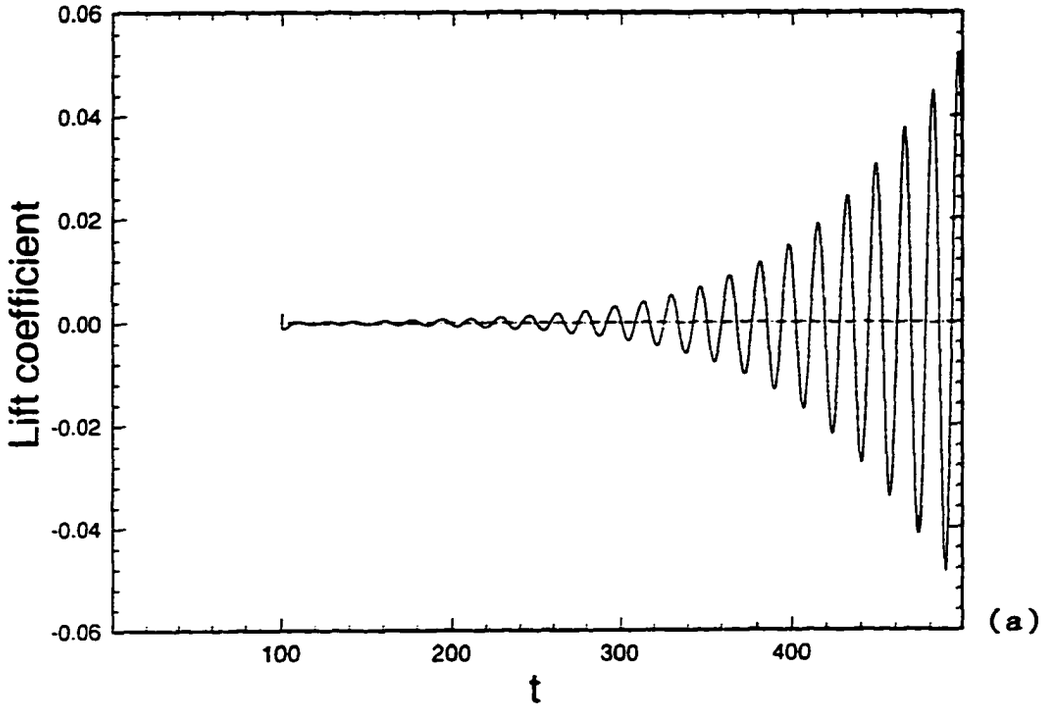

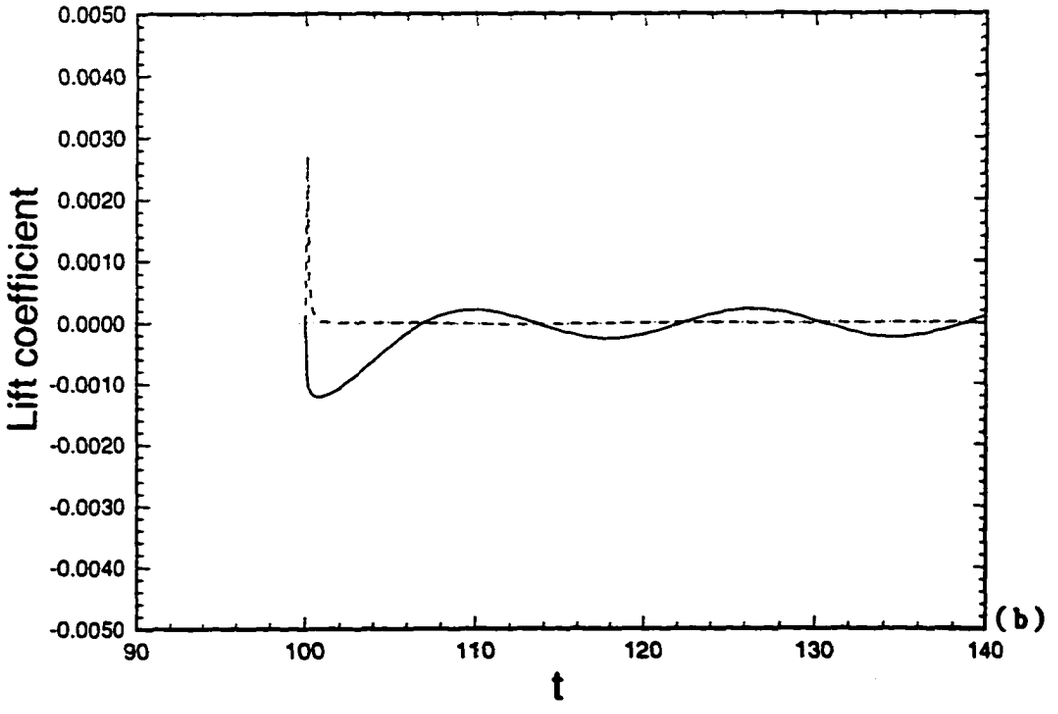

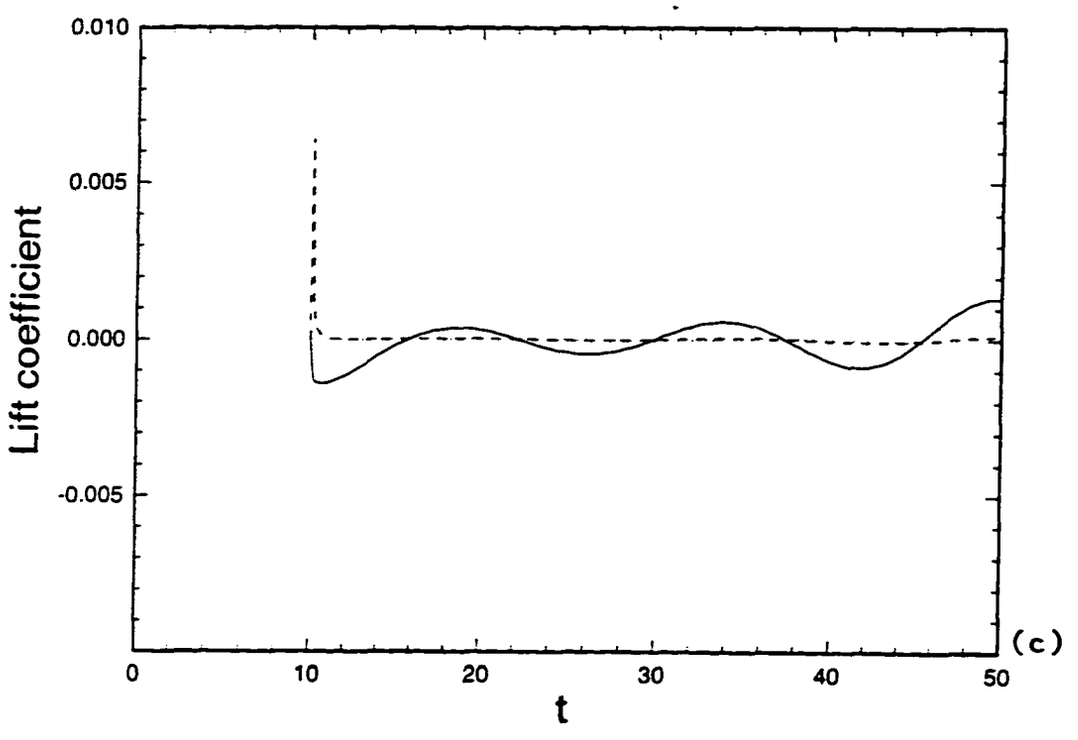

Figure 3.6: Time history of the lift coefficient in the direct numerical simulation (DNS): without any artificial perturbation (dotted line), with the vorticity perturbation ($\omega_p = 0.05, \Gamma_p = 0.003$) introduced at $x_1 = 10.1$ (solid line), with the vorticity perturbation ($\omega_p = 4.2, \Gamma_p = 0.003$) introduced at $x_1 = 1.1$ (dashed line), showing that the asymmetric divergent perturbation of figure 3.5(b) grows and that the asymmetric convergent perturbation of figure 3.5(a) decays: (a) at $Re = 56$, (b) zoom of (a), (c) at $Re = 100$.

introduced in the flow at $t = 100$ whereas the asymmetric convergent perturbation decays. It is interesting to point out that the lift is very similar in the original DNS (without perturbation) and in the DNS subjected to the asymmetric convergent perturbation after the latter has decayed. In both cases, the instability develops and the flow becomes asymmetric after some time under the action of round-off errors. Figure 3.6(c) shows that similar results are obtained at Reynolds number $Re = 100$. We now return to $Re = 56$ and insert an asymmetric convergent perturbation at $x_1 = 1.1$ of the same vorticity as the previous asymmetric divergent perturbation, that is $\omega_p = 0.05$. (The circulation of the new perturbation is $\Gamma_p = 3.73 \times 10^{-5}$.) Figure 3.7 shows that such a perturbation decays as well. We now display the flow patterns at $Re = 56$ at time $t = 500$ in figure 3.8 in the cases of the asymmetric divergent perturbation (figure 3.8(a)) and the two asymmetric convergent perturbations (figures 3.8(b) and 3.8(c)). Under the influence of the asymmetric divergent perturbation (figure 3.5(b)), the flow evolves into a vortex street at early times while the flow subjected to the asymmetric convergent perturbation (figure 3.5(a)) remains symmetric over a long time period.

It is interesting to emphasize that the perturbation is amplified when it is inserted in the far wake while it decays when it is located in the near wake. This result is somewhat intriguing due to the fact that the time averaged flow is absolutely unstable in the near wake and convectively unstable in the far wake.

In order to explore this point further, we reiterate our experiments at $Re = 56$ and insert the same vorticity perturbation (of circulation $\Gamma_p = 0.003$) on the centerline successively at the locations: (3,0), (4,0), (5,0), (6.1,0), (7.1,0) and (10.1,0) at time $t = 100$ and release it afterwards. Figure 3.9 displays the envelopes of the lift coefficients for all these runs. It is clear that the envelopes of the lift coefficients are exponential functions of time and that the growth rates are *identical* for all cases. The

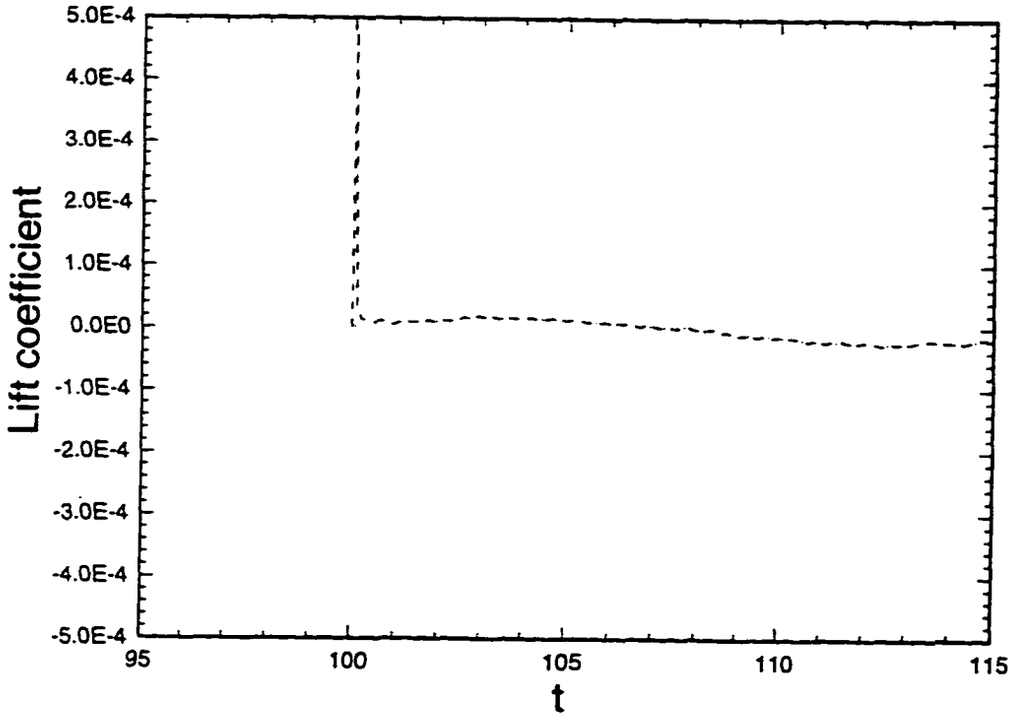

Figure 3.7: Time history of the lift coefficient in the direct numerical simulations (DNS) at $Re = 56$: without any artificial perturbation (dotted line), with the vorticity perturbation ($\omega_p = 0.05, \Gamma_p = 3.73 \times 10^{-5}$) introduced at $x_1 = 1.1$ (dashed line), confirming that the asymmetric convergent perturbation of figure 3.5(a) decays. Here, the perturbation has the same vorticity as the asymmetric divergent perturbation of figure 3.6.

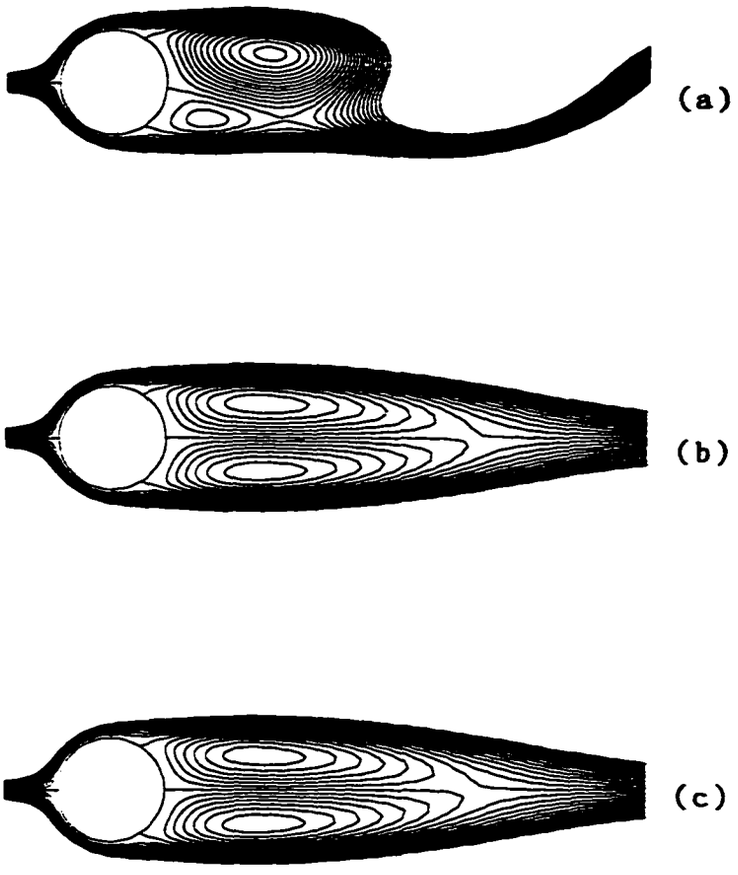

Figure 3.8: Streamlines of the flow from the direct numerical simulation (DNS) at $Re = 56$ at time $t = 500$ showing the stability property of the flow with: (a) the vorticity perturbation ($\omega_p = 0.05, \Gamma_p = 0.003$) at $x_1 = 10.1$, (b) the vorticity perturbation ($\omega_p = 4.2, \Gamma_p = 0.003$) at $x_1 = 1.1$ and (c) the vorticity perturbation ($\omega_p = 0.05, \Gamma_p = 3.73 \times 10^{-5}$) at $x_1 = 1.1$. In all cases, the perturbation is inserted in the flow at time $t = 100$. One observes that the flow consists of a Karman vortex street at time $t = 500$ in the simulation with the asymmetric divergent perturbation while the flow is still a bubble of counter-rotating vortices if asymmetric convergent perturbation is introduced.

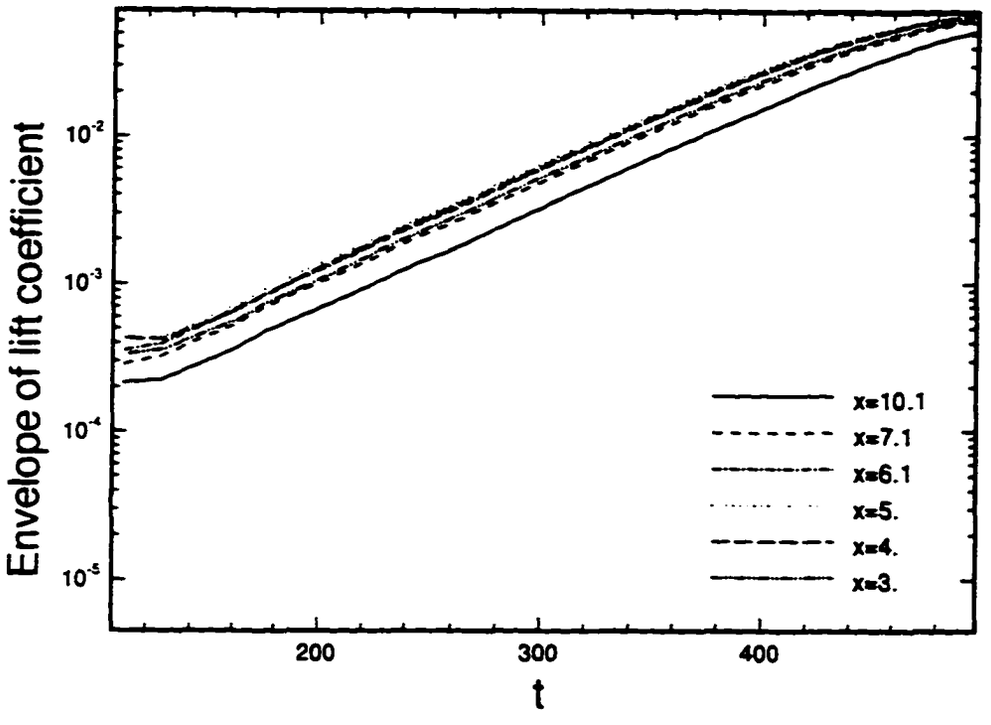

Figure 3.9: Envelopes of the lift coefficients obtained by direct numerical simulations in which the vorticity perturbation ($\Gamma_p = 0.003$) is introduced in the flow at time $t = 100$ at the distances $x_1 = 10.1$, $x_1 = 7.1$, $x_1 = 6.1$, $x_1 = 5.0$, $x_1 = 4.0$, and $x_1 = 3.0$ from the center of the body.

fact that the curves do not coincide is due to the fact that the various projections of the induced velocity disturbances on the twin vortices onto the stable, unstable and center subspaces of the model vary with the location of the perturbation on the centerline. For instance, the projection of the velocity disturbance induced by the perturbation located at $x_1 = 1.1$ onto the unstable eigenmode is close to zero. The disturbances related at all other locations ((3,0), (4,0), (5,0), (6.1, 0), (7.1,0) and (10.1,0)) have various (non-zero) projections onto both the stable eigenmodes and unstable one. But only the projections onto the unstable eigenmode amplify. Their growth thus takes place with the same growth rate, as confirmed by figure 3.9. The stability property of the flow is therefore independent of the location of the perturbation (provided the perturbation has a non-zero component along the unstable eigenmode).

To conclude this section, our numerical experiments show that the mechanism responsible for the instability of the symmetric bubble in the wake of a circular cylinder is qualitatively described by the instability of the potential vortex model. It is worth recalling, however, that the latter model does not provide a quantitative description of the real flow structure (Shair, 1963).

3.4 Concluding remarks and discussions

We have studied the stability of the symmetric recirculating bubble behind a circular cylinder analytically by means of the potential vortex model originally derived by Föppl and computationally by direct numerical simulations. The stability property of the flow in our numerical simulations is well represented qualitatively by the stability of the fixed point in the model. Above the critical Reynolds number, the symmetric bubble wake flow located behind a circular cylinder is found to be globally unstable in the sense that a perturbation, located at any distance from the body and

whose projection onto the unstable eigenmode of the model is non-zero, grows. This finding is useful for triggering the symmetry breaking instability of the recirculating bubble early. The unstable eigenmode $\vec{V}_1$ represented in figure 3.3 corresponds to motions of the twin vortices which can be described as follows. The lower vortex moves upstream and penetrates the flow between the upper vortex and the body while the upper vortex tends to move downstream and upward. This dynamics along $\vec{V}_1$ constitutes the origin of the shedding process of the upper vortex. It is interesting to point out that $\vec{V}_1$ and $-\vec{V}_1$ keep playing an important role in the Karman vortex street. Indeed, in the vortex shedding cycle itself, the previous motions can be easily detected as shown by our computations as well as by Perry *et al.*'s (1982) vortex shedding sketch (see figure 3.10). The roles of the upper vortex and the lower vortex have to be interchanged to describe $-\vec{V}_1$ which is the origin of the shedding process of the lower vortex. Vortex shedding thus consists of a motion alternating between $\vec{V}_1$ and $-\vec{V}_1$. Finally, the findings of this paper concerning the origin of the vortex shedding process will be used to control vortex shedding and its onset in the next chapter.

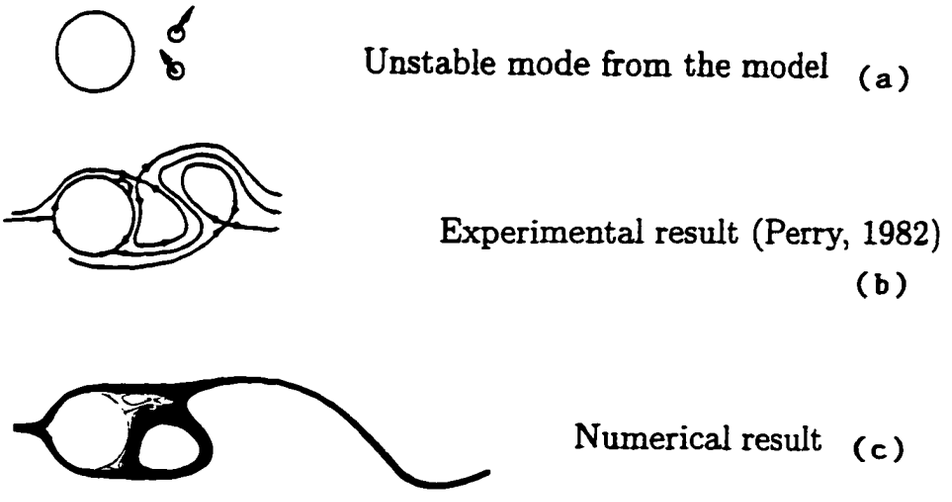

Figure 3.10: Similarity between: (a) the unstable eigenmode $\vec{V}_1$ of the low dimensional model, (b) the sketch plotted by Perry *et al.* (1982) and (c) the instantaneous streamlines obtained in this paper by direct numerical simulation at Reynolds number $Re = 100$ at time $t = 255$.

Chapter 4

Control of the cylinder wake

4.1 Preliminaries

In order to control the linear instability of the vortices in the model of Chapter 3, we recall that the unstable eigenspace is one-dimensional and that the corresponding (real) eigenvalue tends to zero rapidly as the distance of the vortices from the center of the cylinder increases (see figure 3.2(b)). This point leads us to wonder whether one can use a small effort to change the sign of the square of the eigenvalues $\lambda_{1,2}^2$ from positive to negative in order to eliminate the unstable eigenspace and therefore neutrally stabilize the symmetric bubble of vortices. The results of this chapter are reported in Tang and Aubry (1997b).

4.2 Control model for the symmetry breaking instability

4.2.1 Control model and its stability analysis

The control is investigated by designing a new dynamical system consisting of the previous vortex model to which we add a pair of symmetric control vortices that are maintained at the locations $z_c = x_c + iy_c$ and $\overline{z}_c$, respectively (see figure 4.1). Hereafter, Γ_c denotes the circulation of the upper control vortex, $-\Gamma_c$ being the circulation of the lower control vortex ($\Gamma_c > 0$). The original vortices located at z_1 and z_2, of circulation $-\Gamma$ and Γ ($\Gamma > 0$), respectively, are referred to as the *twin vortices* since they represent the recirculating bubble in the real flow. Under the assumption that the velocity of the oncoming flow is $U_\infty = 1$ and that the radius of the cylinder is also equal to 1, the new four dimensional dynamical system (whose variables are $z_1 = x_1 + iy_1$ and $z_2 = x_2 + iy_2$) is given by the equations:

$$\begin{aligned}\frac{d\overline{z}_1}{dt} &= 1 - \frac{1}{z_1^2} + \frac{\Gamma}{2\pi i}\frac{1}{z_1 - 1/\overline{z}_1} - \frac{\Gamma}{2\pi i}\frac{1}{z_1 - 1/\overline{z}_2} + \frac{\Gamma}{2\pi i}\frac{1}{z_1 - z_2} \\ &\quad + \frac{\Gamma_c}{2\pi i}\frac{1}{z_1 - z_c} - \frac{\Gamma_c}{2\pi i}\frac{1}{z_1 - \overline{z}_c} - \frac{\Gamma_c}{2\pi i}\frac{1}{z_1 - 1/\overline{z}_c} + \frac{\Gamma_c}{2\pi i}\frac{1}{z_1 - 1/z_c}. \end{aligned} \tag{4.1}$$

$$\begin{aligned}\frac{d\overline{z}_2}{dt} &= 1 - \frac{1}{z_2^2} - \frac{\Gamma}{2\pi i}\frac{1}{z_2 - 1/\overline{z}_2} + \frac{\Gamma}{2\pi i}\frac{1}{z_2 - 1/\overline{z}_1} - \frac{\Gamma}{2\pi i}\frac{1}{z_2 - z_1} \\ &\quad + \frac{\Gamma_c}{2\pi i}\frac{1}{z_2 - z_c} - \frac{\Gamma_c}{2\pi i}\frac{1}{z_2 - \overline{z}_c} - \frac{\Gamma_c}{2\pi i}\frac{1}{z_2 - 1/\overline{z}_c} + \frac{\Gamma_c}{2\pi i}\frac{1}{z_2 - 1/z_c}. \end{aligned} \tag{4.2}$$

Here z_2 should be replaced by $\overline{z}_1$ for symmetric solutions, particularly for symmetric fixed points. The second equation of motion is identical to the first one in which z_1 is replaced by z_2, Γ by $-\Gamma$ and vice versa.

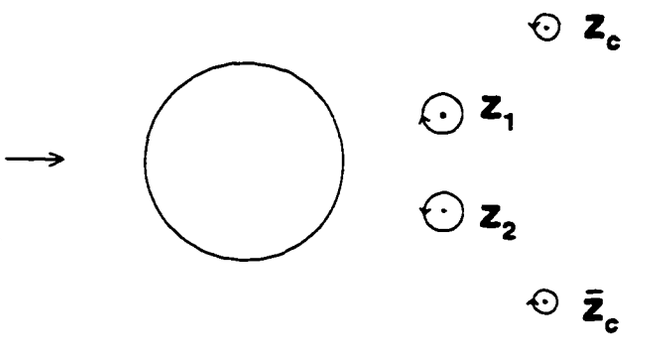

Figure 4.1: Sketch showing the twin vortices at positions z_1 and z_2 and the control vortices located at positions z_c and $\bar{z}_c$ in the control model.

The control system is more complex than the original model of Chapter 3 due to the fact that it has three extra independent parameters, which are the characteristics of the control vortices x_c, y_c and Γ_c. Since it is beyond the scope of this work to study the dynamics in this three-dimensional parameter space, we restrict our analysis to a few relevant cases.

We concentrate on finding the symmetric equilibria of the new model by solving the equations $d\bar{z}_1/dt = 0, z_2 = \bar{z}_1$, (where $d\bar{z}_1/dt$ is given by equation (4.1), the characteristics x_c, y_c and Γ_c of the control vortices and the circulation Γ of the twin vortices being considered as parameters. For this, we proceed as follows. Given x_c, y_c, Γ_c and Γ, we obtain the real part, u, and the imaginary part, v, as functions of x_1 and y_1, from the right hand side of equations (4.1) and (4.2). We then plot the zero streamwise and zero transverse velocity lines corresponding to $u = 0$ and $v = 0$, respectively. The equilibria we are seeking are located at the intersection points between the two curves. We observe that if Γ_c is too small, there is only one equilibrium similar to that of the original vortex model, and its stability properties are the same as those described in Chapter 3. If Γ_c is increased, but still small compared with Γ, the control vortex model generates three equilibria. Figure 4.2(a) shows the three curves of equilibria corresponding to the set of parameters $(x_c, y_c) = (4.294, 2.031)$, $\Gamma_c/2\pi = 0.03$ and different values of $\Gamma/2\pi$ ($\Gamma/2\pi = 1.6, 2, 3, 4, 5$). The curves represented by triangles, circles, diamonds are referred to as Curve 1, Curve 2, Curve 3, respectively. The squares correspond to the equilibria of the original model. Curve 1 is analogous to the curve of fixed points obtained in the original point vortex model of Section 2. The other two points are new equilibria strictly due to the presence of the control vortices. Figure 4.2(b) shows similar results for the set of parameters $(x_c, y_c) = (5.392, 1.35)$, $\Gamma_c/2\pi = 0.03$ and different values of $\Gamma/2\pi$ ($\Gamma/2\pi = 1, 2, 3, 4, 5$).

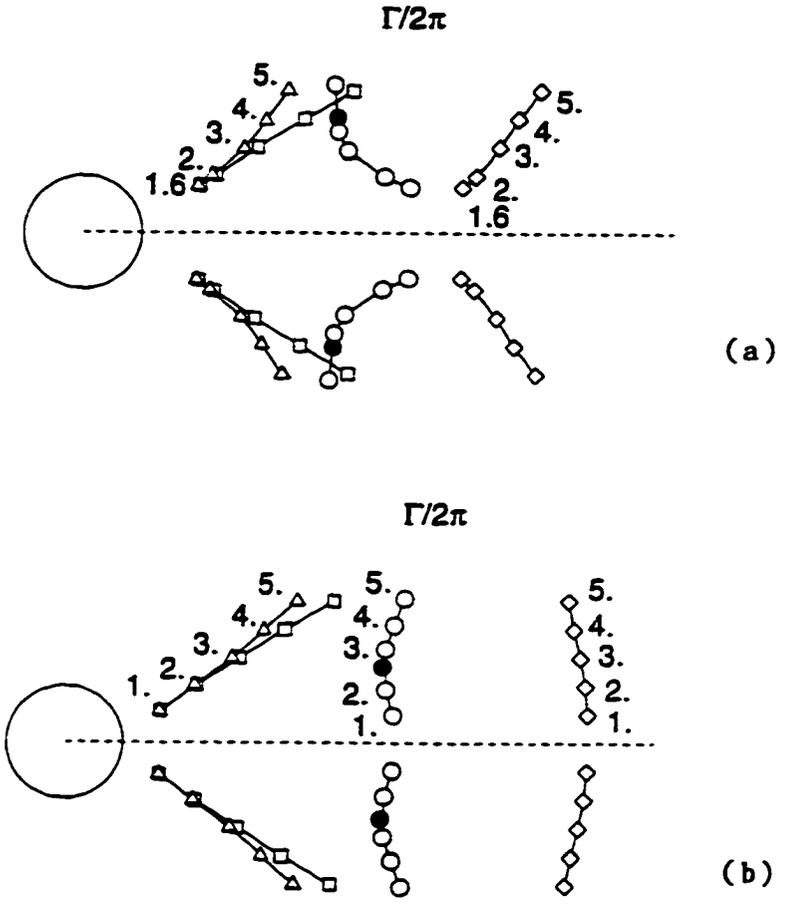

Figure 4.2: Location of the equilibrium positions for the control model whose control vortices have a circulation equal to $\Gamma_c/2\pi = 0.03$: (a) the control vortices are located at $x_c = 4.294, y_c = \pm 2.031$, (b) the control vortices are located at $x_c = 5.392, y_0 = \pm 1.35$. Equilibrium curve of the (uncontrolled) original model (squares), equilibrium curve 1 (triangles), equilibrium curve 2 (circles), equilibrium curve 3 (diamonds). We have indicated the values of the circulation $\Gamma/2\pi$ of the twin vortices corresponding to each equilibrium.

We now carry out the linear stability analysis of the fixed points, in a manner similar to that described in Chapter 3, and derive the equations of motion governing the dynamics of the perturbations around each equilibrium. Hereafter, x_1, y_1 denote the coordinates of the fixed point considered. The linear dynamics of the perturbation is governed by the set of ordinary differential equations (ODE)

$$\frac{d}{dt}\begin{pmatrix} x_1' \\ y_1' \\ x_2' \\ y_2' \end{pmatrix} = \begin{pmatrix} A & B & c & d \\ E & -A & f & c \\ c & -d & A & -B \\ -f & c & -E & -A \end{pmatrix} \begin{pmatrix} x_1' \\ y_1' \\ x_2' \\ y_2' \end{pmatrix} \tag{4.3}$$

where

$$A(x_1) = a(x_1) + P_r(x_1), \tag{4.4}$$

$$B(x_1) = b(x_1) - P_i(x_1), \tag{4.5}$$

$$E(x_1) = e(x_1) - P_i(x_1), \tag{4.6}$$

with

$$\begin{aligned} P_r(x_1) + iP_i(x_1) &= -\frac{\Gamma_c}{2\pi i}\frac{1}{(z_1 - z_c)^2} + \frac{\Gamma_c}{2\pi i}\frac{1}{(z_1 - \overline{z}_c)^2} \\ &\quad + \frac{\Gamma_c}{2\pi i}\frac{1}{(z_1 - 1/\overline{z}_c)^2} - \frac{\Gamma_c}{2\pi i}\frac{1}{(z_1 - 1/z_c)^2}, \end{aligned} \tag{4.7}$$

$$\begin{aligned} a(x_1) &= \frac{2(x_1^3 - 3x_1y_1^2)}{r_1^6} + \frac{\Gamma x_1 y_1}{\pi(r_1^2 - 1)^2} \\ &\quad - \frac{\Gamma x_1 y_1 (r_1^4 - 1)}{\pi[(x_1^2 - y_1^2 - 1)^2 + 4x_1^2y_1^2]^2}, \end{aligned} \tag{4.8}$$

$$\begin{aligned} b(x_1) &= \frac{-2(y_1^3 - 3x_1^2y_1)}{r_1^6} - \frac{\Gamma(x_1^2 - y_1^2)}{2\pi(r_1^2 - 1)^2} + \frac{\Gamma}{2\pi(r_1^2 - 1)^2} \\ &\quad + \frac{\Gamma[x_1^2(r_1^2 - 1)^2 - y_1^2(r_1^2 + 1)^2]}{2\pi[(x_1^2 - y_1^2 - 1)^2 + 4x_1^2y_1^2]^2} + \frac{\Gamma}{8\pi y_1^2}, \end{aligned} \tag{4.9}$$

$$c(x_1) = \frac{-2\Gamma x_1 y_1 (x_1^2 - y_1^2 - 1)}{\pi[(x_1^2 - y_1^2 - 1)^2 + 4x_1^2y_1^2]^2}, \tag{4.10}$$

$$d(x_1) = \frac{-\Gamma[((x_1^2 - y_1^2 - 1)^2 - 4x_1^2y_1^2]}{2\pi[(x_1^2 - y_1^2 - 1)^2 + 4x_1^2y_1^2]^2} - \frac{\Gamma}{8\pi y_1^2}; \tag{4.11}$$

$$e(x_1) = \frac{-2(y_1^3 - 3x_1^2 y_1)}{r_1^6} - \frac{\Gamma(x_1^2 - y_1^2)}{2\pi(r_1^2 - 1)^2} - \frac{\Gamma}{2\pi(r_1^2 - 1)^2} + \frac{\Gamma[x_1^2(r_1^2 - 1)^2 - y_1^2(r_1^2 + 1)^2]}{2\pi[(x_1^2 - y_1^2 - 1)^2 + 4x_1^2 y_1^2]^2} + \frac{\Gamma}{8\pi y_1^2}, \quad (4.12)$$

$$f(x_1) = \frac{\Gamma[(x_1^2 - y_1^2 - 1)^2 - 4x_1^2 y_1^2]}{2\pi[(x_1^2 - y_1^2 - 1)^2 + 4x_1^2 y_1^2]^2} - \frac{\Gamma}{8\pi y_1^2}. \quad (4.13)$$

Note that A, B, c, d, E, f are functions of $r_1 = (x_1^2 + y_1^2)^{1/2}$ such that x_1 and y_1 are related (since they are the coordinates of an equilibrium). We then retain the x_1-dependency only, i.e. $A(x_1), B(x_1), c(x_1), d(x_1), E(x_1), f(x_1)$. While such dependency should be kept in mind, it is often dropped to lighten the notation. Here, a, b, c, d, e and f are related to the twin vortices as they are in the original vortex model of Chapter 3, while the existence of the extra terms P_r and P_i is strictly due to the control vortices. The Jacobian matrix of equation (4.3) reduces to the Jacobian matrix of the original model if P_r and P_i are set to zero.

We now diagonalize the Jacobian matrix and obtain the following eigenvalues and eigenvectors

$$(\lambda_{1,2}^c)^2 = (A - c)^2 + (B + d)(E - f), \quad \vec{V}_{1,2}^c = \begin{pmatrix} \frac{B+d}{\lambda_{1,2} - A + c} \\ 1 \\ \frac{-(B+d)}{\lambda_{1,2} - A + c} \\ 1 \end{pmatrix} \quad (4.14)$$

$$(\lambda_{3,4}^c)^2 = (A + c)^2 + (B - d)(E + f), \quad \vec{V}_{3,4}^c = \begin{pmatrix} \frac{d-B}{\lambda_{3,4} - A - c} \\ -1 \\ \frac{d-B}{\lambda_{3,4} - A - c} \\ 1 \end{pmatrix}. \quad (4.15)$$

We can rewrite the eigenvalues as

$$(\lambda_{1,2}^c)^2 = (a - c)^2 + (b + d)(e - f) + P_r^2 + P_i^2 + 2(a - c)P_r - P_i(b + d + e - f) \quad (4.16)$$

$$(\lambda^c_{3,4})^2 = (a+c)^2 + (b-d)(e+f) + P_r^2 + P_i^2 + 2(a+c)P_r - P_i(b-d+e+f). \quad (4.17)$$

As expected, the eigenvalues (4.16), (4.17) coincide with the eigenvalues of the original model if P_r and P_i are set to zero. The extra terms due to the presence of the control vortices involve both P_r and P_i which are proportional to the circulation Γ_c of the control vortices. Our aim is now to make $(\lambda^c_{1,2})^2$ negative in order to eliminate the one-dimensional unstable eigenspace of the original model (while keeping $(\lambda^c_{3,4})^2$ negative). One can see that this goal may be reached if the circulation Γ_c of the control vortices is not too small.

The stability analysis of the three previous equilibria corresponding to the set of parameters $(x_c, y_c) = (2.908, 1.375)$, $\Gamma_c/2\pi = 0.048$ and $\Gamma/2\pi = 1.6$ is summarized below.

Equilibrium 1:

$$\lambda^c_1 = 0.4504, \quad \vec{V}^c_1 = \begin{pmatrix} 0.6559 \\ 1 \\ -0.6559 \\ 1 \end{pmatrix}, \quad \textit{unstable subspace}, \quad (4.18)$$

$$\lambda^c_2 = -0.4504, \quad \vec{V}^c_2 = \begin{pmatrix} -0.2174 \\ 1 \\ 0.2174 \\ 1 \end{pmatrix}, \quad \textit{stable subspace}, \quad (4.19)$$

$$(\lambda^c_{3,4})^2 = -0.4056, \quad \textit{center subspace}. \quad (4.20)$$

Equilibrium 2:

$$\lambda_1^c = 0.3422, \quad \vec{V}_1^c = \begin{pmatrix} 0.2168 \\ 1 \\ -0.2168 \\ 1 \end{pmatrix}, \quad \textit{unstable subspace}, \tag{4.21}$$

$$\lambda_2^c = -0.3422, \quad \vec{V}_2^c = \begin{pmatrix} -0.2849 \\ 1 \\ 0.2849 \\ 1 \end{pmatrix}, \quad \textit{stable subspace}, \tag{4.22}$$

$$\lambda_3^c = 0.3183, \quad \vec{V}_3^c = \begin{pmatrix} -3.6037 \\ -1 \\ -3.6037 \\ 1 \end{pmatrix}, \quad \textit{unstable subspace}, \tag{4.23}$$

$$\lambda_4^c = -0.3183, \quad \vec{V}_4^c = \begin{pmatrix} 5.7692 \\ -1 \\ 5.7692 \\ 1 \end{pmatrix}, \quad \textit{stable subspace}, \tag{4.24}$$

Equilibrium 3:

$$(\lambda_{1,2}^c)^2 = -0.003473, \quad \textit{center subspace}, \tag{4.25}$$

$$(\lambda_{3,4}^c)^2 = -0.00527, \quad \textit{center subspace}. \tag{4.26}$$

In conclusion, the stability characteristic of Equilibrium 1 is similar to the stability of the unique equilibrium of the original model (Chapter 3): both fixed points have one positive eigenvalue, one negative eigenvalue and two conjugate imaginary eigenvalues. The unstable subspace consists of the asymmetric divergent mode,

while the asymmetric convergent mode characterizes the stable subspace. The center subspace is spanned by two symmetric modes. Equilibrium 2 has two unstable eigenspaces, spanned by the asymmetric divergent mode and the symmetric divergent mode, and two stable eigenspaces spanned by the asymmetric convergent and symmetric convergent modes. Finally, all the eigenvalues of Equilibrium 3 are imaginary. Here, both the stable and unstable subspaces disappear and the center subspace is four dimensional. The existence of the third equilibrium shows that a small control vortex couple can (neutrally) stabilize a symmetric bubble.

The stability analysis has been performed with all the parameter values, x_c, y_c, Γ_c and Γ given in Table 4.1. In *all* these cases, the stability properties of the control model are qualitatively the same as those previously described, that is the equilibria located on curves 1 and 2 are found to be unstable while the equilibria of curve 3 are neutrally stable. The existence of a neutrally stable equilibrium is robust in the sense that it is valid for a wide range of parameters in the model.

These stability features of the control model are confirmed by the following numerical integration of equations (4.1) and (4.2).

4.2.2 Integration of the control model

In order to illustrate the existence of the equilibria, their stability and the role they play in the solutions of the (non-linear) model, we integrate the ordinary differential equations (4.1) and (4.2), starting with various initial conditions. The numerical simulations are performed by means of a fourth-order Runge-Kutta integration method used with double precision. In the simulations, we have chosen the parameter values $(x_0, y_0) = (2.908, 1.375)$, $\Gamma_0/2\pi = 0.048$ and $\Gamma/2\pi = 1.6$ for the location, the circulation of the control vortices and the circulation of the twin vortices, respectively. Note that the linear stability analysis has also been performed for these

(x_0, y_0)	$\Gamma_0/2\pi$	$\Gamma/2\pi$
(2.908, 1.375)	0.048	1.6
(2.908, 1.375)	0.096	1.6
(4.908, 1.375)	0.048	1.6
(2.908, 1.375)	0.03	2
(2.908, 1.375)	0.05	2
(4.294, 2.031)	0.03	1.6
(4.294, 2.031)	0.03	2
(4.294, 2.031)	0.03	3
(4.294, 2.031)	0.03	4
(4.294, 2.031)	0.03	5
(5.392, 1.35)	0.03	1.
(5.392, 1.35)	0.03	2.
(5.392, 1.35)	0.03	3.
(5.392, 1.35)	0.03	4.
(5.392, 1.35)	0.03	5.

Table 4.1: Parameter values used for the integration of the control model.

parameter values (see Section 4.2.1 and Table 4.1).

Dynamics in the symmetric subspace

Figure 4.3(a) shows the trajectories obtained with initial conditions consisting of *symmetric* perturbations to the equilibria. One can clearly see, in this symmetric subspace, that Equilibria 1 and 3 are centers while Equilibrium 2 is a saddle point stable to symmetric convergent perturbations and unstable to symmetric divergent perturbations. These stability features coincide with our previous theoretical analysis. Starting with an initial condition close to Equilibrium 2 also shows the existence of a homoclinic cycle connecting the saddle to itself and wondering around the two centers. The remaining trajectories are limit cycles wondering around each center or around the homoclinic cycle. Figure 4.3(b) confirms this picture by providing a zoom of the top half of figure 4.3(a).

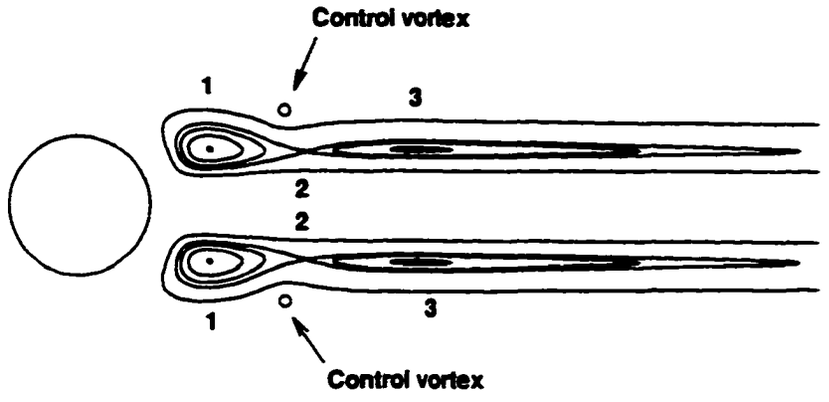

(a)

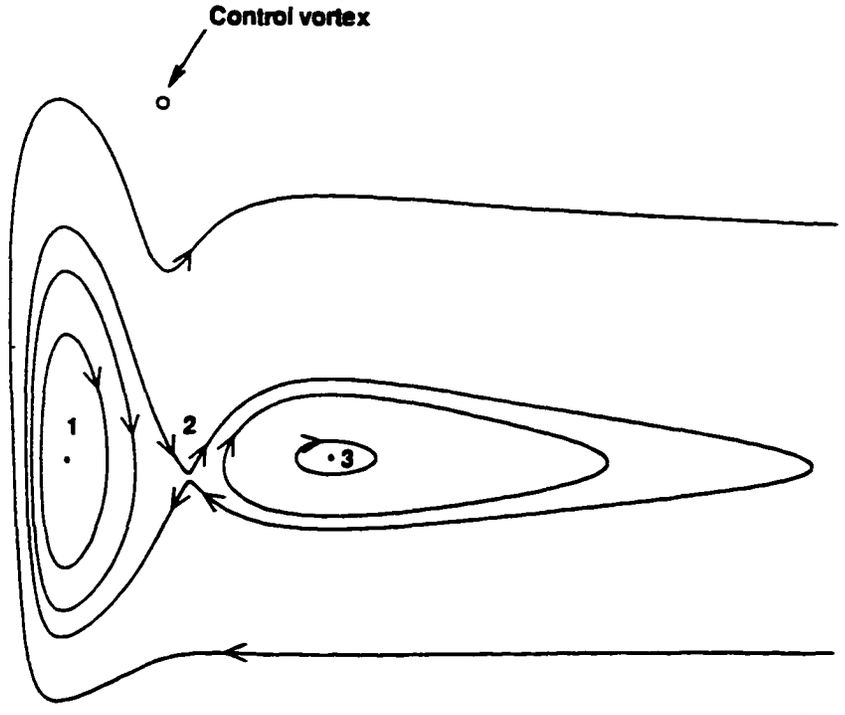

(b)

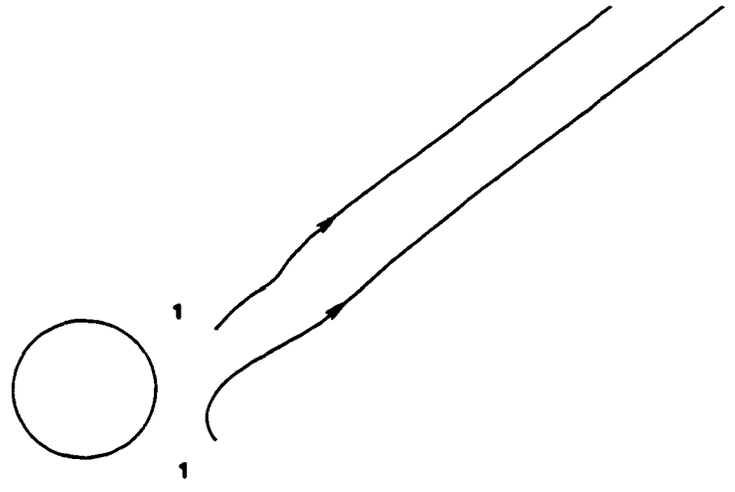

(c)

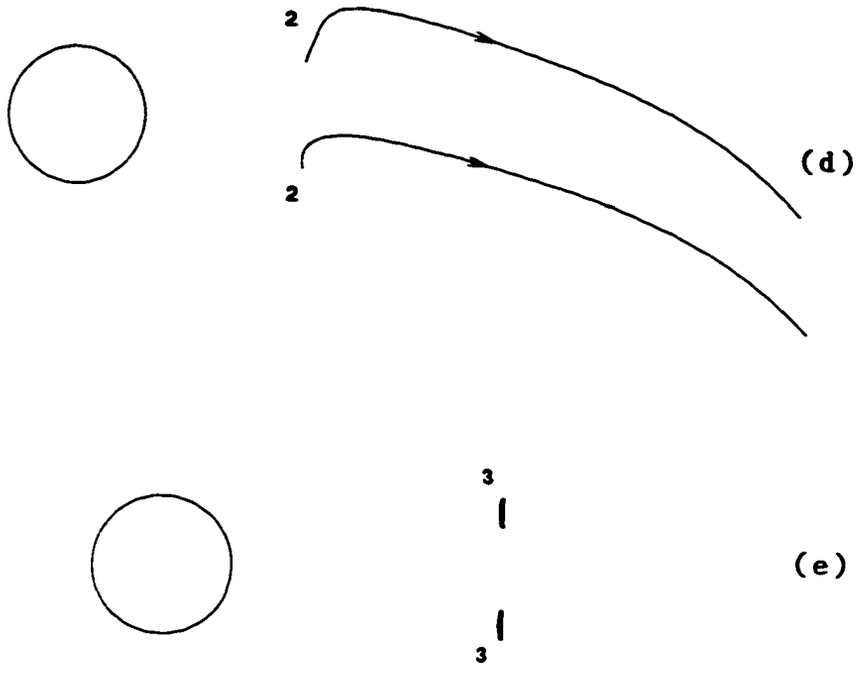

Figure 4.3: Representation of the cylinder and the trajectory of the point vortices solutions of the low dimensional control model (4.1) and (4.2) whose parameters are $x_c = 2.908, y_c = \pm 1.375$, $\Gamma_c/2\pi = 0.048$, $\Gamma/2\pi = 1.6$; 1, 2, 3 refer to the three equilibria of curves 1, 2, 3, respectively (see figure (4.2). (a) Trajectory of vortices obtained by perturbing the equilibria with *symmetric* perturbations. In this (symmetric) subspace, Equilibria 1 and 3 are centers while Equilibrium 2 is a saddle point. One can clearly observe the presence of a homoclinic orbit connecting the saddle to itself. (b) Details of the trajectories of (a). (c-e) Trajectory of vortices obtained by perturbing Equilibrium 1 (c), Equilibrium 2 (d) and Equilibrium 3 (e) with *asymmetric* perturbations showing the instability of Equilibria 1, 2 and the neutral stability of Equilibrium 3 outside the symmetric subspace.

Dynamics in the full space

Our linear stability analysis has shown that Equilibria 1 and 2 are unstable to some asymmetric perturbations and Equilibrium 3 is neutrally stable to *all* kinds of perturbations. This is corroborated by integrating the original non-linear equations and by computing the trajectory of the vortices. The latter which are given small *asymmetric* perturbations from the various individual equilibria are displayed in figures 4.3(c), 4.3(d) and 4.3(e). While it is clear that the asymmetric perturbations are amplified immediately for Equilibria 1 and 2 (see figures 4.3(c) and 4.3(d)), the trajectories of Equilibrium 3 remains in a bounded area as shown in fig. 7(e). In the latter case, detailed observation of the latter trajectories shows the asymmetry of the vortices at all times.

The numerical integration of the control model thus confirms the results of our linear stability analysis. One of the most interesting features of the control model is that it generates new equilibrium points, one of which being neutrally stable. Whether a pair of small control vortices can indeed suppress the instability and make a new symmetric bubble stable in the numerically simulated flow is the subject of the next section.

4.3 Numerical Simulations of controlled flows

The stability analysis of the control vortex model reported in the last section shows that we may be able to control the wake instability in the real flow by inserting a pair of small symmetric vortices in the flow. In order to pursue this task, we now carry out two-dimensional numerical simulations of wake flows in the presence of control vortices which play the role of a forcing in the Navier-Stokes equations.

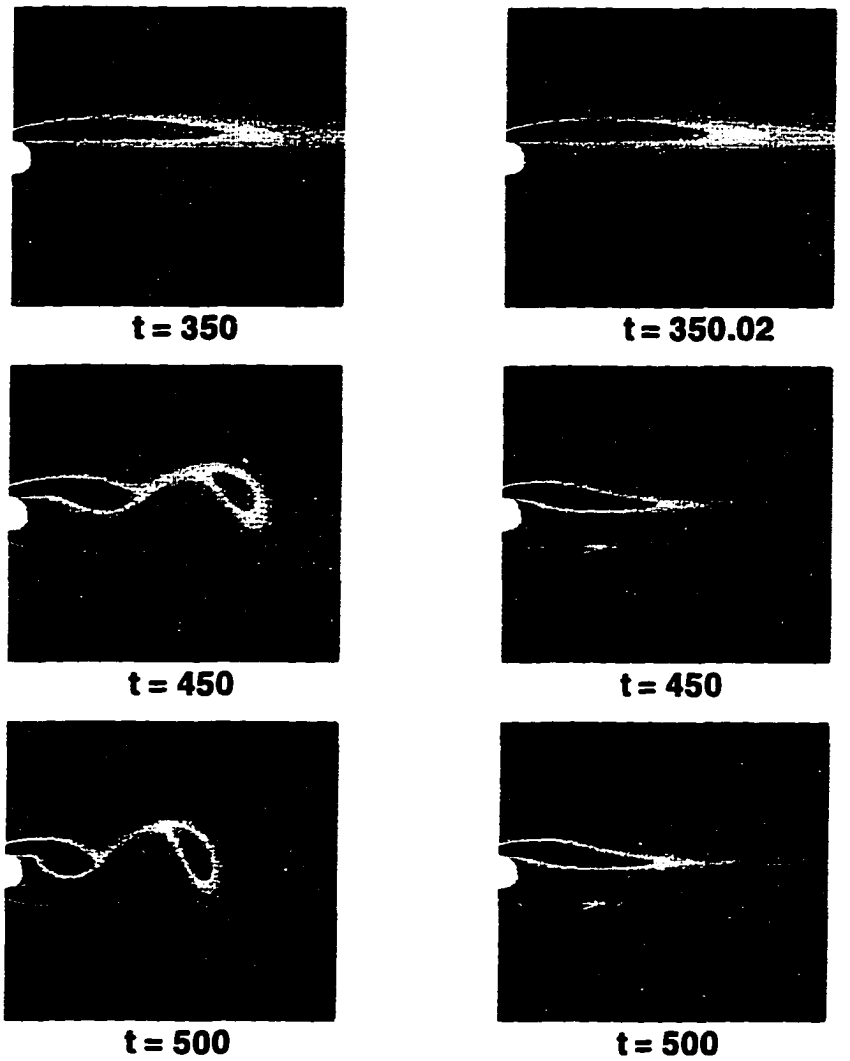

Figure 4.4: Control of the onset of vortex shedding by insertion of two small control vortices ($\omega_c = 0.2$) at the location $x_c = 4.294, y_c = \pm 2.031$ at $Re = 100$, at time $t = 350.01$. The flow is visualized by means of vorticity contours. Left column: flow without control showing the instability of the recirculating bubble, right column: flow with control showing that the asymptotic state is a symmetric bubble different from the natural bubble (such as that displayed at $t = 350$ in the uncontrolled case).

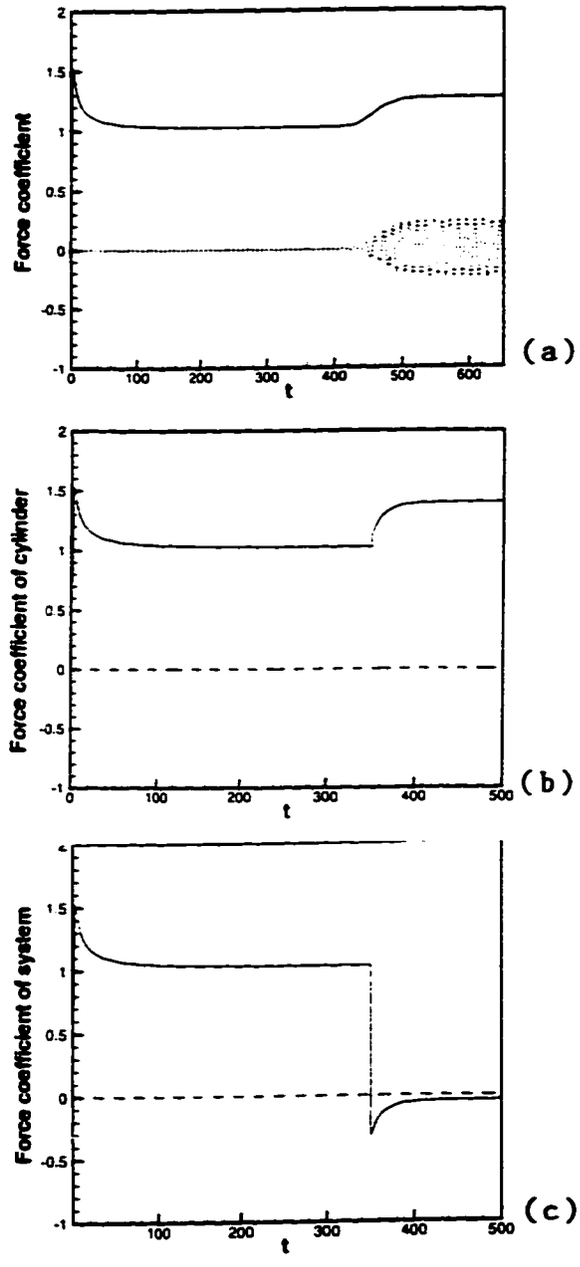

Figure 4.5: Time history of the force coefficients of the uncontrolled and controlled flows of figure 4.4: drag coefficient (solid line), lift coefficient (dashed line). (a) Force coefficients on the body in the uncontrolled flow, (b) force coefficients on the body in the controlled flow, (c) force coefficients on the full system (containing both the cylinder and the control vortices) in the controlled flow.

4.3.1 Control of the onset of vortex shedding at $Re = 100$

We first investigate whether it is possible to prevent vortex shedding from occurring in the transient flow. For this, we run our code at $Re = 100$. The transient flow consists of a growing symmetric recirculating bubble of counter-rotating vortices. Under natural conditions, this bubble undergoes a symmetry breaking instability and evolves toward a Karman vortex street. During the instability events, both the drag and the lift start oscillating, and the drag jumps abruptly to a higher value. In the present computation, the flow is still a recirculating bubble at time $t = 350$. Shortly after this (at time $t = 350.01$), we introduce two control vortices $\omega_c = \pm 0.2$ at the locations $x_c = 4.294, y_c = \pm 2.031$. Figure 4.4 displays both the natural evolution of the flow to vortex shedding (left column) and the evolution of the recirculating bubble to another bubble flow under the effect of the control vortices (right column). One clearly observes that the region of strong vorticity in the original bubble is concentrated near the body, while it is more elongated in the controlled flow (right column, compare $t = 350.02$ with $t = 500$). Figure 4.5 displays the drag and lift coefficients of the flow in both the uncontrolled case and in the controlled situation. In the uncontrolled flow (figure 4.5(a)), the drag and the lift start oscillating as the recirculating bubble undergoes the instability, and the drag jumps to a higher value. Here, Algorithm 1 (equation (2.12)) and Algorithm 2 (equation (2.13)) of Chapter 2 lead to the same results. In the case of the control, we can compute two types of forces: the forces acting on the body itself from Algorithm 1, and the forces acting on the full system including both the body and the control vortices from Algorithm 2. The selection of a specific control volume does not affect our drag and lift results provided that *cv* is located in a well resolved area of our computational domain. The forces acting on the body are displayed in figure 4.5(b). The first remark is that the force no longer oscillates under the effect of the control. Instead, both the lift and

the drag reach constant values after a short transient owing to the steadiness of the asymptotic controlled flow. While the lift remains zero throughout the computation (due to the fact that the flow never loses its reflection symmetry through the mid-plane), the drag increases to a constant value slightly higher than the mean drag value of the vortex shedding. Figure 4.5(c) presents the body force acting on the system. As in figure 4.5(b), the lift remains zero at all times. The drag, however, undergoes a dramatic drop due to the insertion of the control vortices in the flow. After the drop, the drag increases to reach its asymptotic, slightly negative value, showing that the full system experiences weak propulsion. The decrease of the drag acting on the full system can be understood from the relation between the body force and the vorticity distribution in the whole domain:

$$\begin{aligned} \vec{F_b} &= -\frac{d}{dt}\int\int_{fluid} \vec{u}dxdy \\ &= \frac{d}{dt}\int\int_{fluid} \vec{\omega}\times\vec{x}dxdy \\ &= \frac{d}{dt}\int\int_{fluid} (-\omega y\vec{i}+\omega x\vec{j})dxdy. \end{aligned} \tag{4.27}$$

Here, $\vec{i}$ denotes the direction of the oncoming flow. It is clear from (4.27) that the drag depends only on the time derivative of the integral of $-\omega y$ over the whole flow field. The introduction of new positive (or negative) vorticity at a positive (or negative) y-location decreases the drag. The insertion of the control vortices has no contribution to the lift due to the fact that the effects of the control vortices (of vorticity ω and $-\omega$) cancel each other since they are introduced at the same x-location. The insertion of new vorticity in the flow can thus play a major role in drag reduction strategies.

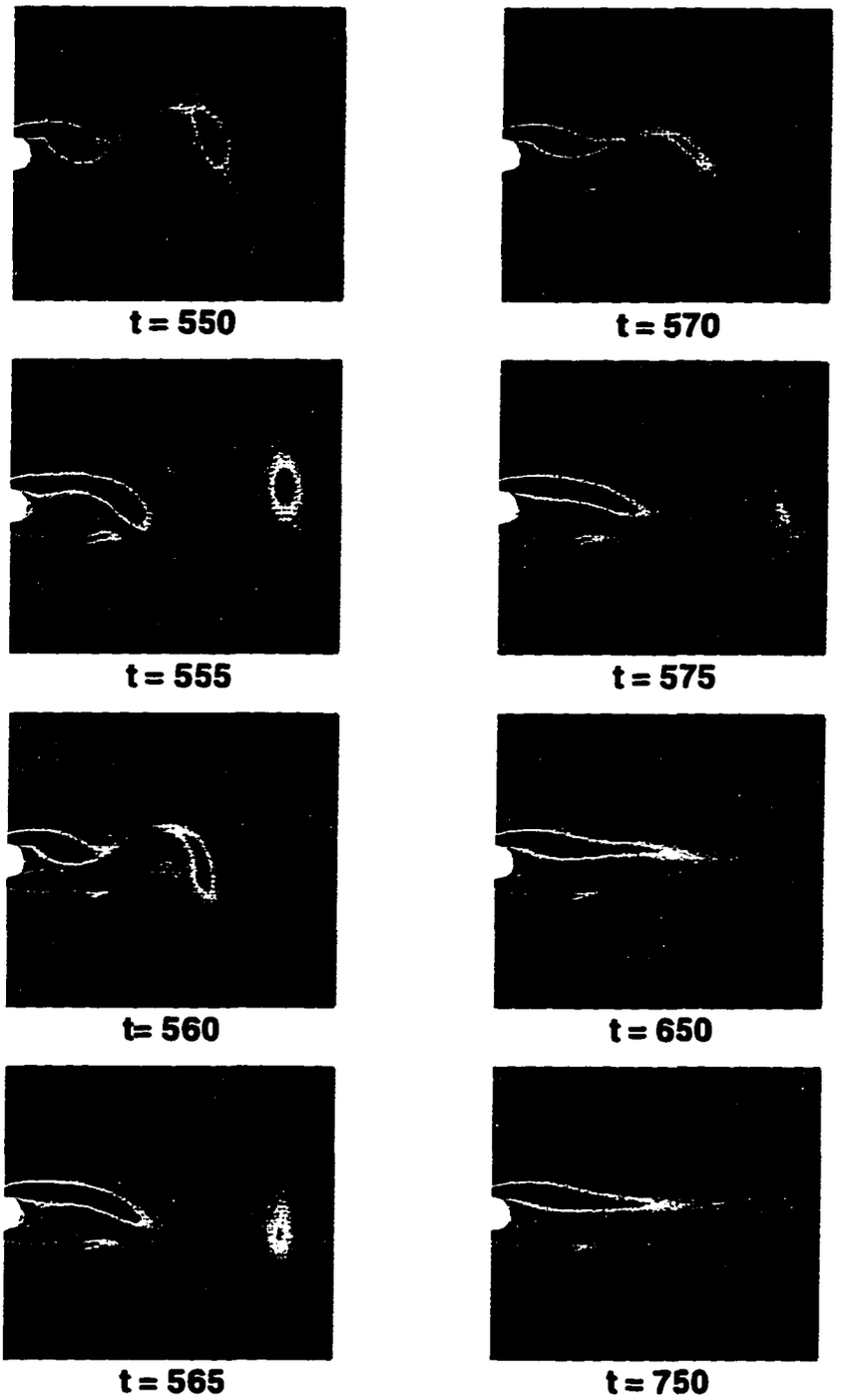

Figure 4.6: Vorticity contours showing the suppression of vortex shedding by insertion of the same small control vortices as in figure 4.4. At time $t = 550$, the flow is in its natural vortex shedding state. The control is inserted at time $t = 550.01$.

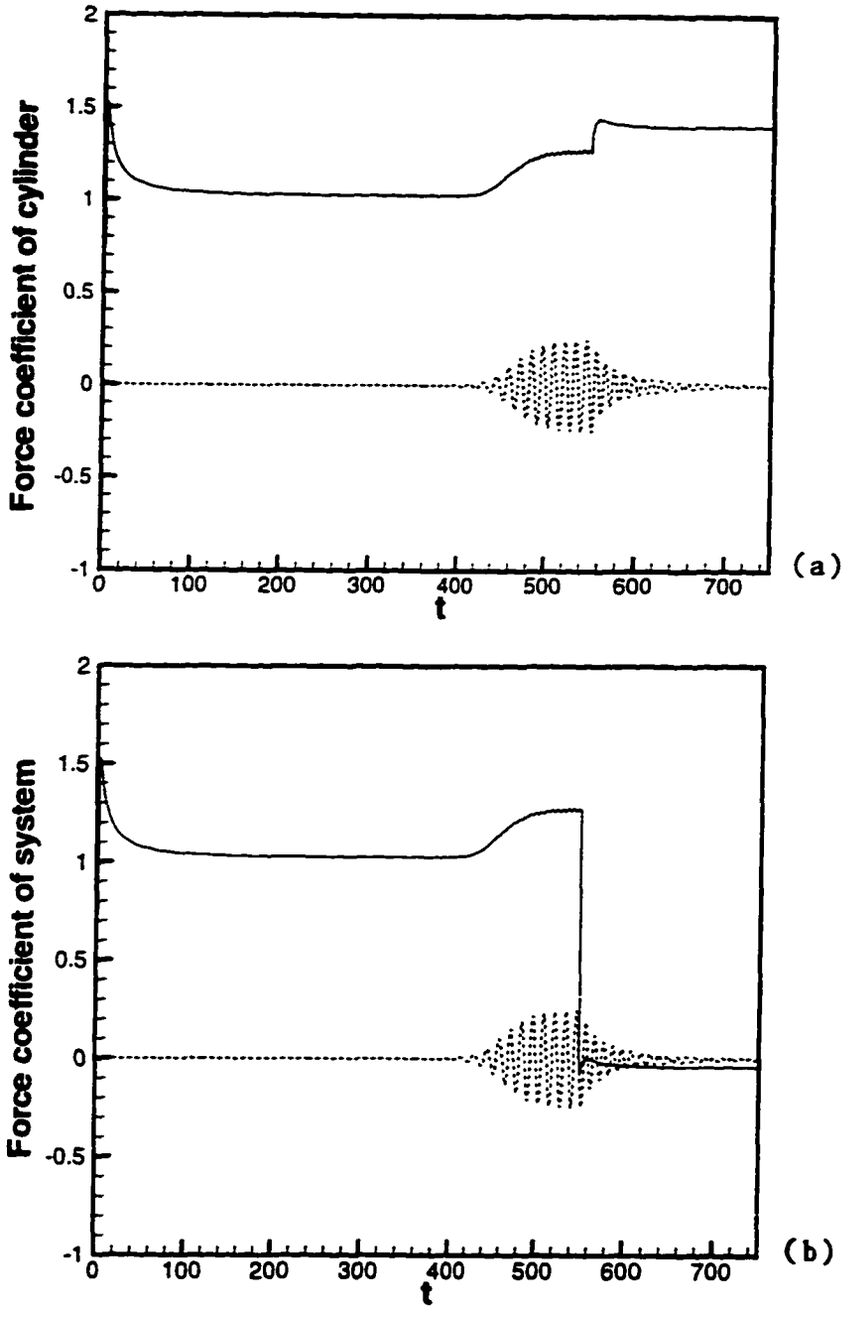

Figure 4.7: Time history of the force coefficients (a) on the body, (b) on the full system: drag coefficient (solid line), lift coefficient (dashed line).

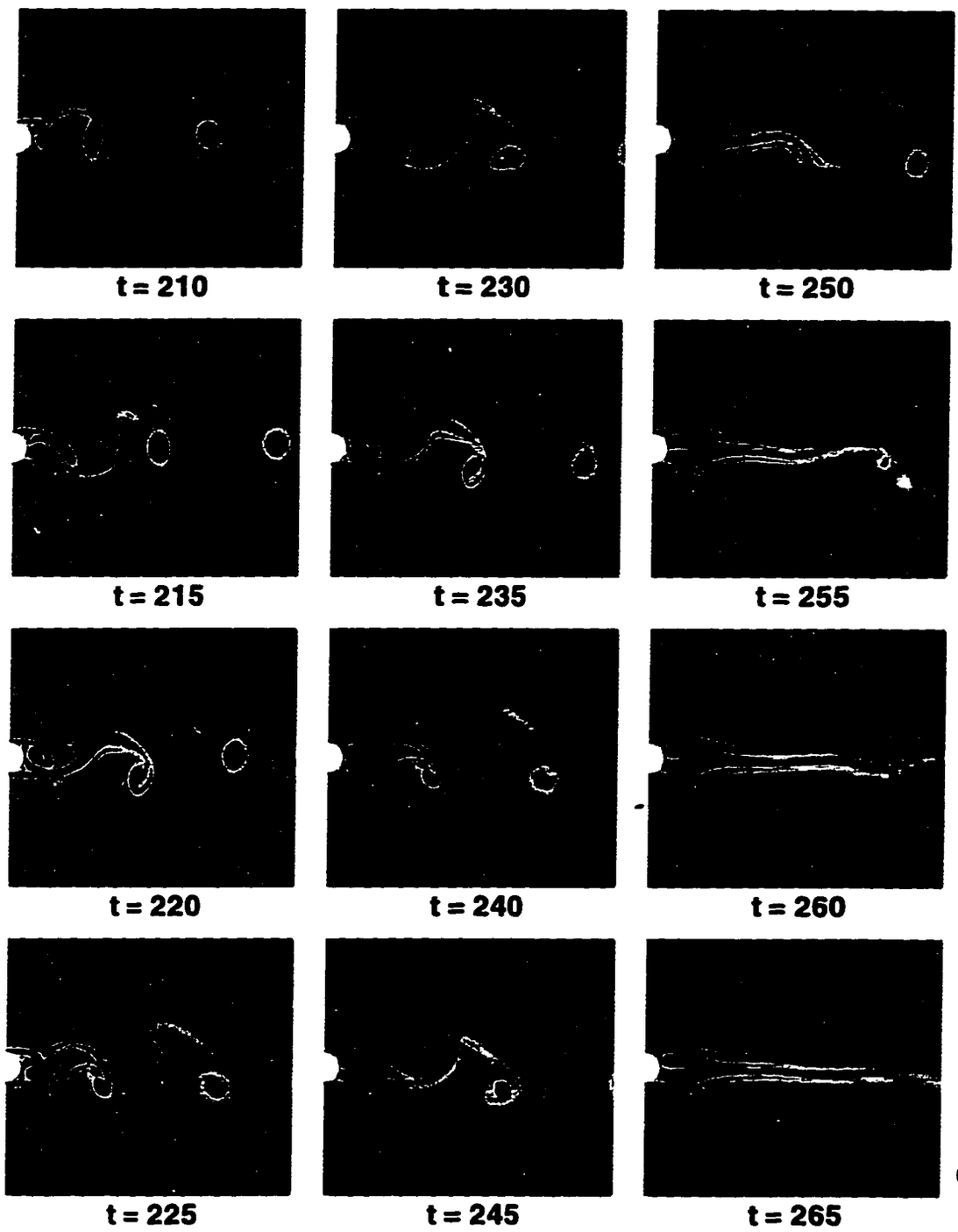

(a)

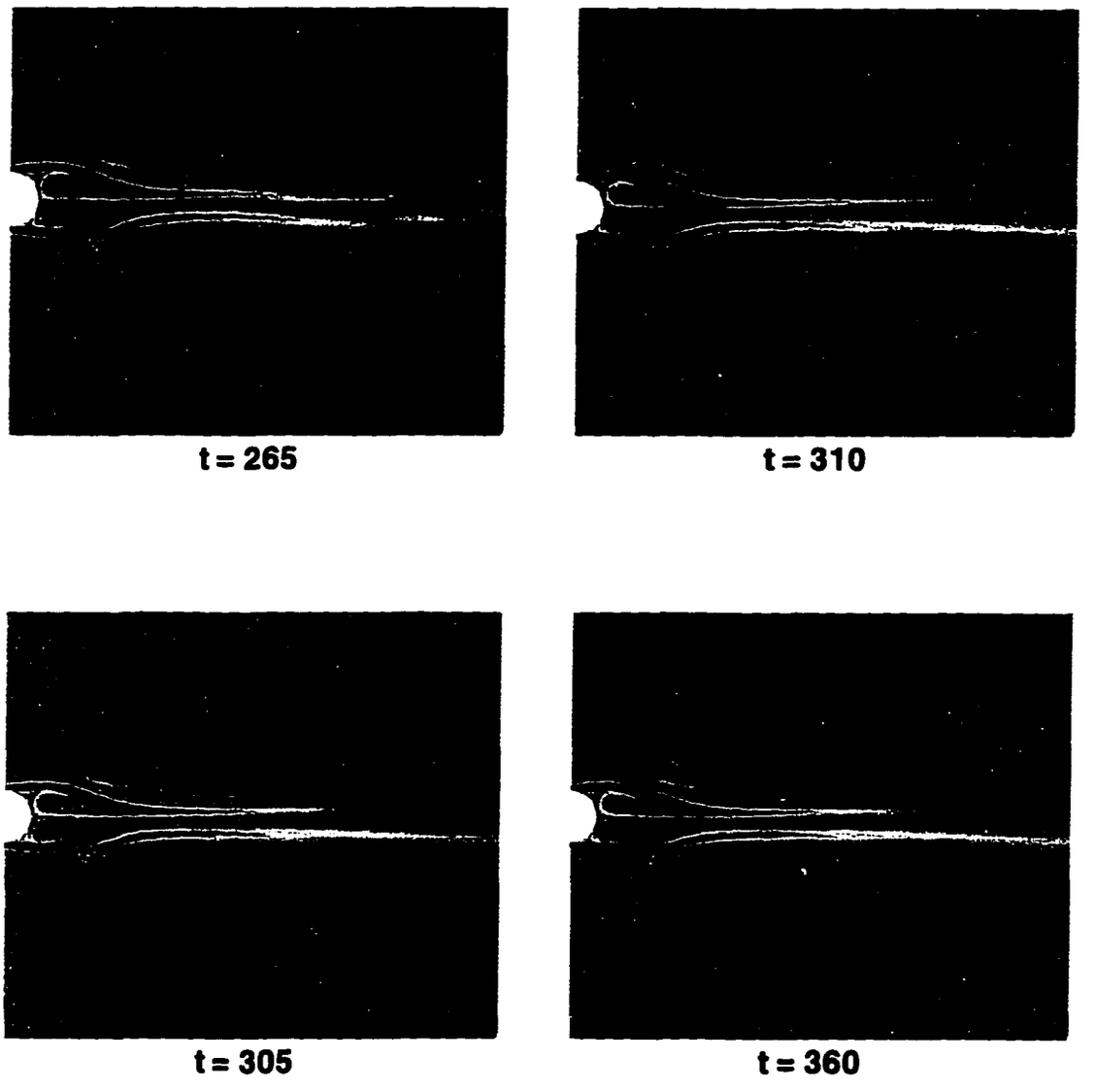

Figure 4.8: Vorticity contours showing the suppression of vortex shedding by insertion of two small control vortices ($\omega_c = 0.8$) at the location $x_c = 2.908, y_c = \pm 1.375$ at $Re = 1000$. At time $t = 210$, the flow is in its natural vortex shedding state. The control vortices are inserted in the flow at time $t = 210.01$. (a) the evolution of the controlled wake, (b) the late evolution of the bubble toward its asymptotic state.

4.3.2 Control of vortex shedding at $Re = 100$

We now investigate whether the control technique can destabilize vortex shedding itself after the latter has settled. The flow is the same as that previously described but now we insert the previous control vortices at a much later time ($t = 550.01$), more precisely after the Karman vortex street has settled. Figure 4.6 shows that our control strategy has a significant effect on the flow which is now attracted to an asymptotic stable state consisting of a symmetric bubble. The latter is very similar to that previously obtained by controlling the *onset* of vortex shedding. Figure 4.7 displays the corresponding force coefficients. The lift on both the body and the system decays to zero in the presence of the control. The drag on the body slightly increases, while the drag on the system undergoes a significant decrease. As before, the drag value of the asymptotic solution is slightly negative. It is interesting to note that the drag coefficient (on the body) of the asymptotic bubble is $C_d^2 = 1.402$ while that obtained by controlling the *onset* of vortex shedding is $C_d^1 = 1.401$. The very small relative error between these two values ($\sim 10^{-3}$) confirms the fact that the two asymptotic solutions of figure 4.4 (right column) and figure 4.6 are the same. This solution constitutes an attractor for the controlled flow whether the initial condition is the recirculating bubble or the Karman vortex street.

4.3.3 Control of vortex shedding at $Re = 1000$

We now investigate whether our control strategy still works at higher Reynolds numbers. For this, we consider $Re = 1000$. Figure 4.8 shows the natural vortex shedding, and the evolution of the flow after insertion of the control ($\omega_c = \pm 0.8$, at the location $(x_c, y_c) = (2.908, \pm 1.375)$). It is interesting to note that soon after the control is turned on, the vortex generated near the body in the upper mid-plane stretches

downward as it interacts with the upper control vortex. This stretching process ends by a shedding of this vortex in the lower mid-plane. Likewise, the vortex generated near the body in the lower mid-plane stretches upward before being shed in the upper mid-plane. This dynamics results in a reversed Karman vortex street. The asymmetric bubble consisting of a small vortex and a large one gradually deforms into a symmetric bubble of two counter-rotating vortices of the same size. In the mean time, the intensity of the far wake dynamics decays. It is interesting to concentrate on the final evolution of the asymptotic bubble (see figure 4.8(b)). While large values of vorticity are concentrated in the inner part of the bubble at time $t = 265$, this vorticity decays at later times. At time $t = 360$, high concentrations of vorticity can be found in the shear layers only. The time history of the force coefficients can be observed in figure 4.9. Under the influence of the control, the lift and drag first oscillate during the transient flow, particularly the reversed Karman vortex street. The frequency characteristic of the reversed Karman vortex street is similar to the frequency of the natural vortex shedding. This is consistent with the fact that the reversion of the street originates in the interaction between the shed vortices and the control vortices, and not in the manner the vortices are shed from the body. The lift then decays to zero, while the drag on the body tends to a constant value smaller than the average drag value of the natural vortex shedding. As before, the drag on the system containing both the body and the control vortices decays significantly. The asymptotic negative value is an indicator that propulsion on the full system takes place.

Although the effect of the control persists as the strength and location of the perturbation vary, it is clear that it becomes weaker as the strength of the control vortices decreases. We now introduce the same vorticity in the flow at the same location as before, but with a half vorticity value, that is $\omega_c = \pm 0.4$. In this case,

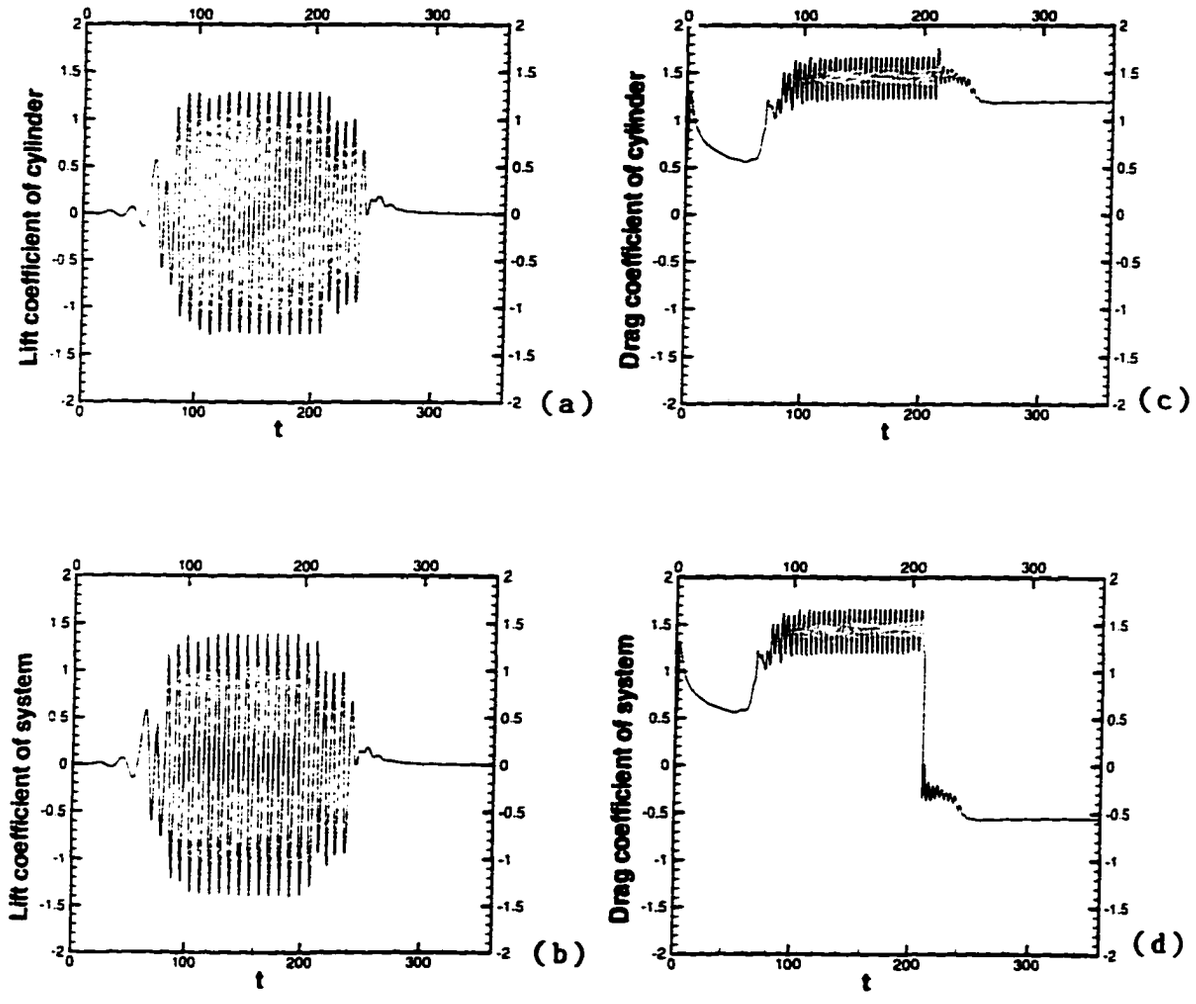

Figure 4.9: Time history of the force coefficients for the flow visualized in figure 4.8: (a) lift coefficient on the body, (b) lift coefficient on the full system, (c) drag coefficient on the body, (d) drag coefficient on the full system.

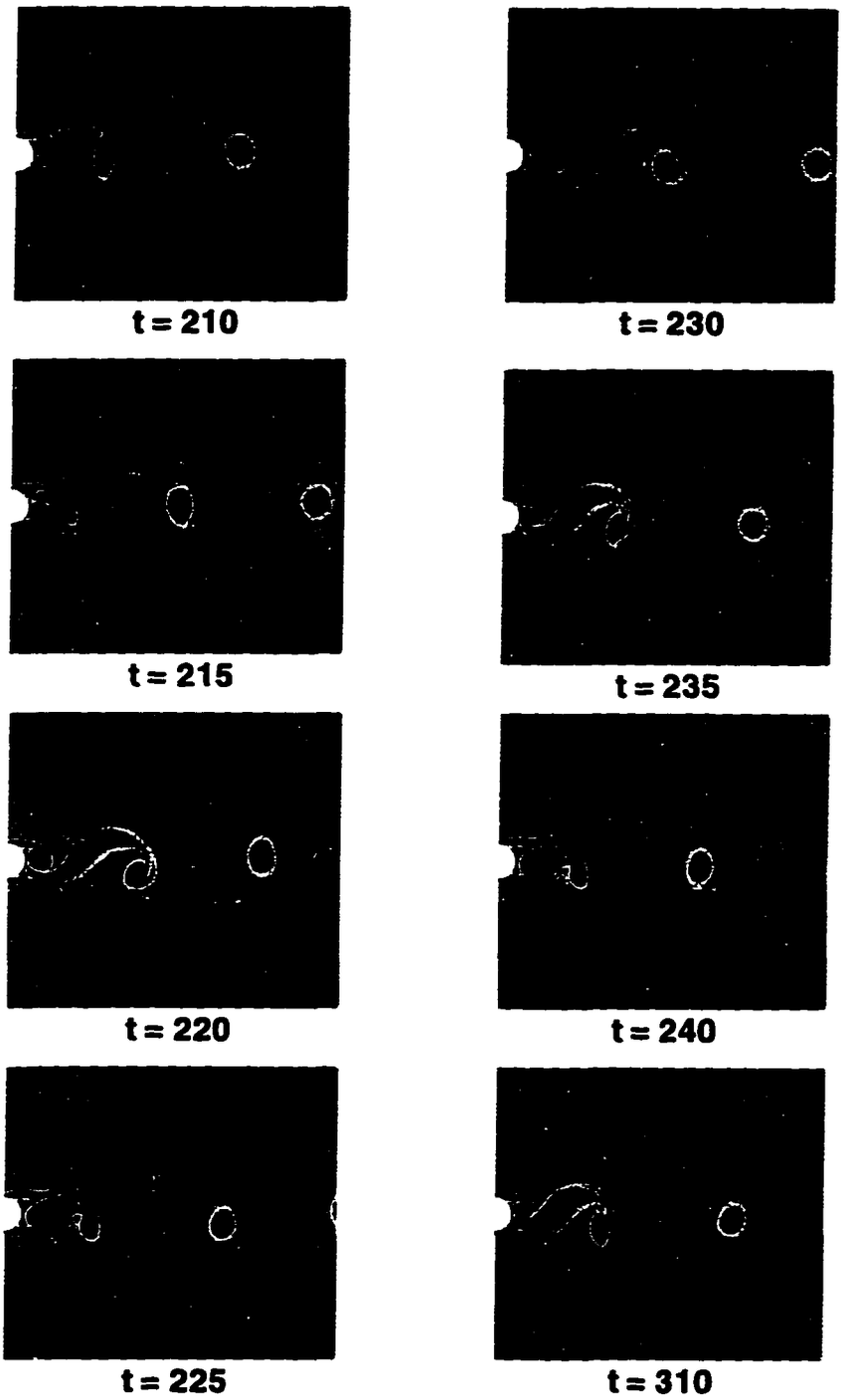

Figure 4.10: Vorticity contours showing the alteration of vortex shedding by insertion of two small control vortices ($\omega_c = 0.4$, other parameters are the same as in fig. 4.8). The asymptotic state of the flow is a reversed Karman vortex street.

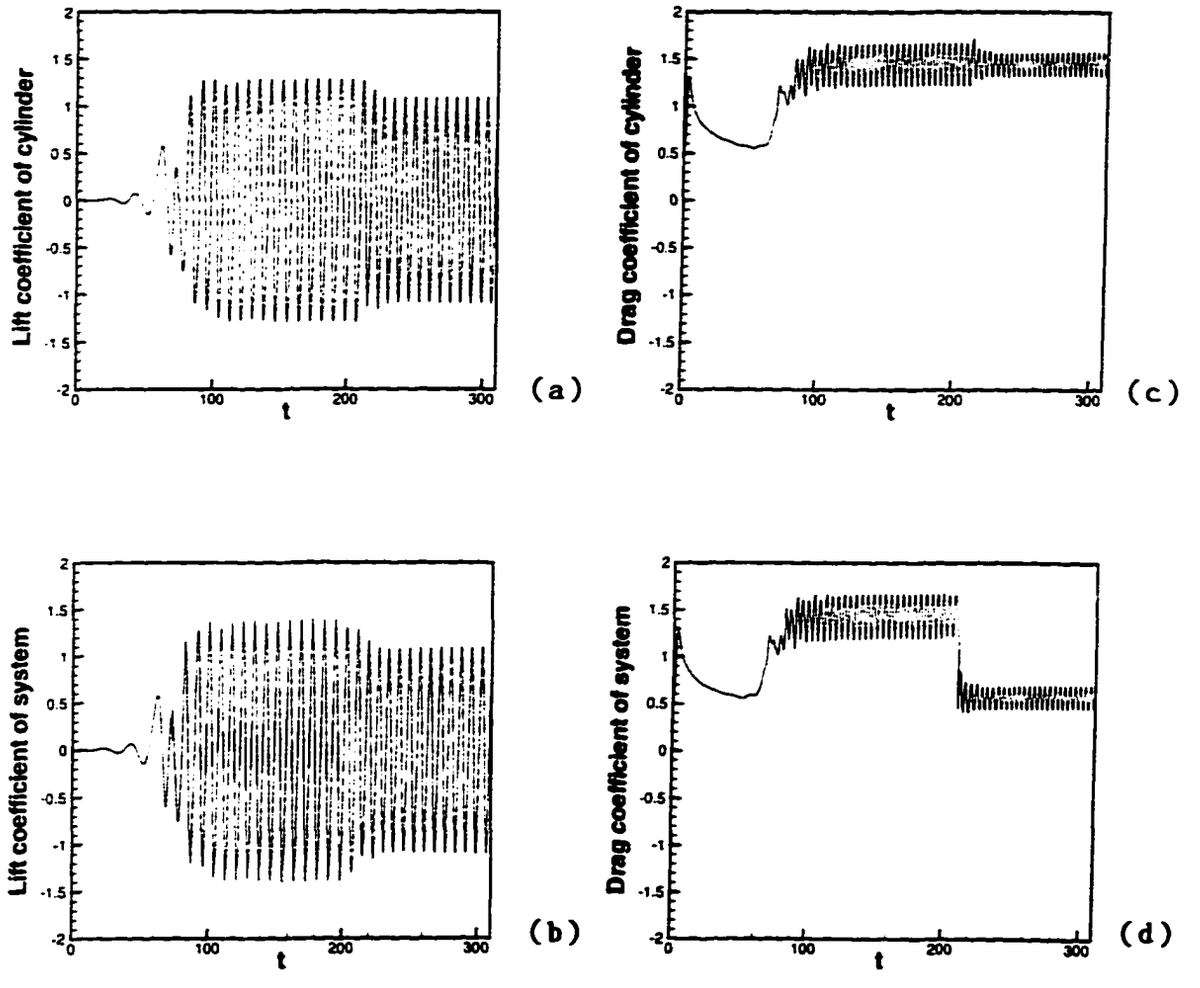

Figure 4.11: Time history of the force coefficients for the flow visualized in figure 4.10: (a) lift coefficient on the body, (b) lift coefficient on the full system, (c) drag coefficient on the body, (d) drag coefficient on the full system.

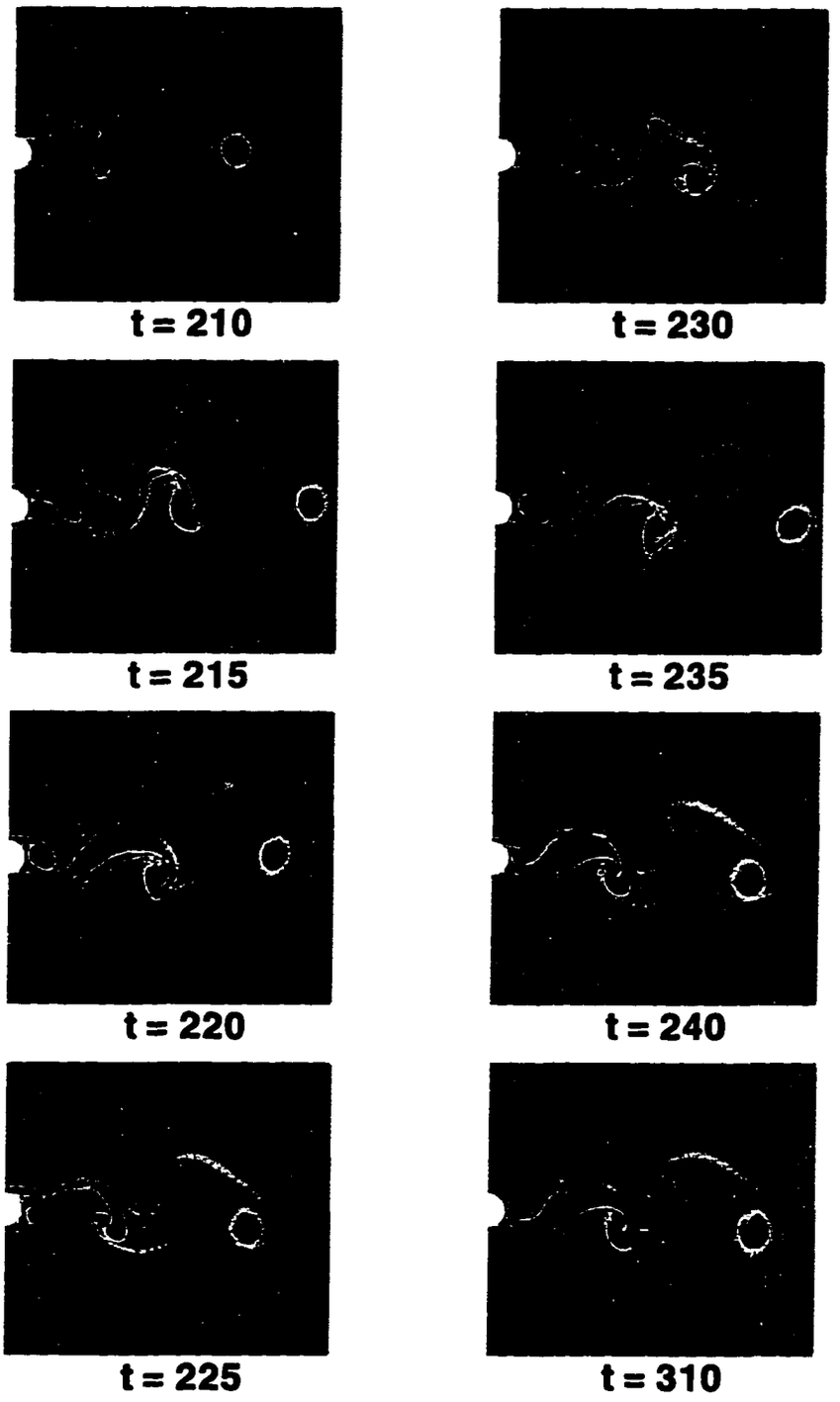

Figure 4.12: Vorticity contours showing the alteration of vortex shedding by two control vortices ($\omega_c = 0.8$) at $x_c = 3.912, y_c = \pm 1.346$ at $Re = 1000$. The asymptotic state is a reversed Karman vortex street.

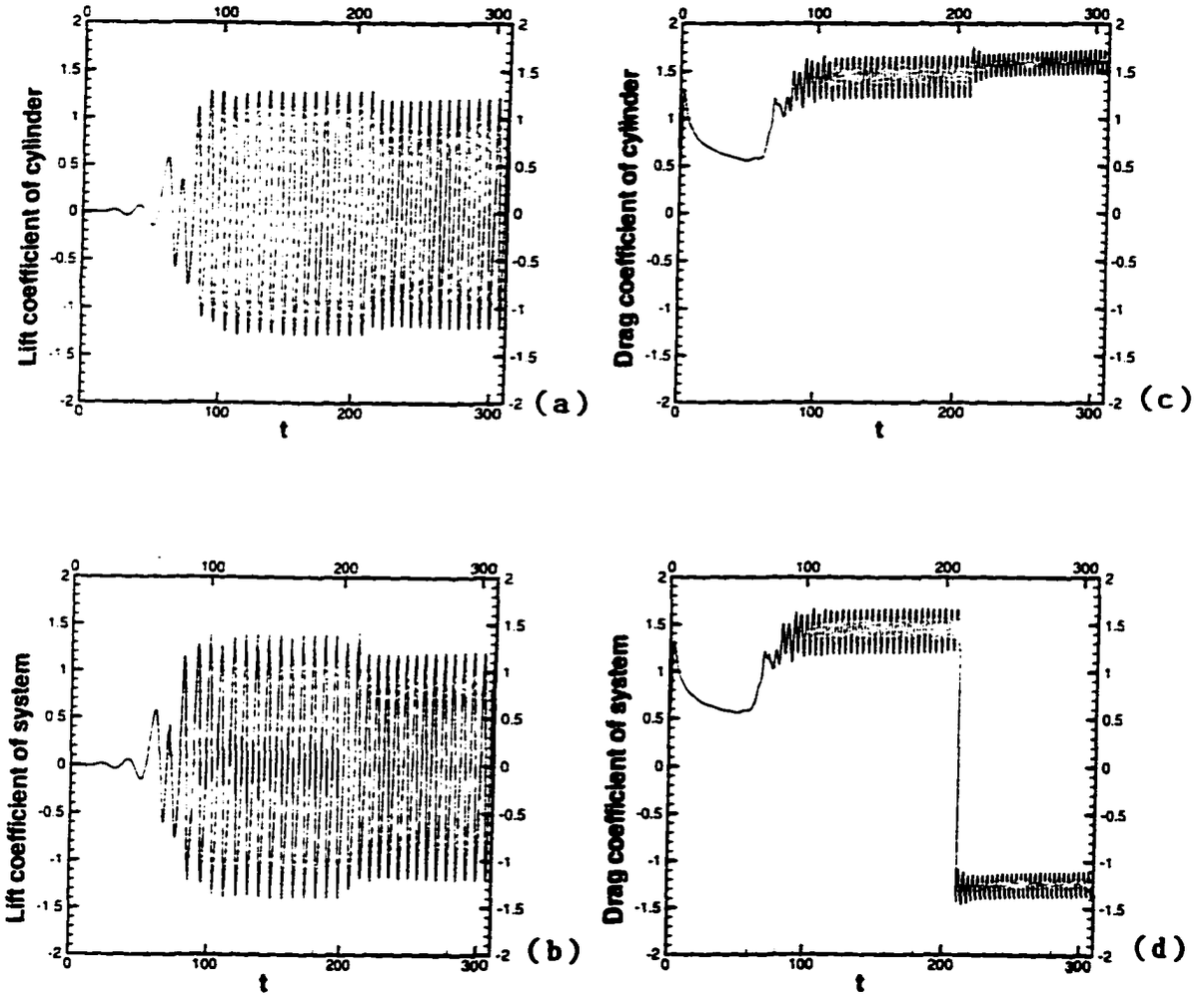

Figure 4.13: Time history of the force coefficients on the cylinder: (a) lift coefficient on the body, (b) lift coefficient on the system, (c) drag coefficient on the body, (d) drag coefficient on the system.

the natural Karman vortex street gets deformed into a reversed Karman vortex street through the same physical phenomena as those previously observed in figure 4.8(a). The flow, however, is not attracted to a stable steady state. Figure 4.10 visualizes the transient flow at various times and figure 4.11 displays the corresponding force coefficients. After insertion of the control vortices, the force still oscillates at the same frequency as before the introduction of the control but the amplitude of the oscillations is smaller.

The introduction of the control vortices ($\omega_c = \pm 0.8$) further downstream (at the location ($x_c = 3.912, y_c = \pm 1.346$)) than in the original experiment has also a weaker effect on the flow as expected. The results are gathered in figures 4.12 and 4.13. In this case as in the previous one, a reversed Karman vortex street, responsible for asymptotic oscillations of the force coefficients, is obtained. The width of the wake, together with the amplitude of the oscillations, seems to be larger than that observed in figures 4.10 and 4.11.

4.4 Conclusions

In this Chapter, we have controlled the wake flow past a circular cylinder above the critical Reynolds number. Our control strategy is based upon our understanding of the instability of the recirculating bubble. This instability was studied via the low dimensional point vortex model originally derived by Föppl. We have shown that the unstable mode of the model is indeed responsible for the instability of the bubble in the viscous flow. The question is then whether it is possible to control the instability in the model. This is achieved in this study by introducing an additional pair of vortices, referred to as *control vortices*, for which the circulation is kept small compared with the circulation of the twin vortices. The insertion of extra

point vortices generates additional steady (symmetric) *bubble* solutions, one of which being neutrally stable (rather than unstable). This control mechanism is also found to be efficient in controlling the viscous flow. In the latter case, the vortex shedding regime never develops if additional (control) vorticity is inserted in the flow before symmetry breaking occurs. We have also shown that our control strategy destabilizes the Karman vortex street, making the flow converge toward a steady, stable bubble solution. In two dimensions, this works at small Reynolds number ($Re = 100$) and at relatively high Reynolds number ($Re = 1000$). In the case of a weaker control (the vorticity of the control vortices is smaller or the control vortices are located farther downstream). the Karman vortex street is reversed. The control technique works also at $Re = 500$ (see Tang and Aubry, 1997c).

One may wonder whether the strength of the control vortices in the viscous flow is small compared to that of the twin vortices. In order to address this issue, we consider the asymptotic controlled bubble flow. Since this state is symmetric by reflection through the centerline, our estimate is restricted to the upper half-plane only. We first determine the point located on the surface of the body such that the vorticity is zero (separation point). This point defines a *separation angle* with the centerline. We then consider the portion P of the wake located within the separation angle. In this part of the domain, we associate all *negative* vorticity with the twin vortex, and all *positive* vorticity with the control vortex. In each vortex, we then determine the maximal vorticity value (in absolute value) which we denote $|\omega^t_{max}|$ for the twin vortex, and $|\omega^c_{max}|$ for the control vortex. We then compute the circulation corresponding to all *negative* vorticity such that $|\omega| > 0.1|\omega^t_{max}|$ for all points in P. This gives us an estimate of the circulation characteristic of the upper twin vortex, Γ_t. In order to estimate the circulation associated with the control vortex, Γ_c, we proceed in the same manner and compute the circulation corresponding to all *positive*

vorticity such that $|\omega| > 0.1|\omega^c_{max}|$. For the controlled bubble obtained at $Re = 100$, we find that $\Gamma_t = 8.79$ and $\Gamma_c = 0.25$, thus leading to a ratio $\Gamma_c/\Gamma_t = 0.028$. For the controlled bubble obtained at $Re = 1000$, we obtain $\Gamma_t = 10.75$ and $\Gamma_c = 1.11$, thus leading to a ratio $\Gamma_c/\Gamma_t = 0.10$. It is clear that we have not optimized our control technique. Particularly at $Re = 1000$, it should be possible to decrease the ratio Γ_c/Γ_t below 10%.

Despite the similarity between the stability characteristic of the potential model and that of the viscous flow, we refrain ourselves from extending our comparison between the model and the numerically simulated flow further. In particular, it is well-known that the vortices present in the viscous flow are very different from point vortices. It is, however, somewhat intriguing that the neutrally stable equilibrium of the controlled model is located farther downstream than the unstable equilibria. This qualitative feature persists in the viscous flow in the sense that the asymptotic controlled bubble flow has most of its vorticity concentrated in the shear layers. This high concentration of vorticity thus extends farther downstream than in the uncontrolled bubble. This discrepancy between the naturally growing bubble and the asymptotic controlled bubble can be clearly observed in figure 4.14 which shows the asymptotic flow of figure 4.8 in a slightly different manner.

Obviously, there is a need for investigating whether the efficiency of the control technique developed in this chapter will persist in three-dimensional simulations, as well as in experiments, particularly at high Reynolds numbers ($Re > 180$ or so) at which the flow is known to be three-dimensional. This question will be addressed in future work. In practice, the vortex generator could be a small airfoil or a small rotating cylinder. In any case, the efficiency of the presence of small vortices in controlling the flow has shown how a small *local* change can have major *global* consequences on wake flows.

t = 10

t = 210

t = 360

(a)

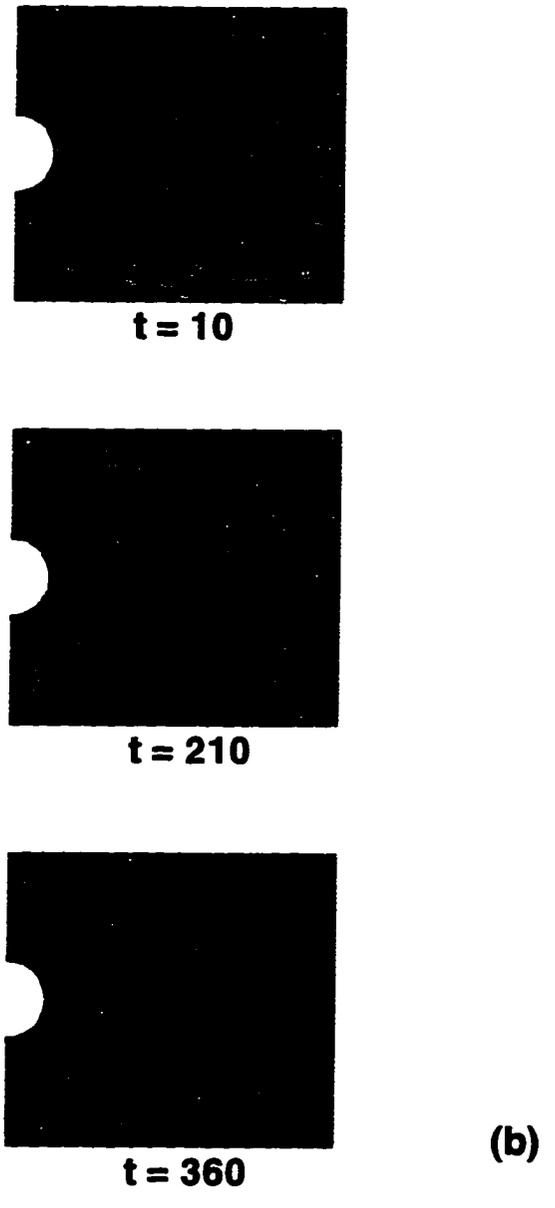

Figure 4.14: Regions of positive and negative vorticity for the flow displayed in figure 4.8: (a) $|\omega| \geq 1.5$, (b) $|\omega| \geq 2.0$.

Bibliography

[1] Abernathy, F. H. and Kronauer, R. E. 1961 The formation of vortex streets. J. Fluid Mech. 13, 11-20.

[2] Acrivos, A., Leal, L. G., Snowden, D. D. and Pan, F. 1968 Further experiments on steady separated flows past bluff objects. J. Fluid Mech. 34, 25-48.

[3] Anagnostopoulos, P. 1989 Numerical solution for laminar two-dimensional flow about a fixed and transversely oscillating cylinder in a uniform stream. J. Comput. Phys. 85, 434-456.

[4] Anagnostopoulos, P. and Iliadis, G. 1996 Numerical study of the blockage effects on viscous flow past a circular cylinder. Int. J. Numer. Methods Fluids 22, 1061-1074.

[5] Aubry, N. and Lima, R. 1995 Spatio-temporal and statistical symmetries. J. Stat. Phys. 81, 793-828.

[6] Aubry, N. Lima, R. and Guyonnet, R. 1992 Spatio-temporal symmetries and bifurcations via biorthogonal decompositions. J. Nonlinear Sci. 2, 183-215.

[7] Aubry, N., Holmes, P., Lumley, J. L. and Stone, E. 1988 The dynamics of coherent structures in the wall region of a turbulent boundary layer. J. Fluid Mech. 192, 115-172, 1988.

[8] Bar-Lev, M. and Yang, H. T. 1975 Initial flow field over an impulsively started circular cylinder. J. Fluid Mech. 72, 625-647.

[9] Bearman, P. W. 1967 The effect of base bleed on the flow behind a two-dimensional model with a blunt trailing edge. Aero. Q. 18, 207-224.

[10] Bearman, P. W. and Graham, J. M. R. 1980 Vortex shedding from bluff bodies in oscillatory flow: A report on Euromech 119. J. Fluid Mech. 99, 225-245.

[11] Berger, E. 1967 Suppression of vortex shedding and turbulence behind oscillating cylinders. Phys. Fluids Suppl. 10, 191-193.

[12] Berger, E. and Wille, R. 1972 Periodic flow phenomena. Annu. Rev. Fluid Mech. 4, 313-340.

[13] Blasius, H. 1908 Grenzchichten in Flussigkeiten mit Kleiner Reiburg. Z. Angew. Math. Phys. (Engl. Transl.) NACA TM-1256 56, 1.

[14] Bouard, R. and Coutanceau, M. 1980 The early stage of development of the wake behind an impulsively started cylinder for $40 < Re < 10^4$. J. Fluid Mech. 101, 583-607.

[15] Braza, M., Chassaing, P. and Ha Minh, H. 1986 Numerical study and physical analysis of the pressure and velocity fields in the near wake of a circular cylinder. J. Fluid Mech. 165, 79-130.

[16] Chilukuri, R. 1987 Incompressible laminar flow past a transversely vibrating cylinder. ASME J. Fluids Eng. 109, 166-171.

[17] Coller, B. D., Holmes, P. and Lumley, J. L. 1994 Control of bursting in boundary layer models. Appl. Mech. Rev. 47 (6), part 2: S139-143, 1994. Mechanics USA 1994, ed. A. S. Kobayashi.

[18] Collins, W. M. and Dennis, S. C. R. 1973a The initial flow past an impulsively started circular cylinder. Quart. J. Mech. Appl. Math. 26, 53-75.

[19] Collins, W. M. and Dennis, S. C. R. 1973b Flow past an impulsively started circular cylinder. J. Fluid Mech. 60, 105-127.

[20] Coutanceau, M. and Bouard, R. 1977 Experimental determination of the main features of the viscous flow in the wake of a circular cylinder in uniform translation. Part 2. Unsteady flow. J. Fluid Mech. 79, 257-272.

[21] Coutanceau, M. and Defaye, J. R. 1991 Circular cylinder wake configurations: A flow visualization survey. Appl. Mech. Rev. 44, 255-305.

[22] Dennis, S. C. R. and Chang, G. 1970 Numerical solutions for steady flow past a circular cylinder at Reynolds numbers up to 100. J. Fluid Mech. 42, 471-489.

[23] Eaton, B. E. 1987 Analysis of laminar vortex shedding behind a circular cylinder by computer-aided flow visualization. J. Fluid Mech. 180, 117-145.

[24] Engelman, M. S. and Jamnia, M. A. 1990 Transient flow past a circular cylinder: A benchmark solution. Int. J. Numer. Methods Fluids 11, 985-1000.

[25] Ffowcs Williams, J. E. and Zhao, B. C. 1989 The active control of vortex shedding. J. Fluids Structures, 3, 115-122.

[26] Föppl, L. 1913 Wirbelbewegung hinter einem Kreiszylinder. Sitzb. d. k. bäyr. Akad. d. Wiss. 1-17.

[27] Fornberg, B. 1980 A numerical study of steady viscous flow past a circular cylinder. J. Fluid Mech. 98, 819-855.

[28] Fornberg, B. 1985 Steady viscous flow past a circular cylinder up to Reynolds number 600. J. Comp. Phys. 61, 297-320.

[29] Franke, R., Rodi, W. and Schonung, B. 1990 Numerical calculation of laminar vortex-shedding flow past cylinders. J. Wind Eng. Ind. Aerodyn. 35, 237-257.

[30] Gerrard, J. H. 1966 The mechanics of the formation region of vortices behind bluff bodies. J. Fluid Mech. 25, 4011-413.

[31] Gerrard, J. H. 1978 The wakes of cylindrical bluff bodies at low Reynolds number. Phil. Trans. Roy. Soc. A288, 351-382.

[32] Gopalkrishnan, R., Triantafyllou, M. S., Triantafyllou G. S. and Barrett, D. 1994 Active vorticity control in a shear flow using a flapping foil. J. Fluid Mech. 274, 1-21.

[33] Gresho, P. M., Lee, R. L. and Sani, R. L. 1980 On the time-dependent solution of the incompressible Navier-Stokes equations in two and three

dimensions. in Recent Advances in Numerical Methods in Fluids, C. Taylor and K. Morgan (eds.) Pineridge, Swansea, 27-79.

[34] Gresho, P. M., Chan, S. T., Lee, R. L. and Upson, C. D. 1984 A modified finite element method for solving the time-dependent, incompressible Navier-Stokes equations. Part 2: Applications. Int. J. Num. Mech. Fluids 4, 619-640.

[35] Grove, A. S., Shair, F. H., Petersen, E. E. and Acrivos, A. 1964 An experimental investigation of the steady separated flow past a circular cylinder. J. Fluid Mech. 19, 60-80.

[36] Henderson, R. D. 1994 Unstructured spectral element methods: Parallel algorithms and simulations, Ph.D. Thesis, Princeton University.

[37] Henderson, R. D. 1995 Details of the drag curve near the onset of vortex shedding. Phys. Fluids 7 (9), 2102-2104.

[38] Hockney, R. W. 1970 The potential calculation and some applications. Methods Comp. Phys. 9, 135-177.

[39] Honji, H. and Taneda, S. 1969 Unsteady flow past a circular cylinder. J. Phys. Soc. Japan. 27, 1668-1677.

[40] Jackson, C. P. 1987 A finite-element study of the onset of vortex shedding in flow past variously shaped bodies. J. Fluid Mech. 182, 23-45.

[41] Jordan, S. K. and Fromm, J. E. 1972 Oscillatory drag, lift and torque on a circular cylinder in a uniform flow. Phys. Fluids 15, 371-376.

[42] Karman, h. von. 1911 Uber den Mechanismus des Widerstands. den ein bewegter Korper in einer Flussigkeit erzeugt. Nachr. Wiss. Ges. Gottingen. Math. Phys. Klasse. 509-517.

[43] Karniadakis, G. E. and Triantafyllou, G. S. 1989 Frequency selection and asymptotic states in laminar wakes. J. Fluid Mech. 199, 441-469.

[44] Karniadakis, G. E. and Triantafyllou, G. S. 1992 Three-dimensional dynamics and transition to turbulence in the wake of bluff objects, J.F.M. 238, 1-30.

[45] Koumoutsakos, P. and Leonard, A. 1995 High resolution simulations of the flow around an impulsively started cylinder using vortex methods. J. Fluid Mech. 296, 1-38.

[46] Kovasznay, L. S. G. 1949 Hot-wire investigation of the wake behind cylinders at low Reynolds numbers. Proc. R. Soc. A, Lond. 198, 174-190.

[47] Laat, T. W. G. D. and Coene, R. 1995 Two-dimensional vortex motion in the cross-flow of a wing-body configuration. J. Fluid Mech. 305, 93-109.

[48] Lamb, Sir H. Hydrodynamics. 6th ed. Dover, New York, 1945.

[49] Mair, W. A. and Maull, D. J. 1971 Bluff bodies and vortex shedding - a report on Euromech 17. J. Fluid Mech. 45, 209-224.

[50] Maull, D. J. and Milliner, M. G. 1978 Sinusoidal flow past a circular cylinder. Coastal Engineering 2, 149.

[51] Milne-Thomson, L. M. 1962 Theoretical hydrodynamics, 4th ed., Macmillan, London.

[52] Mittal, R. and Balachandar, S. 1995 Effect of three-dimensionality on the lift and drag of nominally two-dimensional cylinders. Phys. Fluids 7 (8), 1841-1865.

[53] Morkovin, M. V. 1964 Flow around circular cylinder-kaleidoscope of challenging fluid phenomena. In Proc. A.S.M.E. Symp. on Fully Separated flows, Philadelphia, 102-118.

[54] Mori, Y., Hijikata, K. and Nobuhara, T. 1986 A fundamental study of symmetrical vortex generation behind a cylinder by wake heating or by splitter plate or mesh. Intl. J. Heat Mass Transfer 29, 1193-1201.

[55] Nayler, J. L. and Frazer, R. A. 1917 Vortex motion. (i) Preliminary report upon an experimental method of investigating, by the aid of kinematograph photography, the history of the eddying flow past a model immersed in water. Advisory Committee for Aeronautics, R. and M. (new series), No. 332, 18-25.

[56] Noto, K., Ishida, H. and Matsumoto, R. 1985 A breakdown of the Karman vortex street due to the natural convection. In Flow Visualization III (ed. W. J. Yang), Hemisphere, 348-352.

[57] Oertel, H. 1990 Wakes behind blunt bodies. Annu. Rev. Fluid Mech. 22, 539-564.

[58] Perry, A. E., Chong, M. S. and Lim, T. T. 1982 The vortex-shedding process behind two-dimensional bluff bodies. J. Fluid Mech. 116, 77-99.

[59] Roshko, A. 1955 On the wake and drag of bluff bodies. J. Aero. Sci. 22, 124-132.

[60] Roussopoulos, K. 1993 Feedback control of vortex shedding at low Reynolds numbers. J. Fluid Mech. 248, 267-296.

[61] Saffman, P. G. 1992 Vortex dynamics. Cambridge Univ. Press.

[62] Sanghi, S. and Aubry, N. 1993 Interaction mode models of near wall turbulence. J. Fluid Mech. 247, 455-488.

[63] Schumm, M. S., Berger, E. and Monkewitz, P. A. 1994 Self-excited oscillations in the wake of two-dimensional bluff bodies and their control. J. Fluid Mech. 271, 17-53.

[64] Seto, M., Ahlborn, B. and Lefrancois, M. 1991 A technique to trigger repeatable vortex wake configurations from bluff bodies. Phys. Fluids 3, 1674-1676.

[65] Shair,F.H. 1963 Theoretical and experimental investigations of fluid flow and heat transfer around a cylinder in the region of low Reynolds number and high Prandtl number. Ph.D. Thesis, University of California, Berkeley.

[66] Shair, F. H., Grove, A. S., Petersen, E. E. and Acrivos, A. 1963 The effect of confining walls on the stability of the steady wake behind a circular cylinder. J. Fluid Mech. 17, 546-550.

[67] Smith, A. C. 1973 On the stability of Föppl's Vortices, J. Appl. Mech. 70, 610-612.

[68] Smith, P. A. and Stansby, P. K. 1988 Impulsively started flow around a circular cylinder by the vortex method. J. Fluid Mech. 194, 45-77.

[69] Stansby, P. K. and Slaouti, A. 1993 Simulation of vortex shedding including blockage by the random-vortex and other methods. Int. J. Numer. Meth. Fluids 17, 1003-1013.

[70] Strouhal, V. 1878 Uber eine besondere Art der Tonerregung. Ann. Phys. Chemie (New series) 5, 216-251.

[71] Strykowski, P. J. and Sreenivasan, K. R. 1990 On the formation and suppression of vortex 'shedding' at low Reynolds numbers. J. Fluid Mech. 218. 71-107.

[72] Strykowski, P. J. and Hannemann, K. 1991 Temporal simulation of the wake behind a circular cylinder in the neighborhodd of the critical Reynolds number", Acta Mechanica, 90, 1-20.

[73] Ta Phuoc Loc 1980 Numerical analysis of unsteady secondary vortices generated by an impulsively started circular cylinder. J. Fluid Mech. 100, 111-128.

[74] Ta Phuoc Loc and Bouard, R. 1985 Numerical solution of the early stage of the unsteady viscous flow around a circular cylinder: a comparison with experimental visualization and measurements. J. Fluid Mech. 160, 93-117.

[75] Takami, H. and Keller, H. B. 1969 Steady two-dimensional viscous flow of an incompressible fluid past a circular cylinder. Phys. Fluids Suppl. II, 51-56.

[76] Tang, S. and Aubry, N. 1996 Direct numerical simulations of the impulsively started flow past a circular cylinder in its transient and asymptotic

regimes. CAMS research report: 96-21, New Jersey Institute of Technology.

[77] Tang, S. and Aubry, N. 1997a On the symmetry breaking instability leading to vortex shedding. Phys. Fluids 9 (to appear).

[78] Tang, S. and Aubry, N. 1997b On the suppression and alteration of vortex shedding. (submitted to Phys. Fluids).

[79] Tang, S. and Aubry, N. 1997c Numerical simulation, modeling and control of the impulsively started flow past a circular cylinder. AIAA-97-2135, Proceeding of 13th AIAA computational fluid dynamics.

[80] Tokumaru, P. T. and Dimotakis, P. E. 1991 "Rotary oscillation control of a cylinder wake," J. Fluid Mech. 224, 77-90.

[81] Triantafyllou, G. S., Triantafyllou, M. S. and Chryssotomidis, C. 1986 On the formation of vortex streets behind stationary cylinders. J. Fluid Mech. 170, 461-477.

[82] Tritton, D. J. 1959 Experiments on the flow past a circular cylinder at low Reynolds numbers. J. Fluid Mech. 6, 547-567.

[83] Wehrmann, O. H. 1965 Reduction of velocity fluctuations in a Karman vortex street by a vibrating cylinder. Phys. Fluids 8, 760-761.

[84] Wille, R. 1960 Karmen vortex streets. Adv. Appl. Mech. 6, 273-287.

[85] Wille, R. 1966 On unsteady flows and transient motions. Prog. Aero. Sci. 7, 195-207.

[86] Williamson, C. H. K. 1989 Oblique and parallel modes of vortex shedding in the wake of a circular cylinder at low Reynolds numbers. J. Fluid. Mech. 206, 579-627.

[87] Williamson, W. H. K. 1995 Vortex Dynamics in the wake of a cylinder, in Fluid Vortices, ed. S. I. Green, Kluwer Academic Publishers (the Netherlands), 1995.

[88] Williamson, C. H. K. 1996 Vortex dynamics in the cylinder wake. Annu. Rev. Fluid Mech. 28, 477-539.

[89] Wood, C. J. 1967 Visualization of an incompressible wake with base bleed. J. Fluid Mech. 29, 259-272.

[90] Zdravkovich, M. M. 1981 Review and classification of various aerodynamic and hydrodynamic means for suppressing vortex shedding,24 J. Wind Eng. Ind. Aerodyn. 7, 145-189.

[91] Zebib, A. 1987 Stability of viscous flow past a circular cylinder. J. Engineering Math. 21, 155-165.

[92] Zhang, H. Q., Fey, U. and Noack, B. R. 1995 On the transition of the cylinder wake. Phys. Fluids 7,779-794.